Supporting Information

An In-Depth Analysis Approach Enabling Precision Single Chain Nanoparticle Design

Johanna Engelke[1, 2, 3], Bryan Tuten[1, 4] *, Ralf Schweins[5], Hartmut Komber [2], Leonie Barner[1, 6] *,

Laura Plüschke[2, 3], Christopher Barner-Kowollik[1, 4] *, Albena Lederer[2, 3, 7] *

[1]School of Chemistry and Physics, Queensland University of Technology, 2 George Street, Brisbane, QLD 4000, Australia

[2] Leibniz-Institut für Polymerforschung Dresden, Hohe Str. 6, 01069 Dresden, Germany

[3] School of Science, Technische Universität Dresden, 01062 Dresden, Germany

[4] Centre for Materials Science, Queensland University of Technology, 2 George Street, Brisbane, QLD 4000, Australia

[5] Institut Laue-Langevin, DS / LSS, CS 20 156, 71 Avenue des Martyrs, 38042 Grenoble CEDEX 9, France

[6] Institute for Future Environments, Queensland University of Technology, 4000 QLD Brisbane, Australia

[7] Stellenbosch University, Department of Chemistry and Polymer Science, Private Bag X1, Matieland 7602, South Africa

*To whom all correspondence should be addressed. Phone: +49 351 4658 491, E-mail: lederer@ipfdd.de

Table of Contents

1. Theoretical Background

The most important equations employed in this work are listed below; equations of the contraction factors g and $g^{`}$, apparent density d_{app} and the characteristic ratios κ and ρ are given in the main text. The Rayleigh ratio R_θ describes the scattering intensity I_θ at the angle θ.

$$R_\theta = \frac{I_\theta}{I_0}\left(\frac{r^2}{1+\cos^2\theta}\right) \tag{SI-1}$$

The M_w is obtained from scattering experiments, as shown in the fundamental light scattering equation below (Zimm formalism). This ratio describes the relation of the distance between the scattering object and the detector (r), the scattering intensity $I(q)$ at angle θ and the intensity of the incident beam (I_0).

$$\frac{K*c}{R(\theta)} = \frac{1}{M_w P(\theta)} + 2A_2 c \tag{SI-2}$$

In case of light scattering, the optical constant K_{LS} reveals the importance of the refractive index increment for the scattering intensity.

$$K_{LS} \propto \left(\frac{dn}{dc}\right)^2 \tag{SI-3}$$

The radius of gyration R_g (also known as mean square radius of gyration) is a measure of molecular size, based on the molecule's mass distribution around its center of mass. For the calculation of the radius of gyration R_g, the root of the average squared distance R_k of any scattering point k in the molecule from its center of mass is determined. The molar mass dependence of R_g is given in the scaling law, revealing the scaling exponent ν, were K is a constant as follows:

$$R_g = \langle\frac{1}{N}\sum_k R_k^2\rangle^{1/2} = KM^\nu \tag{SI-4}$$

The scaling exponent ν is an important measure of macromolecular conformation in solution. The scaling exponent ν can be derived from the double logarithmic SANS scattering curve as follows:

$$\nu = \frac{-1}{d_{fractal}} = \frac{-1}{slope_{scattering\ curve}} \tag{SI-5}$$

The hydrodynamic radius R_h is the radius of a hypothetical hard sphere that diffuses at the same rate as the molecule with a particular translational diffusion coefficient. The Stokes-Einstein relation describes the relation of R_h to D_t - the diffusion coefficient, k_B - the Boltzmann's constant, T - the temperature (in Kelvin), and η - the viscosity of the solvent:

$$D_t = \frac{k_B T}{6\pi\eta R_h} \tag{SI-6}$$

The overlap concentration or critical concentration c^* is the polymer concentration, at which polymer chains start to overlap, thus form a transient interpenetrating network. Solutions with concentrations below c^* are coined diluted solutions.

$$c^*_{R_{g,z}} = \frac{M_w}{\frac{4}{3}\cdot\pi\cdot R_{g,z}^3\cdot N_A} \tag{SI-7}$$

2. Materials and Methods

2.1. Instrumentation

Small-angle neutron scattering (SANS) measurements were carried out at the instrument D11 of the Institute Laue-Langevin (ILL, Grenoble) at a constant temperature of 298 K. The neutron wavelength was set to 5 Å (Full Width at Half Maximum (FWHM) 9%). A broad q-range from 0.003 Å^{-1} – 0.54 Å^{-1} was covered using three sample-detector distances of 1.4 m, 8 m and 20 m (with collimation distances of 8 m, 8 m and 20.5 m) for the 50 kDa samples. For all other samples only the two shorter sample-detector distances have been used, yielding a q-range of 0.008 Å^{-1} – 0.54 Å^{-1}. A circular neutron beam of 14 mm diameter has been used, together with 404-QS quartz cuvettes with a path-length of 1 mm (*Hellma Analytics*, DE). The scattering intensities were recorded with a multi-wire proportional chamber (MWPC) detector (*CERCA*) having 256 x 256 pixels of size 3.75 mm x 3.75 mm. All obtained data were normalized by use of the secondary calibration standard water and its known differential scattering cross section ($d\Sigma/d\Omega_{H20}$, 1mm, at 5 Å: 0.929 cm^{-1}) making use of the software package LAMP. The scattering behavior of the perdeuterated solvent THF-d$_8$ (*Eurisotop*, Cambridge Isotope Laboratories, Inc.) was also measured and subtracted from the solution data. Eventually, the incoherent scattering intensity has been determined from the plateau intensity at large q-values and subtracted from the scattering curves. An illustration about the set-up is shown in SI figure 43.

The investigated samples were dissolved in deuterated solvent THF-d$_8$ (99.5%, *Eurisotop*). Each polymer sample (20C, 50A, 50B, 50C, 100A, 100C) was measured in the dilute solution regime with concentrations of 25, 20, 5, 2, 1 mg/mL in THF-d$_8$ giving in 60 samples in total. The preparation of the solutions was performed several hours prior to the measurement to ensure equilibrium state of the dissolved polymer.

^{1}H (500.13 MHz), ^{13}C (125.76 MHz) and ^{19}F (470.59 MHz) nuclear magnetic resonance (NMR) spectra were recorded on an Avance III 500 NMR spectrometer (*Bruker*) at 30 °C. The ^{1}H and ^{13}C NMR spectra were referenced to the solvent signal (CDCl$_3$: δ (^{1}H) = 7.26 ppm, δ (^{13}C) = 77.0 ppm). ^{19}F NMR spectra were referenced to external C$_6$F$_6$ (δ (^{19}F) = −163.0 ppm) if stated. The apparent coupling constants are given in Hertz. The description of the fine structure means: br = broad, s = singulett, d = dublett, t = triplett, q = quartett, m = multiplett, dt = dublett of triplett.

Size-exclusion chromatography characterization with multiple detection (SEC-MALS/QELS/VS/dRI; SEC-D4) was performed using *Agilent* 1200 isocratic HPLC-pump and autosampler (*Agilent Technologies*, Santa Clara, CA). A set of two MIXED-C columns (300 x 7.5 mm; 5 µm particle size; PolarGel, *Agilent Technologies*, US) were connected in series. The fourfold detection (D4, all detectors from *Wyatt Technology* Corp., USA) was based on the following setup: (i) *DAWN® HELEOS II* multi angle light scattering (MALS) detector (λ = 663 nm, equipped with 18 photodiodes at different measuring angles); (ii) quasi-elastic light scattering detector (QELS), which is integrated in the MALS detector in the channel number 17 (nominal angle 144.5° relative to the incident laser beam); (iii) online differential viscometer *ViscoStar® III*, equipped with pump pulse suppression without loss of chromatographic resolution and an automated capillary bridge tuning; (iv) differential refractometer (dRI) *Optilab® T-rEX* (λ = 658 nm), equipped with an 512 diode detector array. An illustration about the set-up is shown in SI Figure 32.

The SEC-D4 flow-system was operated under the following conditions: HPLC grade THF (stabilized with 0.025 % butylhydroxytoluol) as eluent, 1 mL min^{-1} flow rate; 53 µL injection volume.

ASTRA software (*Wyatt Technology*, version 7.1.2.) was used to process and analyze raw data of SEC-D4. All averages and standard deviations were calculated from three measurements. A first order Zimm formalism was employed for fitting the MALS data for molar mass and radius of gyration (R_g) determination. Parameters of the R_g are z-average values, of the hydrodynamic radius R_h and the viscosity radius R_η are uncertainty-weighted average values. Data of viscosity was generally calculated by using Huggins models.[1,2]

2.2. Methods

Manual determination of the second virial coefficient A_2 was performed with the instrument *DAWN® HELEOS II* multi angle light scattering (MALS) detector (Wyatt Technology, US, wavelength 663 nm, equipped with 18 photodiodes at different measuring angles) by manual injection of polymer solutions in ACN/THF: 4/1. Precursor samples 50A, 50B, 50C were analyzed for five concentrations, allowing for Zimm-plotting.

Batch determination of the specific d*n*/d*c* was performed in THF at 25 °C using the *Optilab® T-rEX* refractive index detector off-line. At least five different concentrations were employed to determine the d*n*/d*c* values of each sample after manual injection from the lowest concentration to the highest concentration into the differential refractometer cell. The data was evaluated with the procedure d*n/dc from RI* (software Astra 7.1.2.).

Online determination of the d*n*/d*c* was performed by the method d*n/dc from peak* (assuming 100 % sample mass recovery) from the software Astra 7.1.2 (Wyatt Technology, US) by evaluation of the data received from the hyphenated *Optilab® T-rEX* (Wyatt Technology, US) refractive index detector. All averages of online determined d*n*/d*c* were calculated from at least three measurements.

3. Experimental Procedures

3.1. General Remarks

All reagents were purchased from *Sigma-Aldrich* and used without purification unless otherwise stated. THF-d_8 was purchased from *Eurisotop* with a purity of 99.5%. Azobisisobutyronitrile (AIBN) was recrystallized from methanol. Acetone and anhydrous dioxane was dried and stored over molecular sieves (3 Å). Monomers were stabilized with butylhydroxytoluol (BHT) and disinhibited prior use by a silica-column with DCM as eluent. Transfer of air-sensitive phosphine agents were performed in a glovebox unless otherwise stated.

3.2. Composition-based Refractive Index Increments for Precursor and SCNPs

3.2.1. Experimental Determination of the Refractive Index Increment (d*n*/d*c*)

Batch Determination of the *dn/dc*

Batch determination of the specific d*n*/d*c* was performed in the same solvent as employed for the SEC-D4 characterization (tetrahydrofuran, THF) at 25 °C using the refractive index detector off-line. This technique was applied to crosslinker 1,4-benzenedimethanethiol (BDMT) and FRP copolymers, as polymers obtained from this polymerization technique allows for minimal contamination of the polymer material with small molecules. FRP synthesis requires the use of less reagents than for controlled polymerization techniques, allowing for more accurate batch d*n*/d*c* determination of the polymer material. At least five different concentrations below the critical overlap concentration c* (ranging from 0.2 to 1 mg mL^{-1}) were employed to determine the d*n*/d*c* values of each sample. The results of the batch determination of the d*n*/d*c* values are given in the SI Table 1.

SI Table 1. Results of the batch determination of the dn/dc for two FRP copolymers with respect to their molar amount of functional pentafluorobenzyle units (PFB), and the crosslinker 1,4-benzenedimethanethiol (BDMT).

| sample	PFB	d*n*/d*c*	linear plot	deviation	number of samples
	mol%	ml g^{-1}	%	R²	
poly(PFB) acrylate	100	0.0505	±2.89	0.995	5
poly(PFB-stat-^{t}Bu) acrylate	14	0.0541	±6.09	0.982	5
crosslinker BDMT	-	0.2037	±1.24	0.999	5

In contrast to the low refractive index increment of the crosslinker, very low values of approximately 0.05 ml g^{-1} are obtained for the PFB (co)polymers. This underlines the importance to evaluate the dn/dc of the linear PFB copolymers in dependency of the %PFB decoration, and for the crosslinker loaded SCNPs.

Online Determination of the dn/dc

The online determination of the dn/dc of the copolymer libraries in THF was performed by integration of the RI peak area of the SEC-traces, allowing for more accurate dn/dc determination of polymer samples loaded with possible contamination of small molecules from controlled polymerization techniques. According the assumption of the employed software method, high mass recovery was observed for all precursor samples (SI Table 8).

### 3.2.2. Refractive Index Increments for the Precursor dn/d$c_{precursor}$

Accurate spectroscopic characterization is vivid for the determination of the molar mass and concentration-base data evaluation in general. A comprehensive determination of the refractive indices by online-, and batch measurements for poly(PFB-stat-^{t}Bu) acrylate copolymers of several compositions was performed. The results of online dn/dc determinations of the precursors – multiple measurements per sample - are plotted in dependency of the PFB decoration (SI Figure 1) top graph, the colors indicate the functional group decoration. For sake of accuracy, the online dn/dc values for both, the precursors prior-, and after RAFT group removal were employed to calculate the linear correlation between refractive index increment and precursor composition. The obtained linear fit (indicated by the grey line of the top graph of SI Figure 1) serves to determine the refractive index increments for any precursor composition.
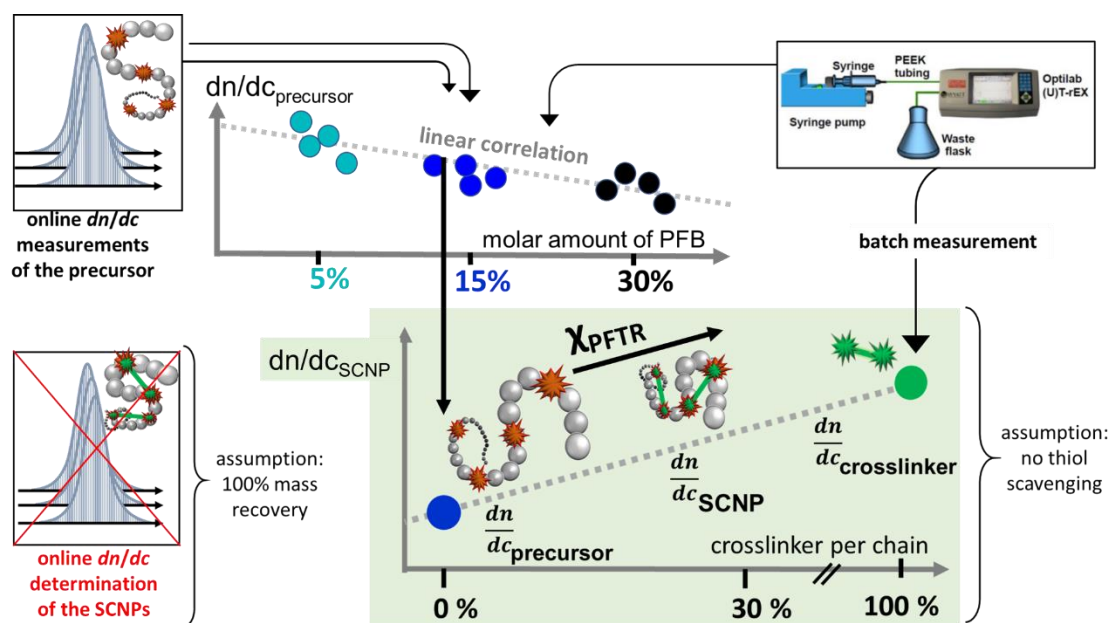
SI Figure 1. Scheme of the strategy for accurate dn/dc determination for precursor of versatile PFB decoration (top graph) as well as for SCNPs with any LD (green highlighted graph on the bottom). This procedure was need as the mass recovery of the SEC-D4 separation was below 90% for some SCNP samples and the online dn/dc determination less reliable, respectively. Numerous online-, and batch dn/dc determination served to deduce a linear correlation between the dn/dc and the % PFB per chain for the precursor (top graph). The obtained linear correlation served as base for the calculation of the dc/dc of the SCNPs (graph at the bottom).

Experimental results of the linear correlation from online dn/dc determination of the precursor are shown in SI Figure 2. The results from batch dn/dc determinations of the FRP copolymers of the same structure validated the linear correlation. FRP copolymers of the same monomer composition, synthesized *via* thermally induced free

radical polymerization (FRP, see Appendix), are suitable for batch dn/dc determination rather than polymers, synthesized *via* controlled polymerization essays. The latter may be derived by RAFT end-groups or the side products of RAFT-group-removal (primarily the phosphine reducing agent), which may impact the refractive index increment and therefore falsify the results. Herein, a reliable linear correlation of dn/dc and precursor composition is evaluated and the final refractive index of the precursors (coined dn/d$c_{precursor}$ in this chapter) is derived from the linear fit for each precursor sample (3D plot in SI Figure 2, SI Table 8).
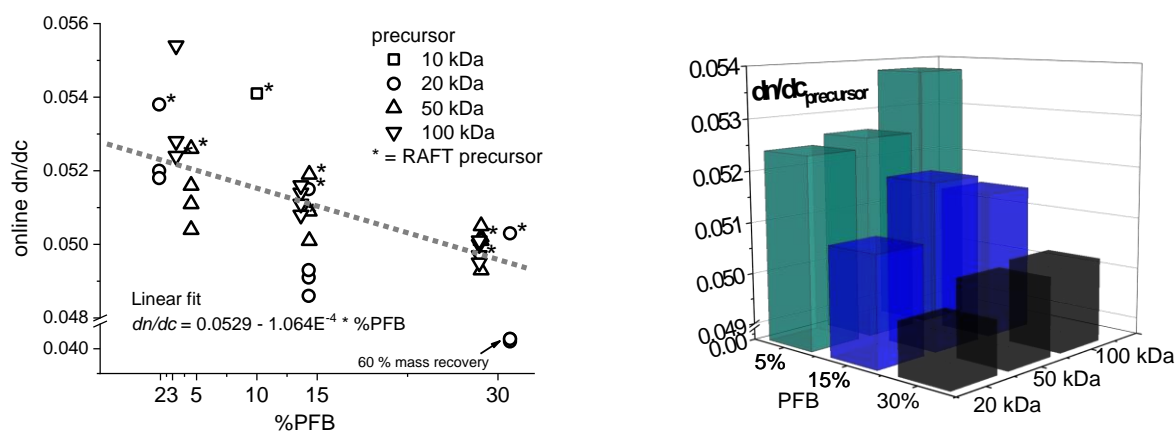
SI Figure 2. Linear fit of online-dn/dc determinations of the RAFT copolymers and desulfurized precursors. The final dn/dc is derived from the linear fit depending on %PFB for each precursor sample. The obtained final dn/dc´s of the precursor are shown in the 3D plot (right), showing the correlation between %PFB and the dn/dc.

Very low refractive index increment values from 0.049 to 0.052 ml g^{-1} are finally obtained for the precursor polymers, showing the expected correlation between %PFB and the dn/dc. Herein, a behaviour close to isorefractivity was observed for the precursor polymers, a challenging characteristic for optical techniques. Nevertheless, a clear increase of the dn/dc with decreasing PFB decoration was observed.

3.2.3. Refractive Index Increments for the SCNPs dn/dc_{SCNP} (external crosslinker folding)

Online dn/dc determination of the SCNPs was less straightforward than for the precursor samples due non-quantitative mass recovery (average mass recovery values are given in SI Table 8). Due to precise SCNP composition, the dn/dc of the SCNPs is calculated alternatively by treating of the SCNPs as a two-component system (equation SI-8, SI Figure 1, green highlighted linear correlation).

The change of the dn/dc from the precursors to SCNPs can be described by the change of the dn/dc due to incorporation of the number of crosslinker molecules to the precursor backbone. For sake of clarity, we coin the refractive index increment for SCNPs from this strategy dn/dc_{SCNP} within this chapter.

$$\frac{dn}{dc}_{SCNP} = (\%CL)\frac{dn}{dc}_{CL} + (1 - \%CL)\frac{dn}{dc}_{precursor} \tag{SI-8}$$

The dn/dc $_{precursor}$ was observed from the linear correlation as described above (SI Figure 1, top figure), and the refractive index increment of the crosslinker (dn/dc_{CL}) is determined by batch determination. The quantification of the amount of incorporated crosslinker is described in chapter 3.5.4.

In contrast to the correlation of the dn/dc $_{precursor}$ with the functional group decoration %PFB for precursor (open dots in SI Figure 4, linked *via* a black dotted line as guide for the eye), the dn/dc_{SCNP} increases with increasing

amount of incorporated dithiol-crosslinker, likewise expected for polarizable material components like thiols (full dots in SI Figure 4, linked *via* a grey dotted line as guide for the eye).
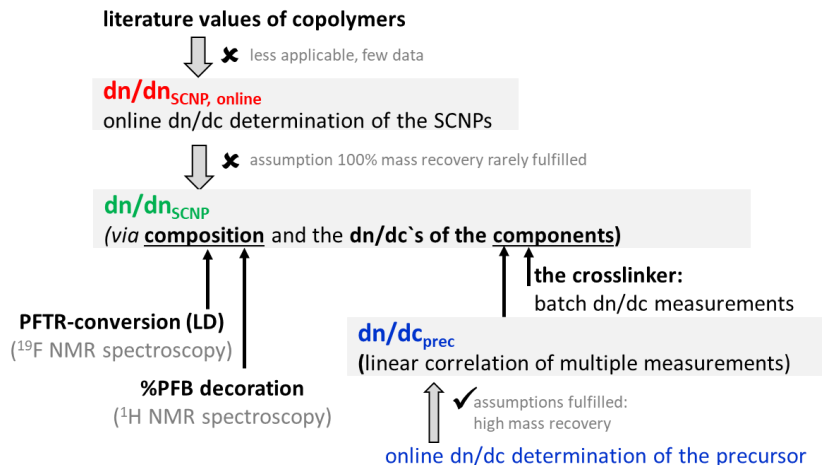
SI Figure 3. Flowchart of the strategy for dn/dc$_{SCNP}$ determination. As neither literature references nor online determination (bold red lettern) are suitable, the dn/dc$_{SCNP}$ (bold green letter) are derived by consideration of the SCNPs as a two-component system.
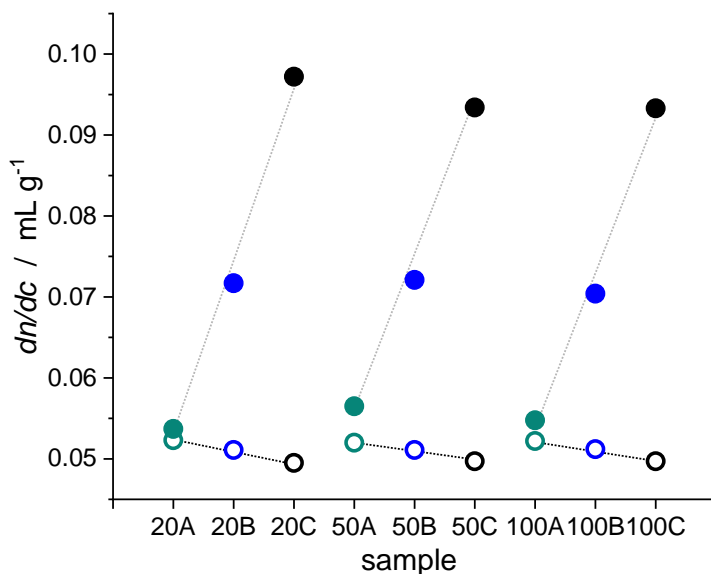
SI Figure 4. Summary of the results of the dn/dc determination for the precursor (open dots, linked via black dotted line as guide for the eye) and their corresponding SCNPs (full dots, linked via grey dotted line as guide for the eye), ordered by increasing LD (samples A, B, C) and molar mass (20kDa, 50kDa, 100kDa).

The incorporation of the crosslinker due the PFTR transformation changes the dn/dc from the precursor to the corresponding SCNP only slightly for the A-samples (SI Figure 4, green data points), medium for the B samples (blue), and significant for the high decorated C-samples (black). As significant changes of the dn/dc values are observed due to crosslinker incorporation, the comprehensive *dn/dc* determination is a prerequisite for accurate molar mass determination, especially for SCNP material obtained from external crosslinker folding strategies.

3.3. Synthesis of the Monomer Pentafluorobenzyl Acrylate (PFBA)

Pentafluorobenzyl acrylate (PFBA) was synthesized *via* a one-pot nucleophilic substitution reaction according the procedure of Roth *et al*. as shown in SI Figure 5.[3]
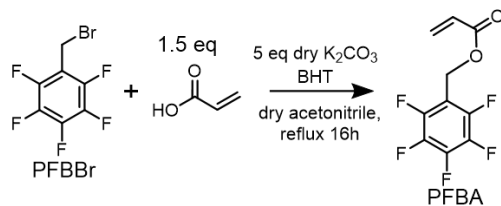

SI Figure 5. Reaction scheme of the monomer synthesis of pentafluorobenzyl acrylate (PFBA).

Excess of potassium carbonate (13g, 5 eq) and catalytic amounts of butylhydroxytoluol (BHT) were stirred in an dried three-neck round-bottom flask (evacuated and backfilled with Argon) in dry acetone to add acrylic acid (1.97 mL, 1.5 eq) under inert atmosphere. The suspension was cooled to 0°C to add pentafluorobenzyl bromide (PFBBr, 2.89 mL, 1 eq) dropwise and under vigorous stirring. The mixture was refluxed for 16 h and stirred at ambient temperature for 8 h. The salts were filtered off and a grain of BHT was added to avoid radical reactions during the subsequent solvent removal under reduced pressure. The crude product was dissolved in diethyl ether and extracted four times with water, four times with sodium bicarbonate buffer standard solution (pH 10) and three times with water and brine. The organic phase was dried over $MgSO_4$. The solvent was gently removed under reduced pressure to obtain 4.02 g of a colourless oily product, which was used without any further purifications (83 % yield).

^{1}H NMR (500 MHz, $CDCl_3$) δ/ppm: 6.42 (dd, J = 17.4, 1.3 Hz, 1H, **1a**), 6.10 (dd, J = 17.3, 10.4 Hz, 1H, **2**), 5.87 (dd, J = 10.5, 1.3 Hz, 1H, **1b**), 5.27 (t, J_{HF} = 1.6 Hz, 2H, **4**).

^{19}F NMR (470 MHz, $CDCl_3$) δ/ppm: -142.3 (m, $2F_o$), -152.8 (t, $1F_p$), -161.2 (m, $2F_m$).

^{13}C NMR (125 MHz, $CDCl_3$) δ/ppm: 165.5 (**3**), 145.8 (F_m, $^1J_{CF}$ = 255 Hz, **7**), 142.0 (F_p, $^1J_{CF}$ = 256 Hz, **8**), 137.7 (F_o, $^1J_{CF}$ = 252 Hz, **6**), 132.2 (**1**), 127.5 (**2**), 109.6 (m, **5**), 53.5 (**4**).
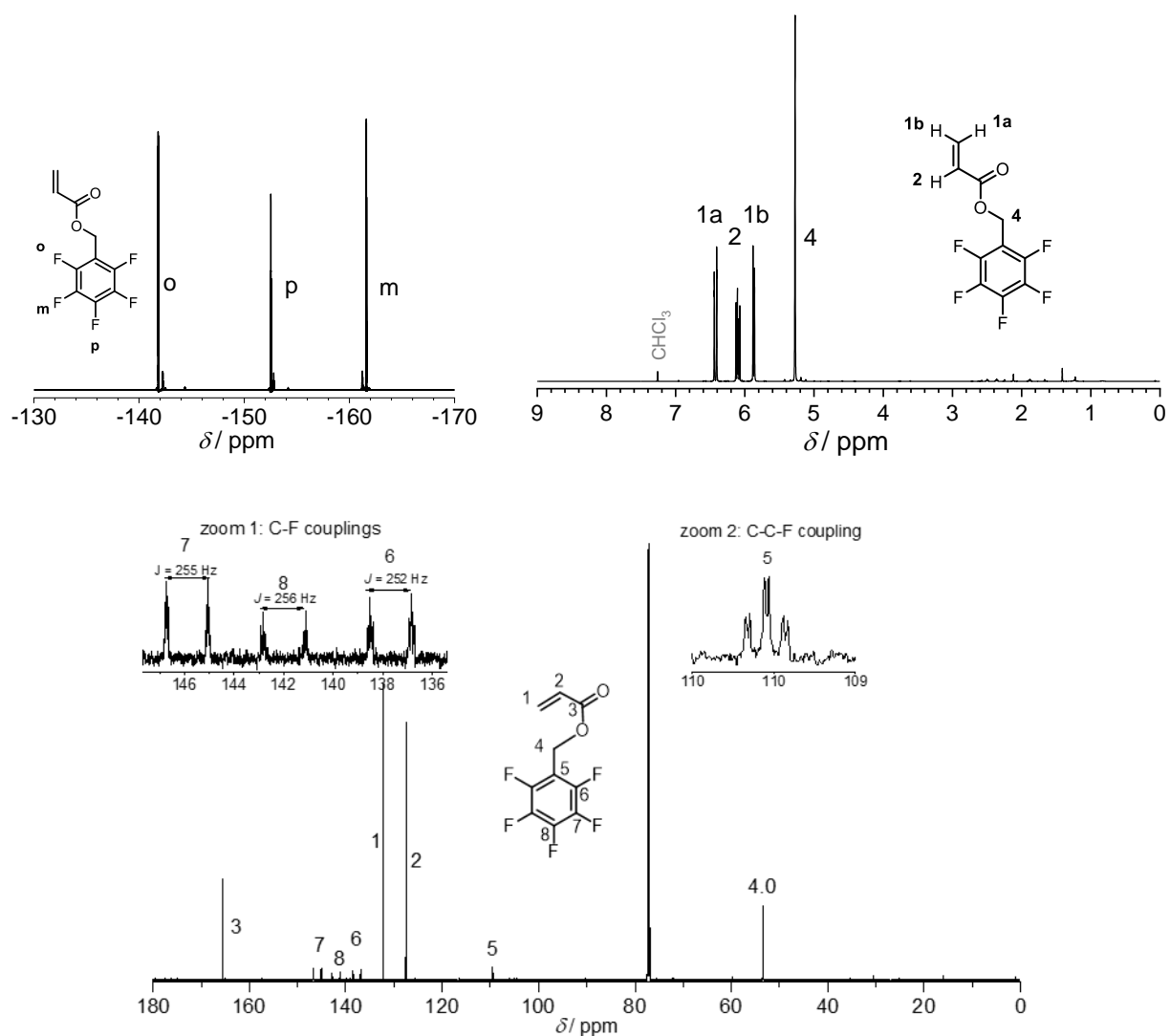
SI Figure 6. ¹H NMR spectrum (500 MHz, CDCl₃, top right), ¹⁹F NMR spectrum (470 MHz, CDCl₃, top left) and ¹³C NMR spectrum (125 MHz, CDCl₃, bottom) of pentafluorobenzyl acrylate (PFBA).

3.4. Precursor Synthesis

3.4.1. General Procedure of Precursor Synthesis (RAFT Polymerization)

Defined poly(pentafluorobenzyl acrylate-*stat*-*tert*-butyl) acrylate copolymers, coined precursors, were synthesized *via* a RAFT polymerization by the use of the the chain transfer agent cyanomethyldodecyl trithiocarbonate (CMDT) as shown in SI Figure 7. Molar amounts and the reactants employed for RAFT polymerization are given in SI Table 2.
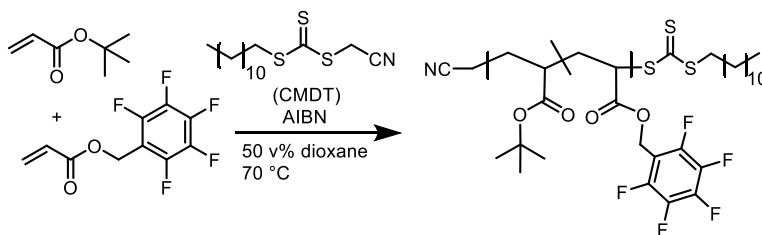
SI Figure 7. Reaction scheme of the RAFT polymerization of poly(PFB-stat-^{t}Bu) acrylate, employed for precursor synthesis. Feed ratios are given in the table below.

General procedure of RAFT polymerization of poly(pentafluorobenzyl-stat-*tert*-butyl) acrylate. An evacuated Schlenk tube was charged with uninhibited pentafluorobenzyl acrylate (PFBA), *tert*-butyl acrylate (^{t}BuA), the chain transfer agent cyanomethyldodecyl trithiocarbonate (CMDT), azobisisobutyronitrile (AIBN, 0.003 eq, stock solution) as radical source, and redistilled dioxane. The Schlenk tube was deoxygenated by four freeze pump-thaw cycles and heated to 70 °C to initiate radical processes. After 23 h the mixture was allowed to cool to ambient temperature and the reaction was quenched by exposing the solution to air. The copolymers were dissolved in as few as possible THF to precipitation three times in at least 50-fold volume excess of cold n-hexane. The solvents were removed under reduced pressure at 40 °C to obtain slightly yellow copolymers, showing powdery to oily viscous appearance in dependency of molar mass and mol% PFB.

SI Table 2. Molar amounts of the monomer tert-butyl acrylate (^{t}BuA) and pentafluorobenzyl acrylate (PFBA), the chain transfer agent cyanomethyldodecyl trithiocarbonate (CMDT), the initiator azobisisobutyronitril (AIBN) and the volume of the solvent dioxane for the RAFT polymerization of defined poly(PFB-stat-^{t}Bu) acrylate copolymers. Colors of the sample´s name of the precursor library samples (underlined in grey) indicate the targeted group decoration according the color code, sample 10a was employed for the optimization of the RAFT end group removal conditions.

	10 a	20A	20B	20C	50A	50B	50C	100A	100B	100C
n_{tBuA} [mmol]	8.582	7.802	7.022	5.461	8.582	7.412	5.461	13.264	15.604	6.242
n_{PFBA} [mmol]	0.954	0.411	1.239	2.341	0.452	1.308	2.341	0.698	2.754	2.675
n_{AIBN} [mmol]	0.009	0.011	0.012	0.013	0.005	0.005	0.005	0.004	0.005	0.003
n_{CMDT} [mmol]	0.043	0.055	0.061	0.065	0.024	0.026	0.026	0.019	0.027	0.015
$V_{dioxane}$ [mL]	0.440	0.502	0.462	0.375	1.122	1.083	0.975	0.853	1.026	0.429

Representative for the precursor library, drawn from polymer **10a**, see SI Figure 78**:**

^{1}H NMR (500 MHz, CDCl$_3$) δ = 5.23 – 4.99 (br s, **10**), 3.33 – 3.19 (m, **15**), 2.48 – 2.00 (br, **3, 8**), 1.87 – 1.12 (br, **2, 7, 6, 16**), 0.80 (t, **17**).

^{13}C NMR (125 MHz, CDCl$_3$) δ/ppm: 174.0 (**4,9**), 145.6 (d, $^1J_{CF}$ = 251 Hz, **13**), 141.6 (d, $^1J_{CF}$ = 257 Hz, **14**), 137.3 (d, $^1J_{CF}$ = 252 Hz, **12**), 109.5 (**11**), 80.2 (**5**), 53.1 (**10**), 42.6 – 39.6 (**3, 8**), 38.2 – 39.6 (**2, 7, 15**), 27.9 (**6, 16**).
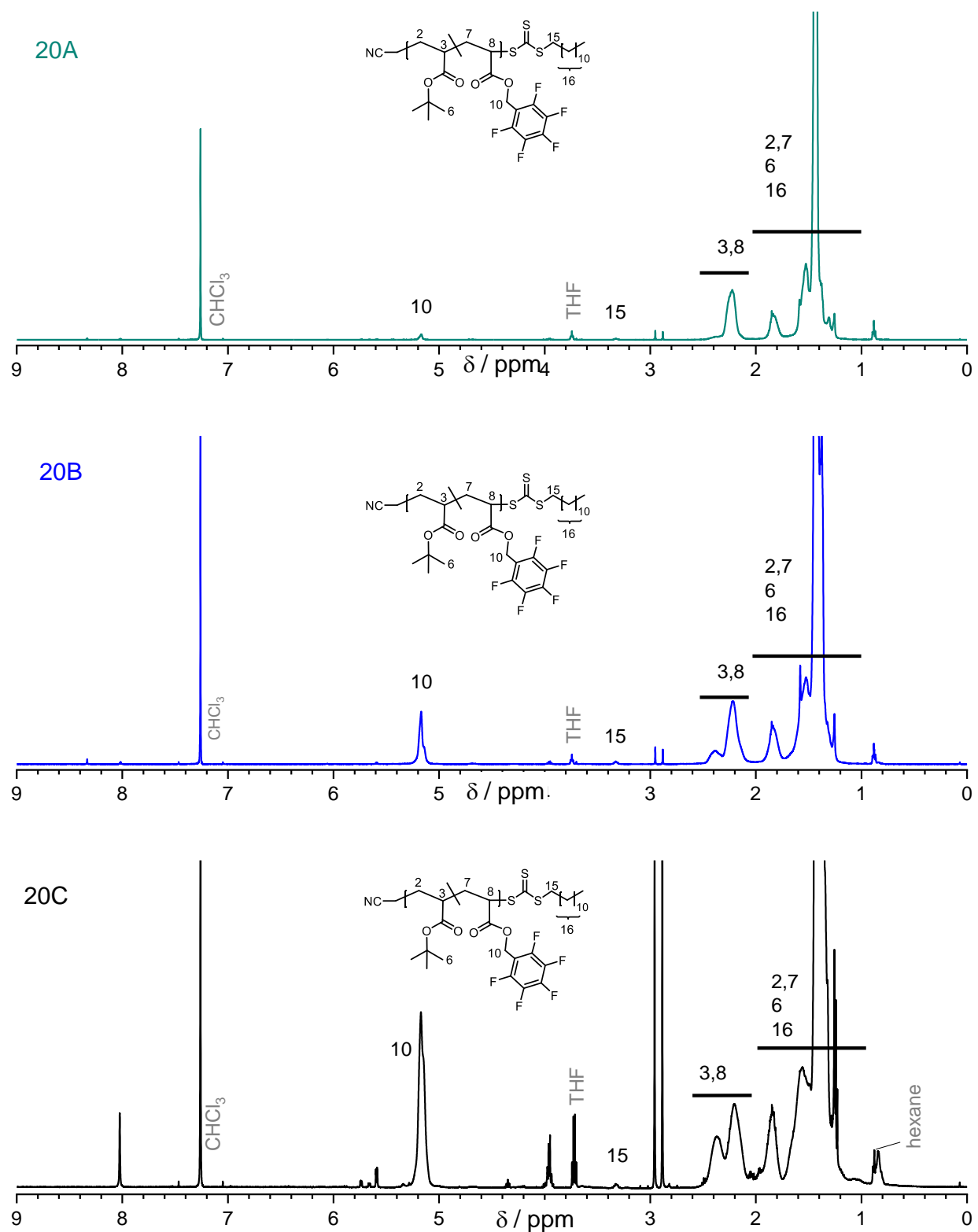
^{19}F NMR (470 MHz, CDCl$_3$) δ = -141.7 – -143.3 (m, 2 F$_o$), -153.6 – -154.7 (m, 1 F$_p$), -162.3 – -163.7 (m, 2 F$_m$).

SI Figure 8. ^1H NMR spectra (500 MHz, CDCl$_3$) of the poly(PFB-stat-^{t}Bu) acrylate samples **20A**, **20B** and **20C** of the approximate molecular weight of 20 kDa, synthesized via RAFT technique. The low decorated A-samples (green, ca. 5% PFB), the middle decorated B-samples (blue, ca.15% PFB) and the high decorated C-samples (black, ca. 30% PFB) differ significantly in the intensity of signal **10**, representative for the methylene group of the PFB. Exact compositions are given in the SI Tables 8-10.
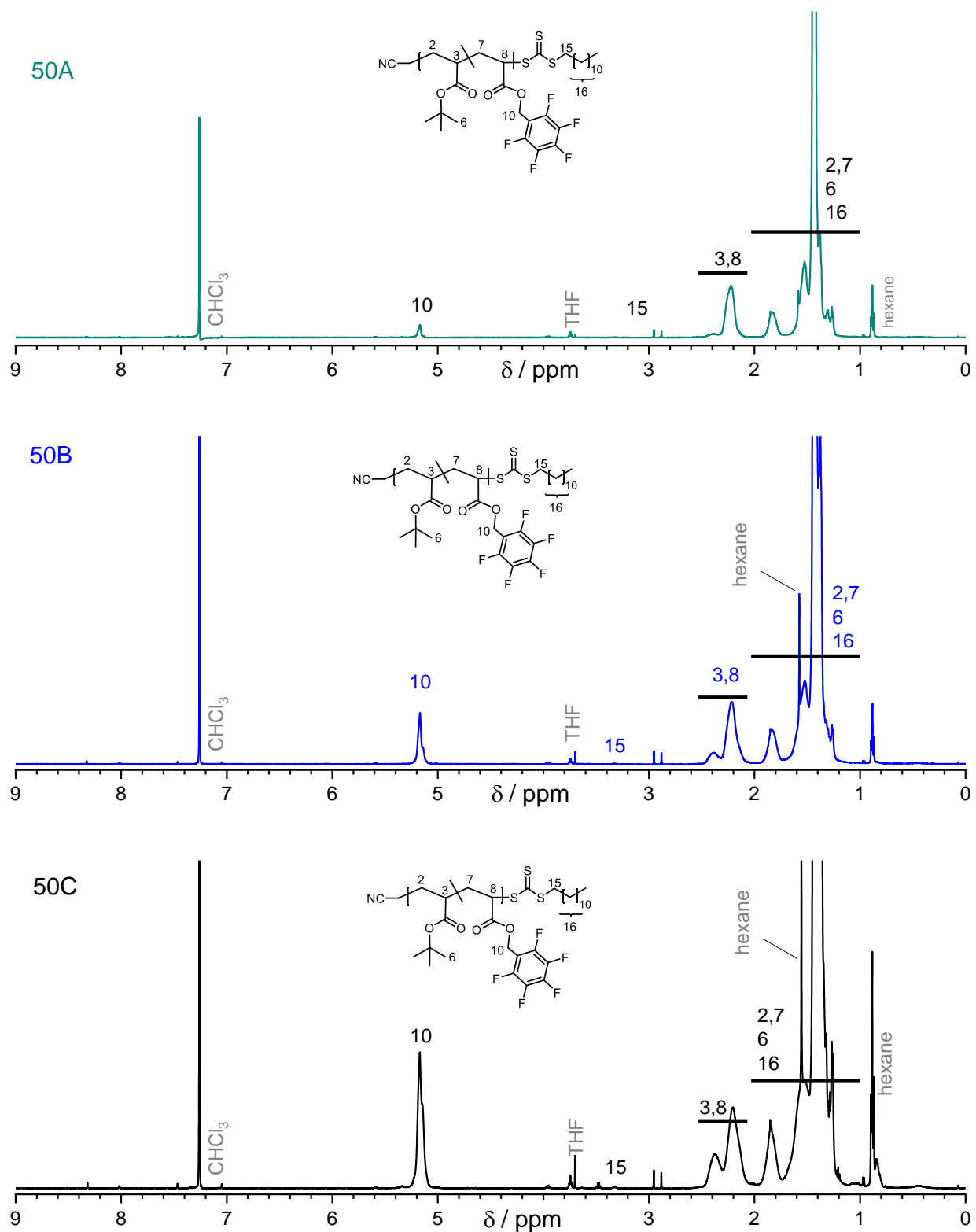
SI Figure 9. ^1H NMR spectra (500 MHz, CDCl$_3$) of the poly(PFB-stat-^{t}Bu) acrylate samples **50A**, **50B** and **50C** of the approximate molecular weight of 50 kDa, synthesized via RAFT technique. The low decorated A-samples (green, ca. 5% PFB), the middle decorated B-samples (blue, ca.15% PFB) and the high decorated C-samples (black, ca. 30% PFB) differ significantly in the intensity of signal **10**, representative for the methylene group of the PFB. Exact compositions are given in SI Tables 8-10.
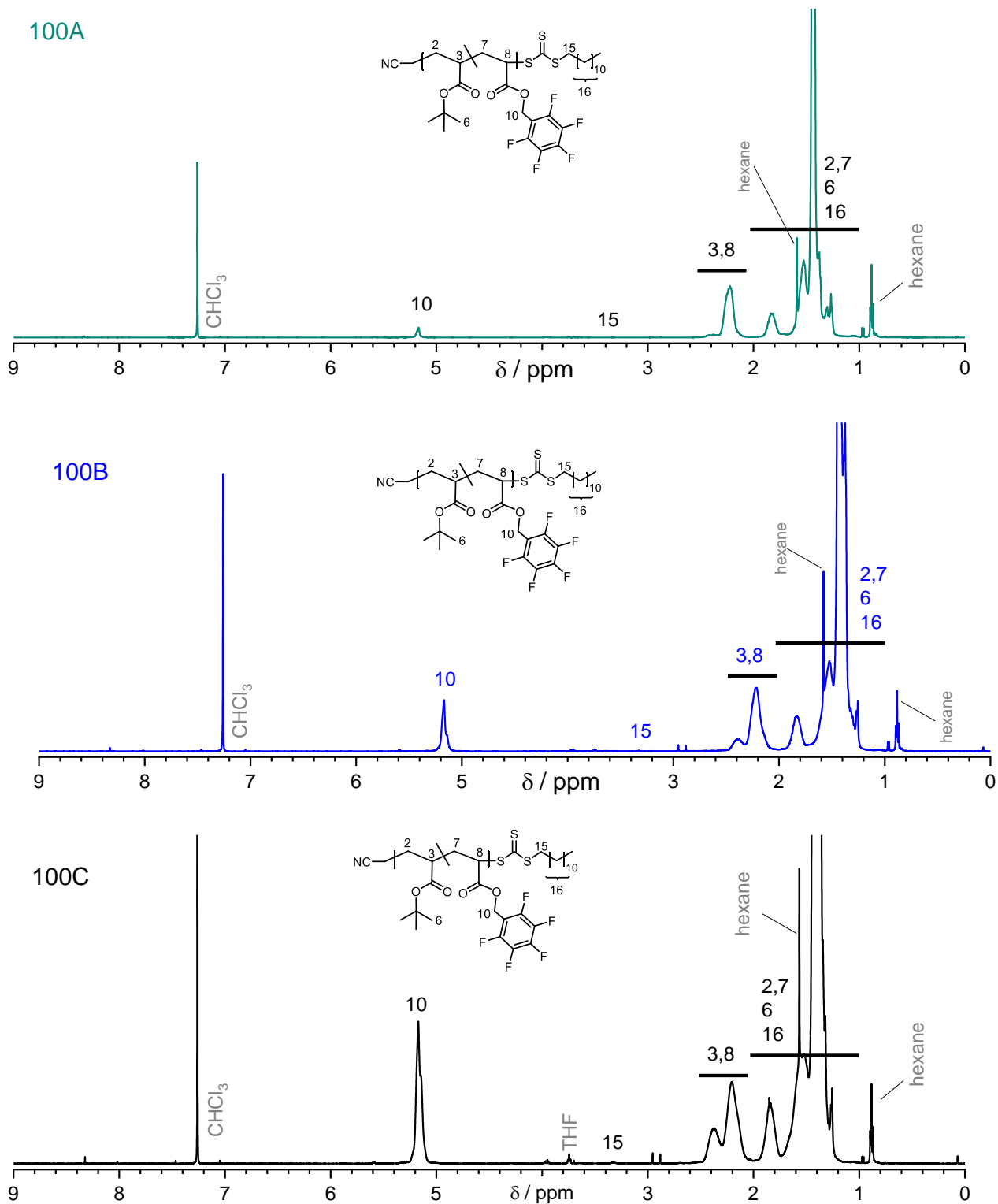
*SI Figure 10. ^1H NMR spectra (500 MHz, CDCl₃) of the poly(PFB-stat-^tBu) acrylate samples **100A**, **100B** and **100C** of the approximate molecular weight of 100 kDa, synthesized via RAFT technique. The low decorated A-samples (green, ca. 5% PFB), the middle decorated B-samples (blue, ca.15% PFB) and the high decorated C-samples (black, ca. 30% PFB) differ significantly in the intensity of signal **10**, representative for the methylene group of the PFB. Exact compositions are given in SI Tables 8-10.*

3.4.2. RAFT End Group Removal

3.4.2.1. General Procedure of RAFT End Group Removal

In contrast to the folding of FRP precursors, detrimental side reactions in SCNP synthesis occurred when applied to defined RAFT precursors of the polymer library. After RAFT end group removal, no such side-reactions occurred anymore, making end group transformation a required *post*-polymerization modification (PPM) for the defined library precursor polymers. RAFT end group transformation as similarly described elsewhere was applied to the whole polymer library according to the following reaction scheme.[4]
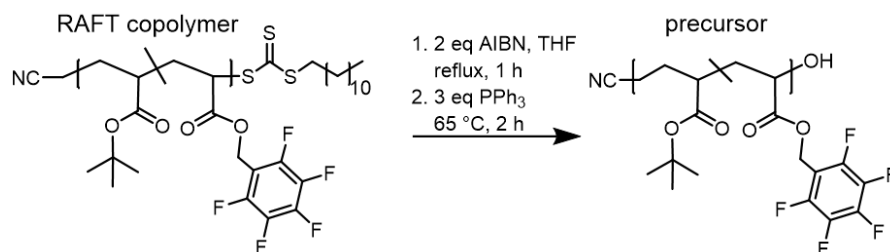

SI Figure 11. Scheme of the general procedure of RAFT end group transformation, applied to the whole precursor library prior the SCNP synthesis.

A solution of poly(PFB-stat-^{t}Bu) acrylate (15 mg/mL) and AIBN (3 eq with respect to the number of RAFT groups) in destilled THF oxygenated by bubbling air through at 65 °C, then refluxed for 2 h under vigorous stirring. After discoloration, the solution was allowed to cool to 55 °C and triphenylphosphine (PPh$_3$, 3 eq with respect to the number of RAFT groups) was added to stir for 2h. The solution was stirred for 1 h at ambient temperature. The reader is cautioned that potentially explosive THF-peroxides are hazardous and liquid solvent waste should be treated accordingly. The copolymer was precipitated three times in at least 50-fold volume excess of cold n-hexane. Residual impurities of THF-derivatives were removed under vacuum at increased temperature (60 °C) overnight. Small amounts of PPh$_3$ could not be removed during precipitation. Colourless copolymers were obtained, appearing in a white powder to viscous oil in dependency of molar mass and molar amount of PFB. Quantitative removal of the RAFT end group is representatively shown for the small copolymer **10a** in the following chapter.

#### 3.4.2.2. Validation of the End Group Removal with a short chain Precursor

To optimize the molar amount of the RAFT group per polymer chain, a short chain poly(PFB-stat-^{t}Bu) acrylate was synthesized. Confirmation of end group conversion with a small copolymer enables RAFT end group quantification *via* ^{1}H NMR spectroscopy and UV-Vis spectroscopy. Furthermore, the observed polymer-stability under applied conditions of RAFT end group removal is representative for the precursor library of the same monomer components. The properties of the small test copolymer **10a** (M$_n$ = 10.6 kDa, Đ =1.14, PFB =10 mol%, characterisation is given in the appendix) are suitable for a representative analysis of the RAFT end group removal.

One-pot radical transformation of RAFT-prepared poly(PFB-stat-^{t}Bu) acrylate polymers into ω-hydroxyl polymers was performed via radical reduction in THF as described above.[4] The disappearance of the RAFT end group characteristic signal at ~ 3.25 ppm in the ^{1}H NMR spectrum confirmed quantitative RAFT end group removal of the small test copolymer **10a** (SI Figure 12).
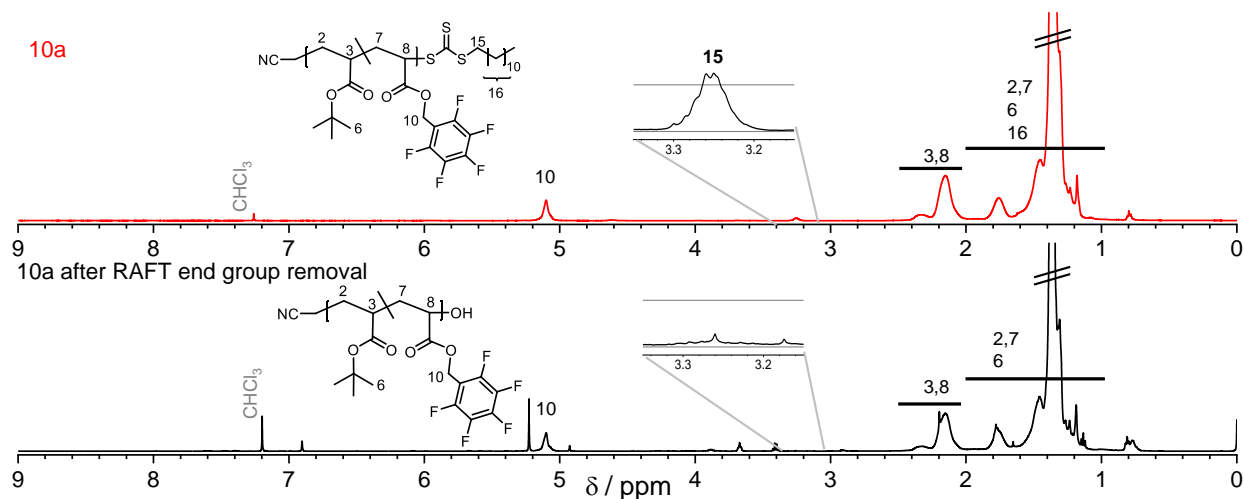
SI Figure 12. ^{1}H NMR spectra (500 MHz, CDCl$_3$) of the copolymer prior (top) and after (bottom) RAFT end group removal. The disappearance of the characteristic signal of the trithiocarbonate end group (3.25 ppm) justifies the success of the removal of the RAFT end group.

Monomodal distribution and the same peak shape in SEC-D4 traces prior and after the end group conversion confirmed the absence of side reactions (SI Figure 13).
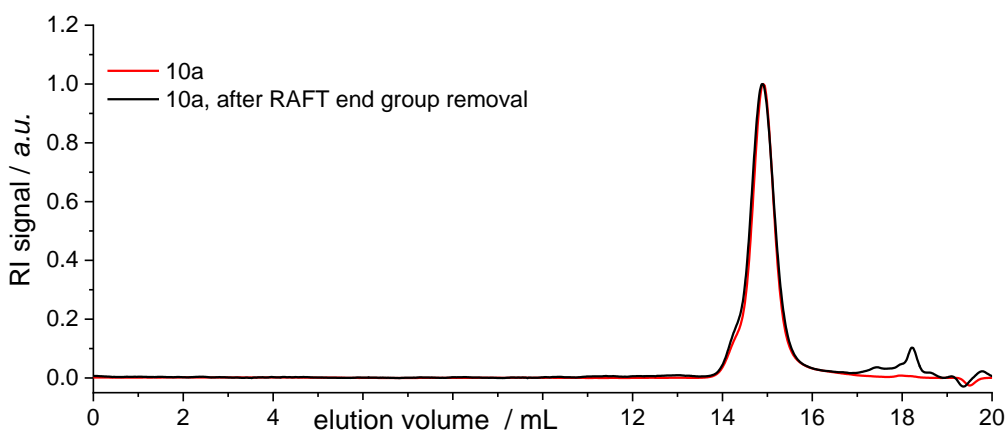
SI Figure 13. The comparison of the dRI trace prior (red) and after (black) end group conversion, obtained from of the SEC-D4 characterization, confirmed the absence of side reactions due to RAFT end group removal procedure.

Confirmation of both the RAFT end group removal and subsequent purification of the side products (mainly thioxanthate derivatives and the degradation products of the THF) is given by UV-vis spectroscopy. The SI Figure 14 shows the significantly decreased of trithiocarbonyl group characteristic adsorption at approximately 308 nm due to the RAFT end group removal for the small test copolymer **10a**.[5,6] The figure shows also, that the quantification of the RAFT characteristic features fades with increasing DP, as the high-molecular weight polymer sample 100B shows slight absorption at 310 nm only. SI Figure 14 shows also the correlation between the absolute number of PFB groups along the chain and the absorbance at 246 nm.
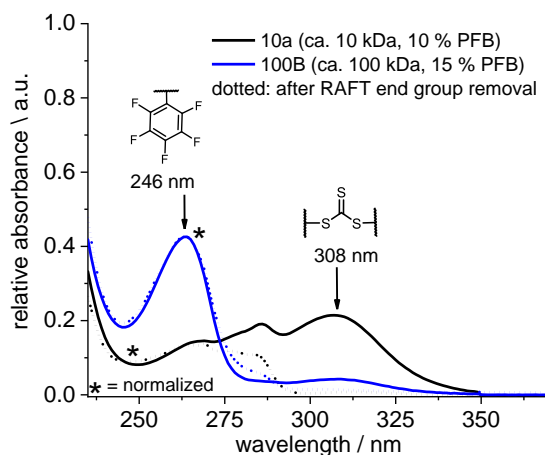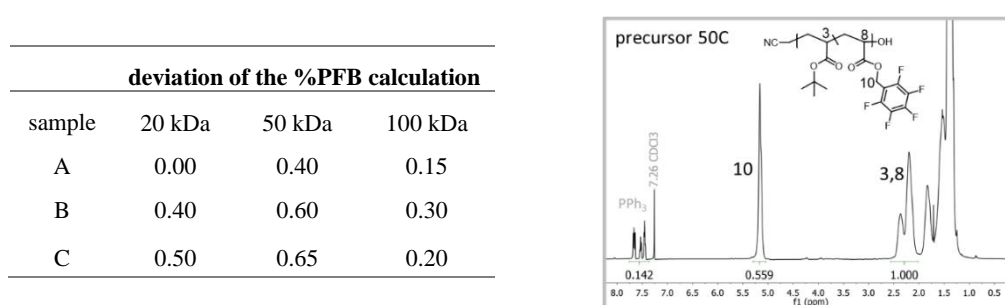
SI Figure 14. The UV-Vis spectra of prior and after RAFT end group removal for the samples 10a (black, small poly(PFB-stat-^{t}Bu) acrylate test copolymer of approximately 10 kDa molar mass) and 100B (blue, library precursor of approximately 100 kDa molar mass) show a significant decrease of UV-Vis absorbance at approximately 308 nm due to the loss of the trithiocarbonyl group. Quantification of the chromophore end groups via UV-Vis analysis is limited to small polymer sample 10a. The UV-Vis adsorption at 246 nm is related to the amount of PFB chain decoration.

Further validation of the new backbone linked hydroxyl group was not performed, as SCNP synthesis was successful with the polymer material after above described procedure.[4] RAFT end group removal was applied to all samples of the precursor library prior SCNP synthesis as described in the following chapter.

### 3.4.3. Evaluation of the precursor composition

The composition of the poly(PFB-stat-^{t}Bu) acrylate polymers of the defined precursor library is calculated from suitable signals in the ^{1}H NMR spectra. SI Figure 15 shows exemplarily the integral regions in the ^{1}H NMR spectrum for the sample 50C, which were employed for the evaluation of the composition of the copolymers. The ratio of the integral of the methylene group signal of the PFB units (**10**; 5.3 - 4.9 ppm) to twice the sum of the integrals of the signals of the methine protons of the polymer backbone (**3, 8**; 2.00 – 2.56 ppm) was employed to quantify the %PFB. The calculation was applied to both the spectra of the RAFT copolymers and to the spectra of the precursor after RAFT end group removal. The deviation of both quantifications is given in the left table of SI Figure 15. The obtained %PFB values are given in the SI Table 8.

	deviation of the %PFB calculation		
sample	20 kDa	50 kDa	100 kDa
A	0.00	0.40	0.15
B	0.40	0.60	0.30
C	0.50	0.65	0.20

*SI Figure 15. Results of the %PFB quantification of the composition of the poly(PFB-stat-tBu) acrylate copolymers via ^{1}H NMR spectroscopy (left) with the exemplary ^{1}H NMR spectrum (500 MHz, CDCl$_3$) of sample 50C to the right. The signals relevant for quantification of the copolymer composition are the methylene group of the PFB unit (**10**) and the methine backbone signals (**3, 8**). Low average deviation (bottom rows of the table) of the quantification applied to the spectra before and after the RAFT group removal validates the reliability of the evaluated copolymer composition.*

3.4.4. Structures of the Precursor Copolymers

Upon SEC-D4 and ^{1}H NMR characterization, the SI Figure 16 shows the obtained copolymer composition, the M_n and the Đ values for all precursor library samples. The %PFB is given next to the sample´s name on the top of each structure, whereas the absolute composition of the poly(PFB-*stat*-^{t}Bu) acrylate copolymers and results of SEC-D4 characterization are given below.
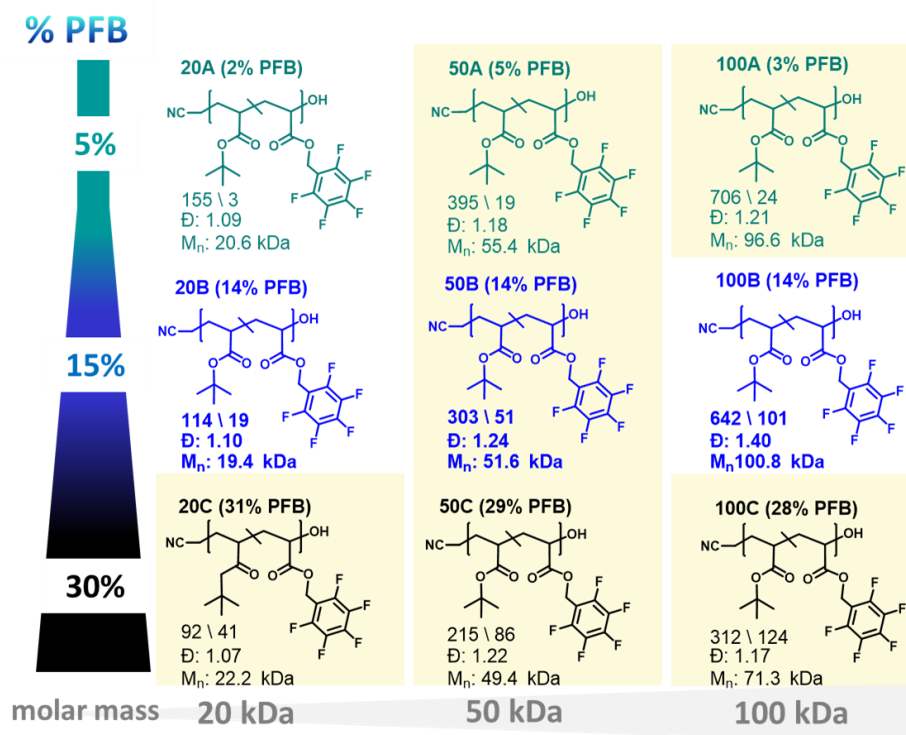
SI Figure 16. Structures of the precursor library poly(pentafluorobenzyl-stat-tert-butyl) acrylate (short: poly(PFB-stat-^{t}Bu) acrylate), synthesized via statistic RAFT polymerization and subsequent RAFT end group removal. The mol% PFB is given next to the sample´s name on the top of each structure, whereas the absolute composition and results of SEC-D4 characterization (number weighed molar mass M_n and polydispersity Đ) are given below each structure.

3.5. SCNP synthesis

3.5.1. Optimization of the Folding Reaction with FRP-Copolymers

The optimization of the PFTR-induced folding of SCNPs turned complex regarding the parameters of polymer solubility *vs.* the optimal solvent conditions to support PFTR thermodynamics, the employed base *vs.* the reaction time, and the reaction time *vs.* side reactions (disulfide linkage). A thermally induced free radical polymerization (FRP) polymerized poly(PFB-stat-^{t}Bu) acrylate polymer with comparable composition regarding the defined library precursor (the structure is shown in SI Figure 76) serves to optimize the parameters and conditions of the folding reaction of the defined precursor library for reasons mentioned in the chapter of FRP synthesis. The optimization of the folding procedure was performed in the order of setting the precursor concentration, the solvent conditions, the amount of base, the crosslinker concentration, the reaction time and the required amount phosphine reducing agent to suppress thiol-thiol interaction.

The concentration of the external crosslinker is related to the absolute number of functional PFB monomer units in solution under folding conditions. The concentration of the precursor is dictated by the requirement high dilution to avoid inter-chain interaction during the folding reaction in turn. No multi chain nanoparticles were observed for a precursor concentration of 0.5 mg mL^{-1} during folding reaction, justified by the MALS signal trace of SEC-D4 characterization.

Attempts to increase the reaction rate by the use of the stronger base 1,8-diazabicyclo [5.4.0] undec-7-ene (DBU) instead of the weak base TEA were not successful. [7–10] Keeping ambient reaction temperature during the folding reaction, we observed no multiple fluorine-substitution even for excess of reactants (thiol and base) and long reaction time if TEA is employed as base. To reduce PFTR reaction time for SCNP synthesis, excess of TEA (4 vol%) appeared at once beneficial to achieve good solvent conditions of the precursor.[3,9–11] Polar solvent acetonitrile (ACN) was employed as main solvent to support for the PFTR reaction rate during SCNP synthesis. Complete solubility of the precursor required the addition of THF as described in the main text. The amount of THF was found to depend on the chain-length and polymer composition. The same solvent ratio (approximately ACN/THF: 0.2/0.8) was applied to all precursor of the same approximate molar mass (20 kDa, 50 kDa, 100 kD to keep comparable reaction conditions. Noteworthy, the precursors with a lower PFB decoration showed already complete solubility below the required amount of good solvent for the higher decorated precursors within the mass-groups.

The use of an external crosslinker facilitates to modify the concentration of the crosslinker with regard the functional group decoration of the precursor. Excess of the thiol-crosslinker was not successful to increase the reaction rate of the PFTR, as at once increasing probability of competing thiol-thiol interaction and concomitant requirement of larger amounts of reducing agents were true. Herein, we employed one equivalent of thiol (0.5 eq of crosslinker) regarding the number of PFB units.

To compensate for the rather slow reaction rate of PFTR by use of the weak base TEA and the restriction to work under lowest possible thiol concentration, long-time SCNP synthesis was performed. We observe high PFTR turnover within three days of SCNP folding.

The reducing agent triphenylphosphine (PPh$_3$) showed less suitable, as required high amount of PPh$_3$ for suppression of competing thiol-thiol interaction accumulated in the polymer product material and purification appeared challenging. Higher efficiency of PFTR reaction at the pendant PFB units was observed by use of the stronger reducing agent dimethylphenylphosphine (DMPP), like described elsewhere.[12,13] To avoid the disulfide linkage (or aggregation, respectively) of unreacted thiols after SCNP synthesis, scavenging of unreacted thiols was applied *prior* purification of the polymer material. Already infinitesimal amounts of possibly residual grafted thiols along the polymer chain may have impacted the elution behavior during the SEC separation, as thiols tend to undergo column interaction.[14] Herein, the folding reaction was quenched by scavenging yet unreacted thiols with methylacrylate (MA). The requirements of the Michael Addition are in good agreement to the folding conditions,

especially the presence of DMPP.[15] To avoid the oligomerization of the thiol scavenger MA in turn, a catalytic amount of butylhydroxytoluol (BHT) was added prior polymer purification.

3.5.2. Experimental of SCNP Folding

From optimization described in the previous chapter, a facile set-up for the sequence for SCNPs synthesis was established. SI Figure 17 shows the sequence, starting with solving the precursor in solvents (1) and base (2), followed by dropwise release of the crosslinker, diluted in a reducing agent DMPP containing stock solution (3). After deoxygenation, the PFTR reaction was performed at ambient temperature for three days (4). The folding reaction was quenched by addition of the Michael acceptor methacrylate to stir for several hours at ambient temperature (5). Solvents and reactants were removed (6) to precipitate the residual polymer in cold n-hexane and separate the side products and excess compounds (7). After drying the SCNPs (8), characterization of the SCNPs is performed.
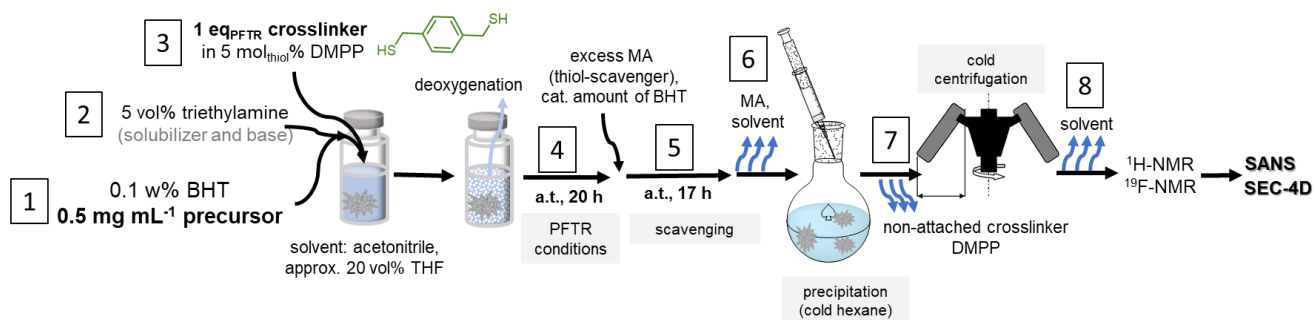
SI Figure 17. Scheme of the experimental procedure of SCNP synthesis.

3.5.3. General Procedure of SCNP Synthesis

SCNP synthesis was applied for the precursor material after RAFT end group transformation, as described in chapter 3.4.2.

THF was added dropwise within 1 h to the precursor poly(PFB-stat-^{t}Bu) acrylate (0.5 mg mL^{-1}) in acetonitrile until the solution became transparent. Triethylamine (TEA, 2 vol%) was added slowly.

The external crosslinker 1,4-benzenedimethanethiol (BDMT, 1 eq with respect to the pendant PFB groups of the precursor) was dissolved with the reducing agent dimethylphenyl phosphine (DMPP, 0.1 eq with respect of the thiol groups of the crosslinker BDMT) in THF to add the thiol solution dropwise to the stirring precursor solution of 20 vol% THF in total. Finally, further 3 vol % TEA was added slowly. The solution was stirred at ambient temperature for three days. Excess of methacrylate (MA) and a catalytic amount of butylhydroxytoluol (BHT) was added and the solution was stirred for 16 h at ambient temperature. The solvents and the base were removed. The copolymer was dissolved in as few as possible THF to precipitate three times in at least 50-fold volume-excess of cold n-hexane. The solvents were removed to obtain SCNPs, as a white powder (SCNPs of approximately 50 kDa and 100 kDa) or amorphous character (true for the high decorated SCNP samples of the lowest PD f20B and f20C)

SI Table 3. Identity and molar amounts of the crosslinker 1,4-benzenedimethanethiol (BDMT), the additives (base triethylamine [TEA], reducing agent [DMPP], radical inhibitor [BHT], methacrylate [MA]), and the solvents (acetonitrile [ACN] and tetrahydrofuran [THF]) employed for synthesis of SCNPs from the starting material of the (poly(PFB-stat-^{t}Bu) acrylate precursor library material (vertical sample names according the color code).

|		m mg	n mmol	c mM	V mL		m mg	n mmol	c mM	V mL		m mg	n mmol	c mM	V mL
precursor		200	0.01	0.026	400		250	0.005	0.011	500		250	0.003	0.006	500
DMPP		0.86	0.006	0.016	0.001		2.33	0.017	0.034	0.002		1.73	0.013	0.025	0.002
BHT (0.1 w%)		0.31					0.39					0.39			
BDMT (1 eq$_{PFB}$)	20A	5.29	0.031	0.078		50A	14.34	0.084	0.168		100A	10.64	0.063	0.125	
ACN					297					362					366
THF (20 vol%)					74					91					92
TEA (5 vol%)					20					25					25
excess MA					1					4					3
precursor		200	0.011	0.027	400		250	0.005	0.011	500		200	0.003	0.007	400
DMPP		5.38	0.039	0.097	0.006		6.8	0.049	0.098	0.007		5.2	0.038	0.094	0.005
BHT (0.1 w%)		0.31					0.39					0.31			
BDMT (1 eq$_{PFB}$)	20B	33.14	0.195	0.486		50B	41.92	0.246	0.492		100B	32.05	0.188	0.47	
ACN					265					331					266
THF (20 vol%)					66					83					67
TEA (5 vol%)					20					25					20
excess MA					8					10					8
precursor		200	0.01	0.025	400		250	0.006	0.012	500		250	0.004	0.008	500
DMPP		10.27	0.074	0.186	0.011		12.08	0.087	0.175	0.012		12	0.087	0.174	0.012
BHT (0.1 w%)		0.31					0.39					0.39			
BDMT (1 eq$_{PFB}$)	20C	63.33	0.372	0.93		50C	74.43	0.437	0.874		100C	73.96	0.434	0.869	
ACN					231					294					295
THF (20 vol%)					58					74					74
TEA (5 vol%)					20					25					25
excess MA					16					19					19

^{1}H NMR spectroscopy confirmed the incorporation of the crosslinker (signal **1,16** in the SI Figures 18 - 25); ^{19}F NMR spectroscopy confirmed the turnover of the PFTR χ_{PFTR} (SI Figure 29), and SEC-D4 showed the changes of the elution behaviour, characteristic for SCNP formation (see chapter 4.2.2).
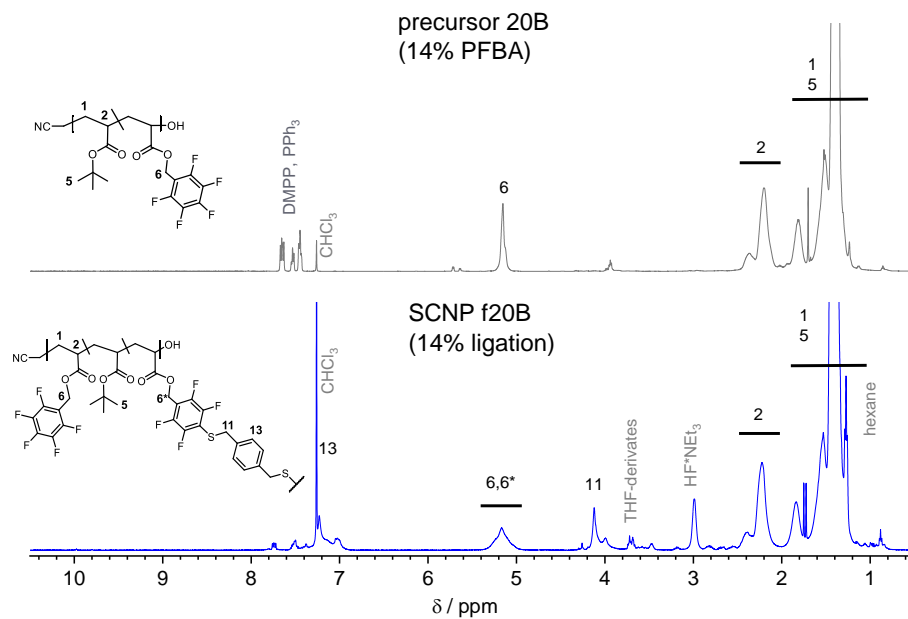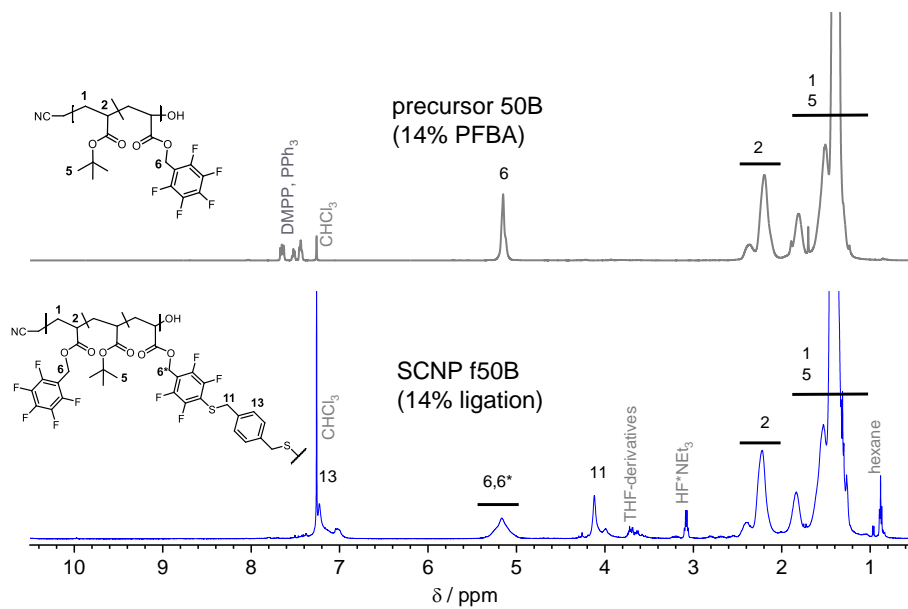
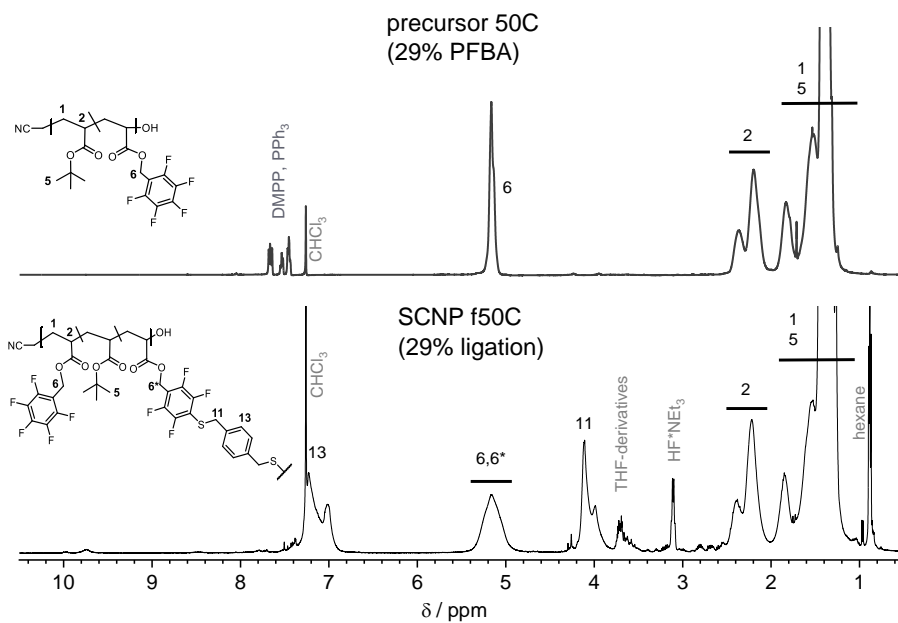*SI Figure 18. Stacked ^1H NMR spectra (500 MHz, CDCl$_3$) of the precursor 20B (top) and the SCNP f20B (bottom).*
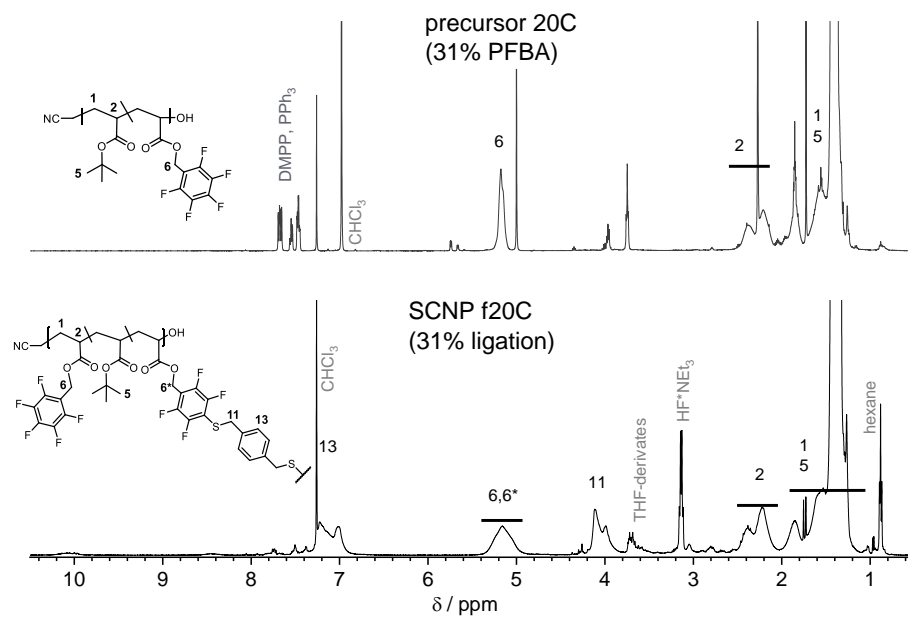
SI Figure 19. Stacked ^1H NMR spectra (500 MHz, CDCl$_3$) of the precursor 20C (top) and the pairing SCNP f20C (bottom).
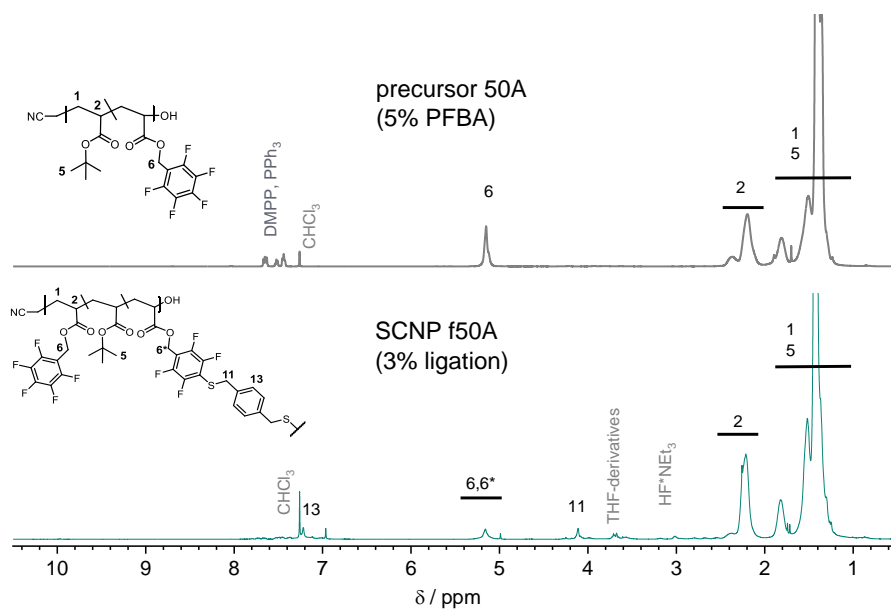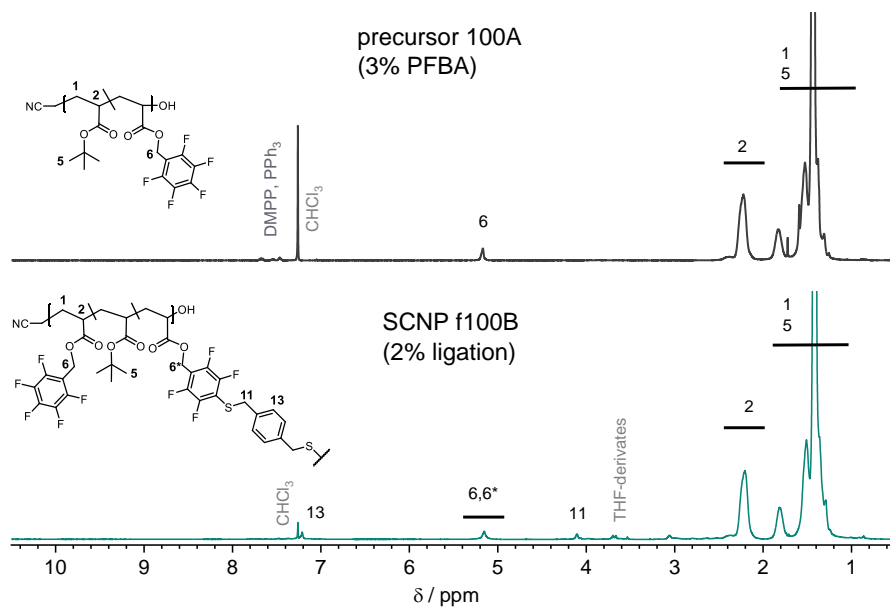
SI Figure 20. Stacked ^1H NMR spectra (500 MHz, CDCl₃) of the precursor 50A (top) and the pairing SCNP f50A (bottom).

SI Figure 21. Stacked ^1H NMR spectra (500 MHz, CDCl₃) of the precursor 50B (top) and the pairing SCNP f50B (bottom).

SI Figure 22. Stacked ¹H NMR spectra (500 MHz, CDCl₃) of the precursor 50C (top) and the pairing SCNP f50C (bottom).
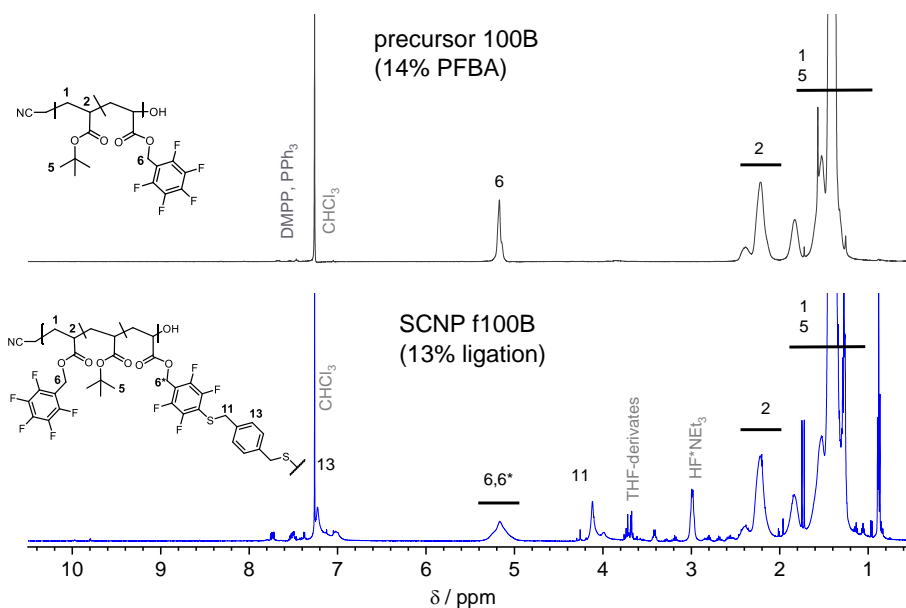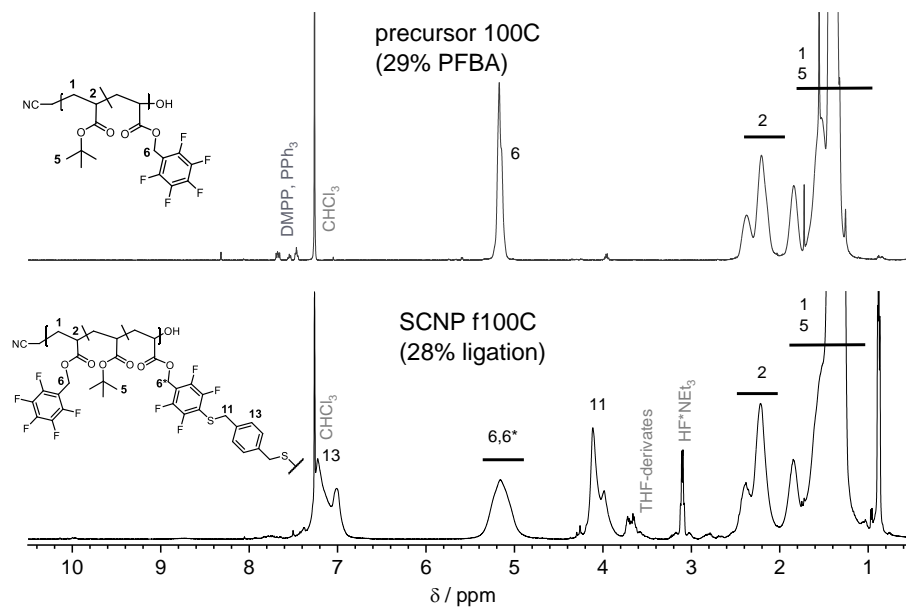

SI Figure 23. Stacked ¹H NMR spectra (500 MHz, CDCl₃) of the precursor 100A (top) and the pairing SCNP f100A (bottom).
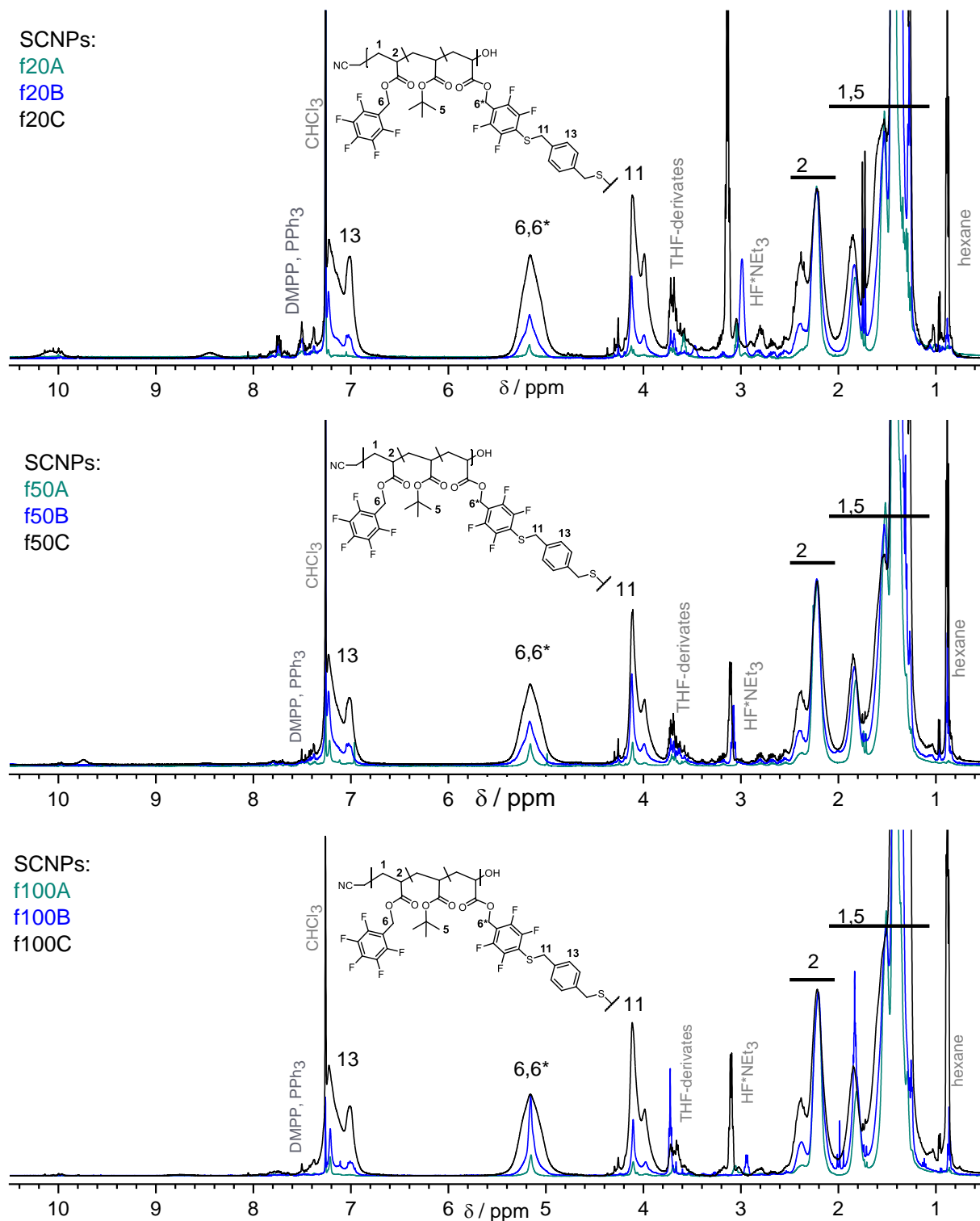
SI Figure 24. Stacked ¹H NMR spectra (500 MHz, CDCl₃) of the precursor 100B (top) and the pairing SCNP f100B (bottom).

SI Figure 25. Stacked ¹H NMR spectra (500 MHz, CDCl₃) of the precursor 100C (top) and the pairing SCNP f100C (bottom).

SI Figure 26 shows the increasing intensity of the signals characteristic for incorporated crosslinker (signals **11** and **13**) in the order C-, (black) > B-, (blue) > A-, (turquoise), visible by the overlay of the ¹H NMR spectra of the SCNPs for each molar mass group (20 kDa on the top, 50 kDa in the middle, 100 kDa spectrum on the bottom). The trend of intensity if the crosslinker-correlated coincides as expected with the %PFB (signal **6, 6***). The amount of the incorporated crosslinker molecules follow.

*SI Figure 26. Labelled polymer structure and ^1H NMR spectra (500 MHz, CDCl$_3$) of the SCNPs for the approximately 20 kDa samples (middle), 50 kDa samples (middle) and 100 kDa samples (bottom). Side products of the reducing agents of the previous RAFT-group removal (PPh$_3$, THF derivates) and the side products of the folding reaction (DMPP and HF*TEA) are labelled in grey.*

3.5.4. Evaluation the SCNP Composition (LD, absolute composition, loop length)

Conversions of *para*-fluoro thiol reaction (PFTR) are evaluated *via* ^{19}F NMR spectroscopy as described in the main text. The characteristic change of the ^{19}F NMR signals is shown in SI Figure 29. The *para* signal disappears (F_p, 154 ppm), the appearance of the F^- signal is found to depend on the employed base and the base concentration (SI Figure 27, highlighted in blue), as discussed in literature.[10] The *ortho* signal (F_o, 143.0 ppm) and the *meta* signal (F_m, 163 ppm) are shifted upfield to the turnover signals (F_o', 142 ppm and F_m', 135 ppm; see red arrows in SI Figure 29).
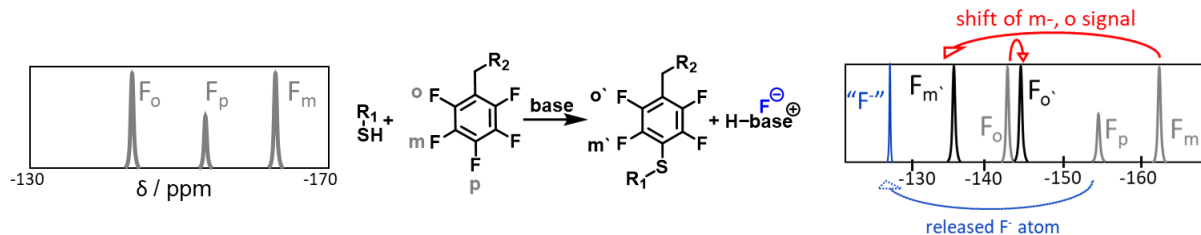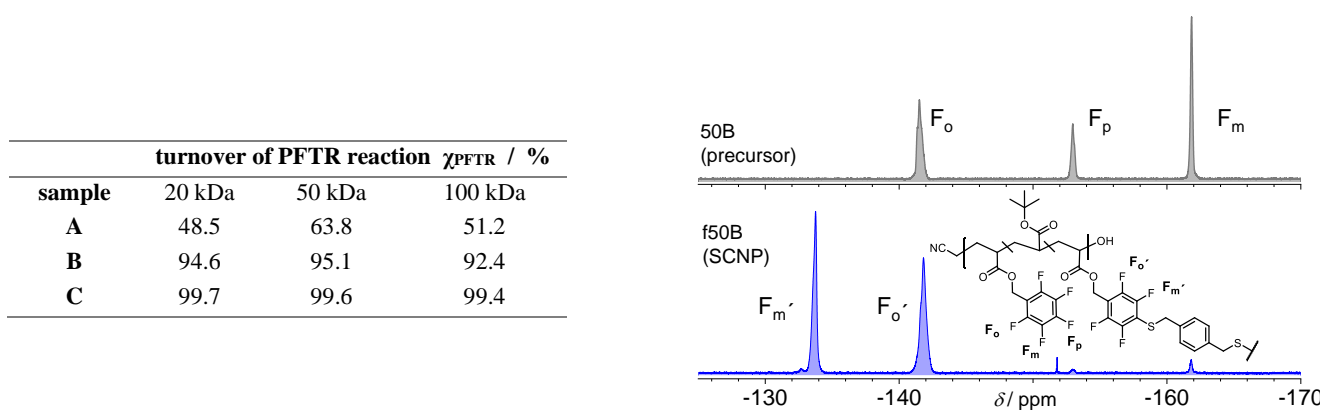

SI Figure 27. The schematic representation of the para-fluoro thiol reaction (PFTR) characteristic changes in the ^{19}F NMR spectrum prior (left) and after (right) the substitution reaction. The general scheme of the PFTR for PFB units is shown between the spectra, colours assist for referencing to the corresponding spectral changes (grey, blue). The changes suitable for quantification are highlighted in red. The signal integrals of the meta signals of unreacted (F_m) and reacted PFB unit (F_m') were employed for quantification of the PFTR turnover.

The ratio of the integrals of characteristic *meta* signals were employed for PFTR quantification for reasons described in the main text, exemplarily shown for the ^{19}F NMR spectrum of the SCNP sample f50C (SI Figure 28). The calculated turnover of the PFTR χ_{PFTR} of all samples are given in the top rows of the table in SI Figure 28. Based on the relative amount of PFB groups in the precursor chain (%PFB) and the PFTR conversion (χ_{PFTR}), the ligation density LD is a useful measure for SCNPs (see SI-9).

$$LD = \chi_{PFTR} * \%PFB \qquad (SI-9)$$

The LD for all SCNPs samples of the polymer library is summarized in SI Figure 28 (right table, shaded) and directly related to the χ_{PFTR}, obtained from ^{19}F NMR spectroscopy. The values of LD are rounded to the last decimal place according to the experimental error (by phase and baseline correction for the Fourier transformed spectra *etc.*).

	turnover of PFTR reaction χ_{PFTR} / %		
sample	20 kDa	50 kDa	100 kDa
A	48.5	63.8	51.2
B	94.6	95.1	92.4
C	99.7	99.6	99.4

SI Figure 28. Left: The exemplary ^{19}F NMR spectrum (470 MHz, CDCl₃) of sample f50B, showing the signals relevant for the quantification of the PFTR conversion. The para (F_p) signal diminishes, whereas the meta (F_m), and ortho (F_o) signals shift to the turnover signals (F_m' and F_o'). From the obtained PFTR conversion, the LD can be calculated. The ^{19}F NMR spectra of all samples are shown in the following figure.

SI Figure 29 shows the ^{19}F NMR spectra of the all SCNPs (a, b and c), which allow to derive the χ_{PFTR} and the LD according equation SI-9, respectively. The lower χ_{PFTR} for the low decorated SCNPs (A-samples approximately

60% PFTR, see SI Figure 28) in contrast to all higher decorated SCNPs (B-, and C samples) is indicated by the variance of the obtained LD (SI Figure 29 d, crosses) to the %PFB (SI Figure 29 d, bars). Herein, lightly crosslinked (2% < LD < 5%), green), medium crosslinked (15% LD, blue) or tightly crosslinked (30 mol% LD, black) SCNPs are obtained.
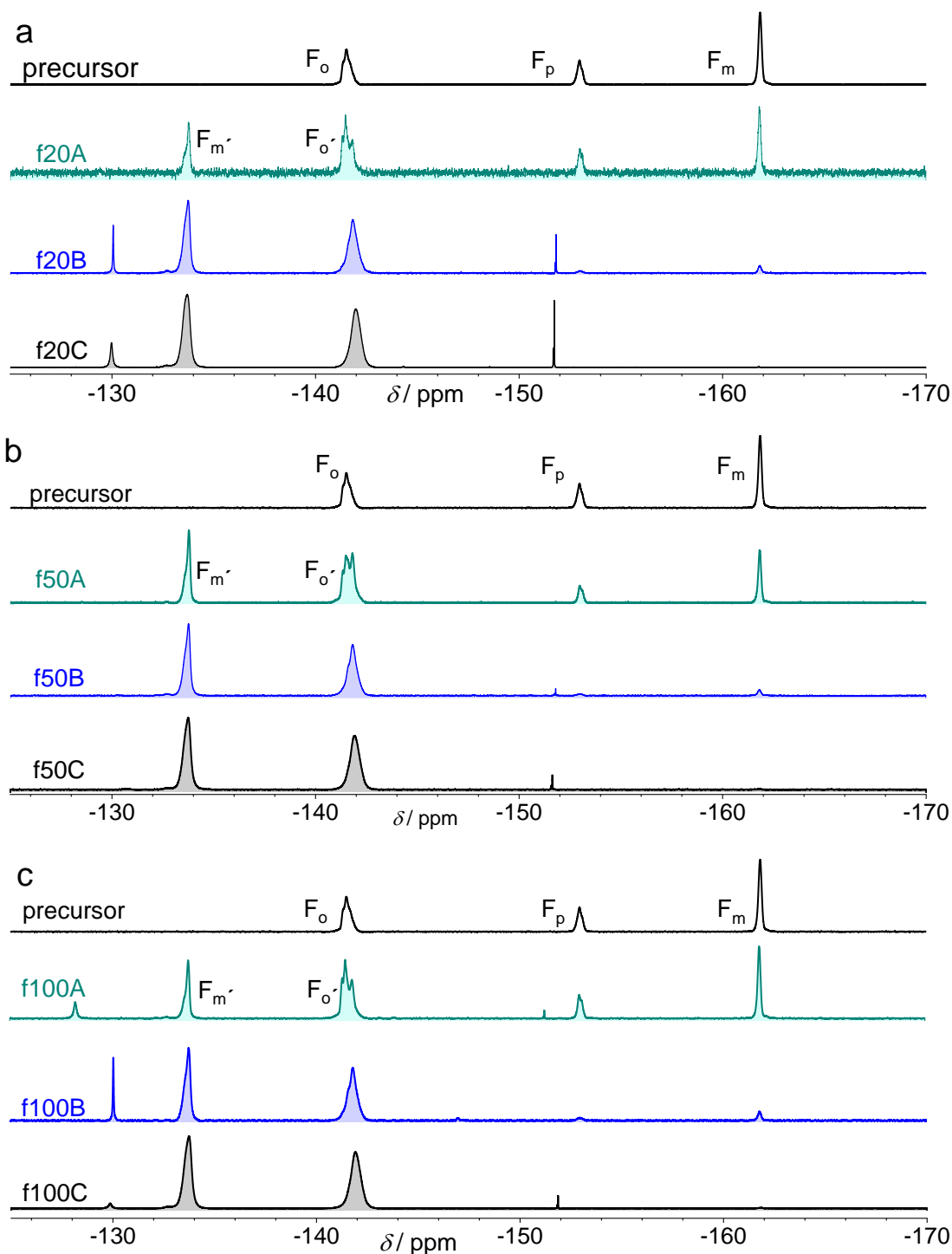
SI Figure 29. ^{19}F NMR spectra (470 MHz, CDCl$_3$) of the small (a, approximately 20 kDa), middle (b approximately 50 kDa) and large (c, approximately 100 kDa) the SCNPs of the polymer library. The color code indicates the functional group decoration. The turnover ratio of the integrals of the of the meta fluorine signals allow for calculation of the PFTR conversion χ_{PFTR} of the pendant PFB groups or the LD, respectively.

Under assumption of exclusively two-side attached crosslinker molecules as discussed in the main text, the number of ligation points is twice the amount of crosslinker per chain under assumptions described in the main text (SI-10a). Assuming statistical character of the precursor polymers, the SCNPs formed via a double sided attached crosslinker molecules means that the number of loops equals the average number of crosslinker per SCNP n_{CL} (SI-10b), the compactness can be estimated by the measure of the average loop length. The relative measure of the %PFB and the PFTR turnover (χ_{PFTR}) of the PFB groups turns then into the average loop length $n_{loop,av}$ as described in equation (SI-10c).

$$\%CL = (LD)/2 = (\chi_{PFTR} * \%PFB)/2 \qquad \text{(SI-10a)}$$

$$n_{CL} = DP \cdot \%CL \qquad \text{(SI-10b)}$$

$$l_{loop,av} = DP/n_{CL} = DP/\left(\frac{\%PFB \cdot \chi_{PFTR}}{2}\right) \qquad \text{(SI-10c)}$$

The SI figure 30 displays the average absolute measures of the number of crosslinker per SCNP n_{CL} (colored crosses, corresponding to the left axis), which turns to the average loop length $l_{loop,av}$ (red bars corresponding the right red axis), quoted by the number of monomer units per loop. Under assumptions described in the text, the measure of the average loop length can be considered as a measure of deformability of the SCNPs as discussed in the main text.
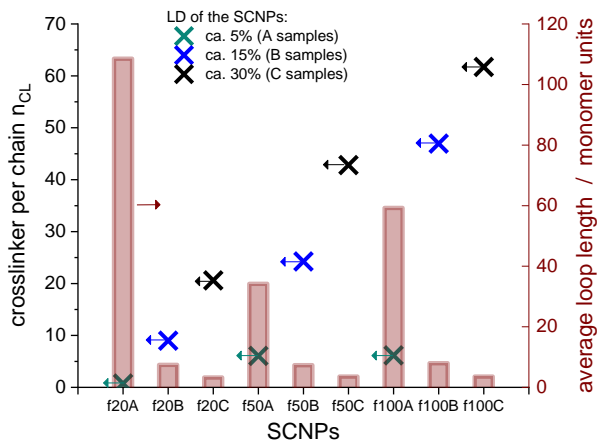
SI figure 30. The DP and the average number of crosslinker per SCNP (colored crosses, corresponding to the left axis) in hand, an average loop length (red bars related to the right axis in the corresponding colour) can be estimated for statistic copolymerized SCNPs.

.

3.5.5. Structures of the SCNPs
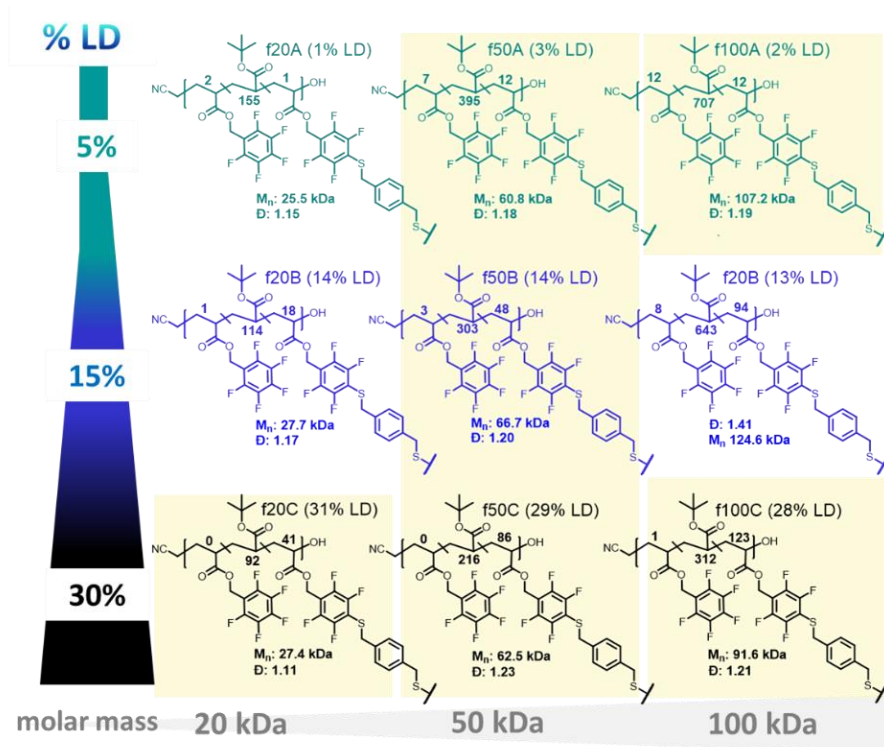
SI figure 31. Molecular structures of the SCNP library, synthesized via folding of poly(^{t}BuA-stat-PFBA) precursors by PFTR with the external dithiol crosslinker BDMT. The letter "f" for folding indicates the turn of the precursors to SCNPs. The samples are sorted column-wise according to the approximate molar masses (indicated by the number of the sample); whereas the ligation densities (LD) are sorted row-wise (indicated by the letter of the sample's name). The turnover of the ligation reaction of the penta-fluorinated functional groups was approximately quantitative for the higher decorated precursors (B, C), leaving only few PFB groups unreacted. In contrast, only ca. 50-60% PFTR turnover was observed for the low decorated A-samples, as discussed in the main text.

4. SEC-D4: Set-up and Characterization of the Polymer Library

4.1. SEC-D4 Set-up

The set-up of the SEC-D4 consists of the SEC column and four coupled detectors (SI Figure 32). After subsequent injection of the sample to the inlet system (SI Figure 32, left), separation of the polymers in the SEC-column leads to retarded elution of the more compact SCNPs compared to the corresponding linear precursor. Subsequently, the ideally monodisperse slices of separated polymers pass the MALS detector, which integrates the QELS detector at the nominal angle of 144.5° relative to the incident laser beam. Then, the sample passes the online viscometry and finally the dRI detector.
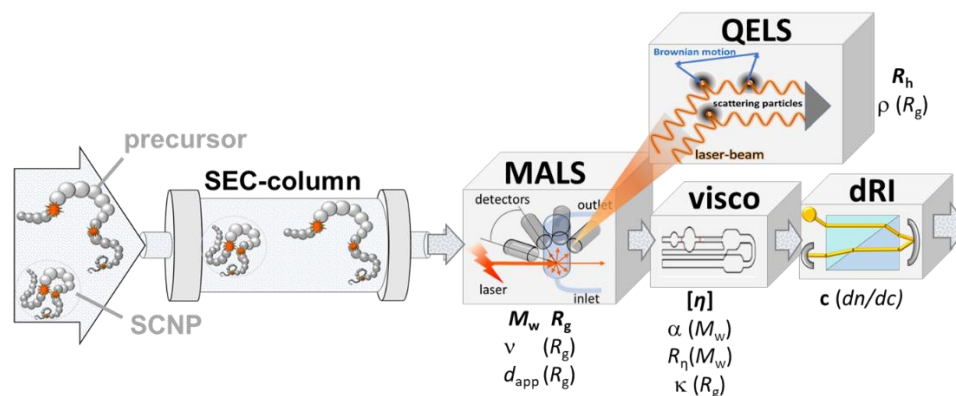

SI Figure 32. Scheme of the SEC-D4 set-up, consisting of the SEC column and four coupled detectors. Important measures are assigned next to the detectors.
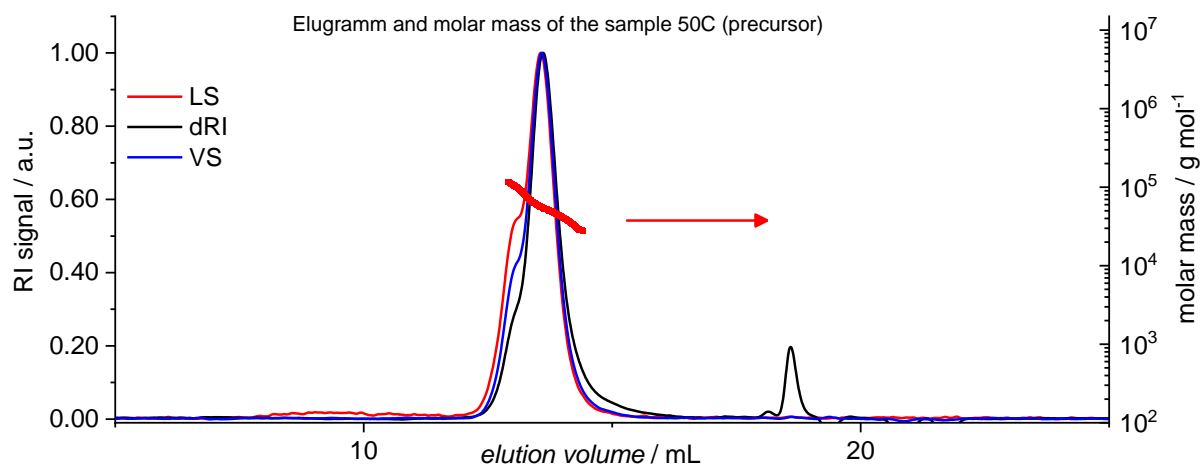
4.2. SEC-D4 Chromatograms

4.2.1. SEC-D4 chromatograms of the Precursor Library

The following figures show the MALS signal (light scattering or LS, red), the dRI signal (black), and the viscosity signal (blue) of the SEC-D4 characterization of the RAFT precursor polymers. The molar mass is represented in red dots (referring to the right y-axis), the average molecular weights can be found in the SI Table 8. After RAFT end group removal, the polymers serve as starting material for SCNP synthesis. SEC chromatograms after RAFT group removal show no significant change. Minor high molar mass shoulders in the LS signal are discussed in the main text. Small molecular side products from synthesis, indicated in the dRI peak after 30 mL elution volume, are well separated from the polymer material.
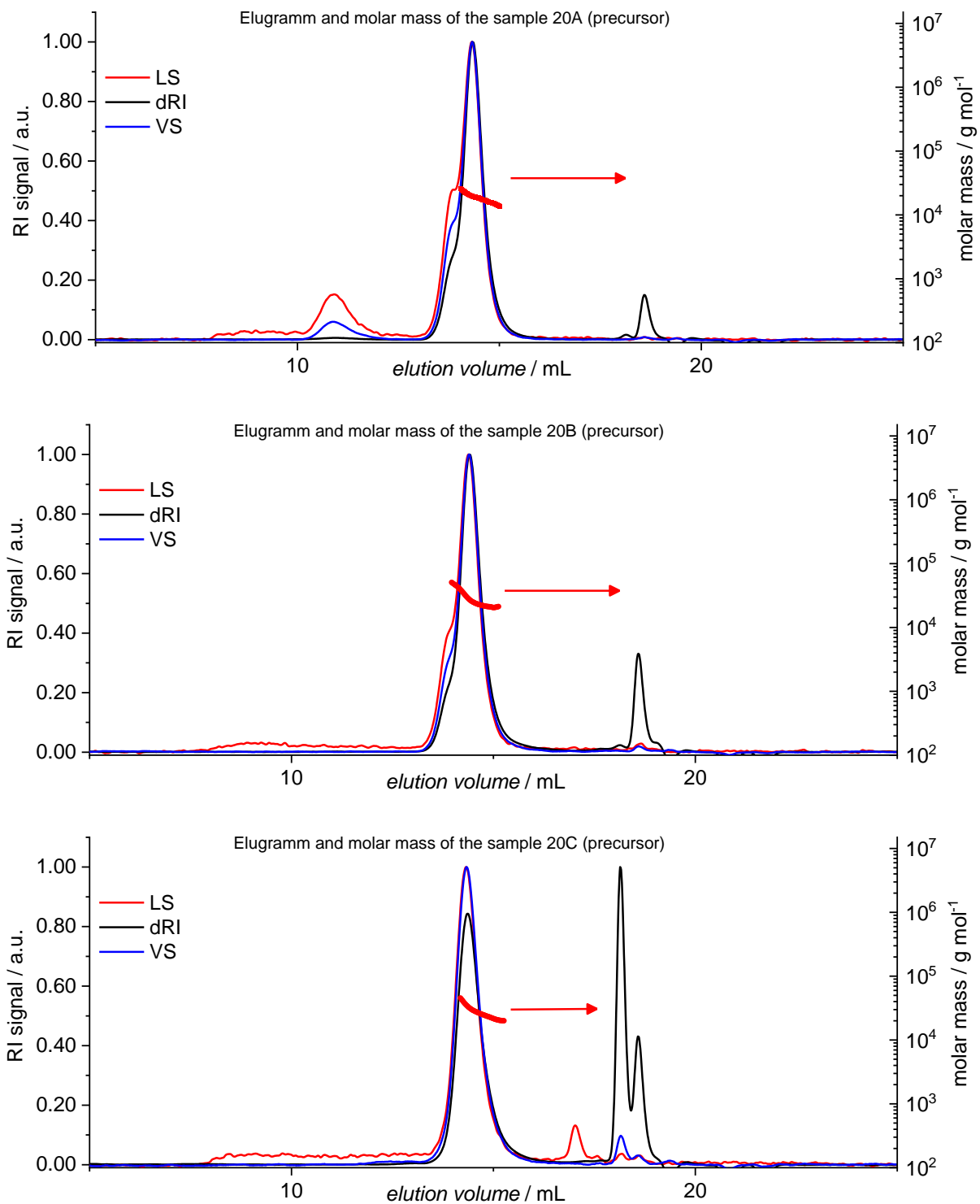
SI Figure 33. SEC-D4 chromatograms of precursor 20A, 20B and 20C in THF after RAFT synthesis.
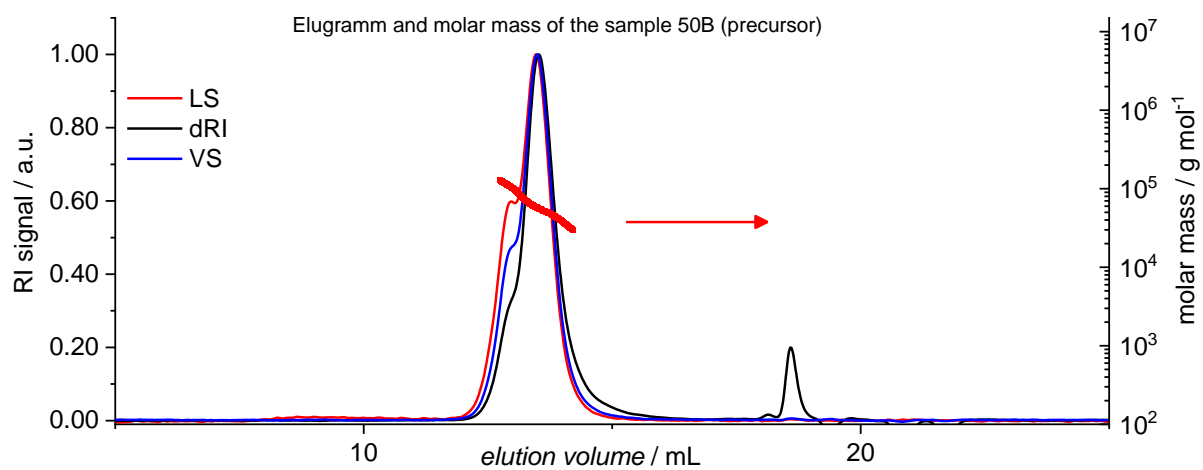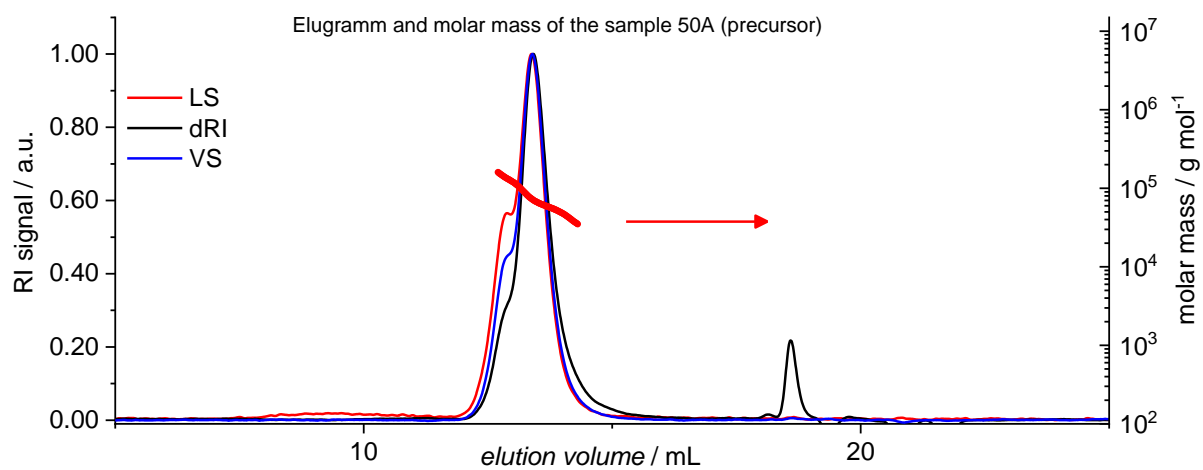
SI Figure 34. SEC-D4 chromatograms of precursor 50A, 50B and 50C in THF after RAFT synthesis.
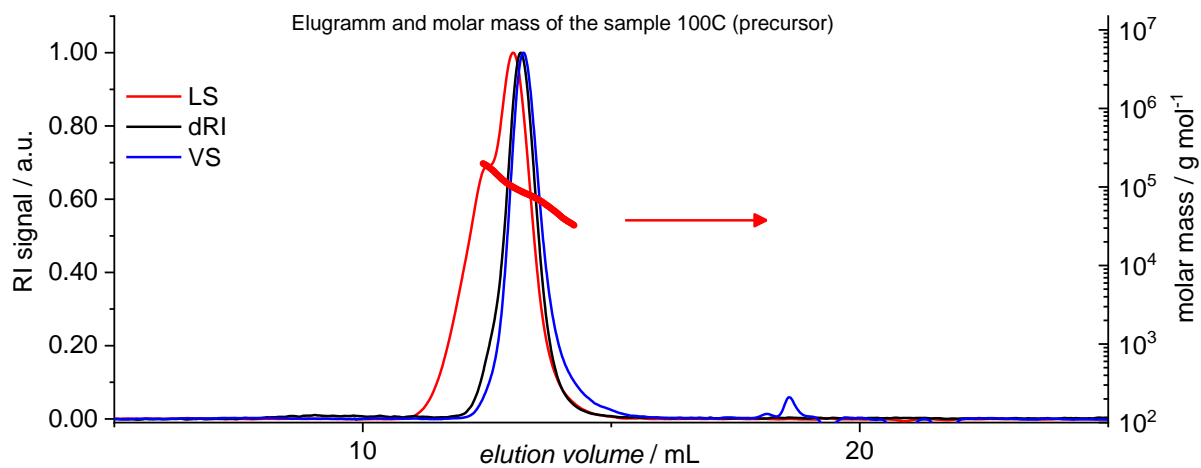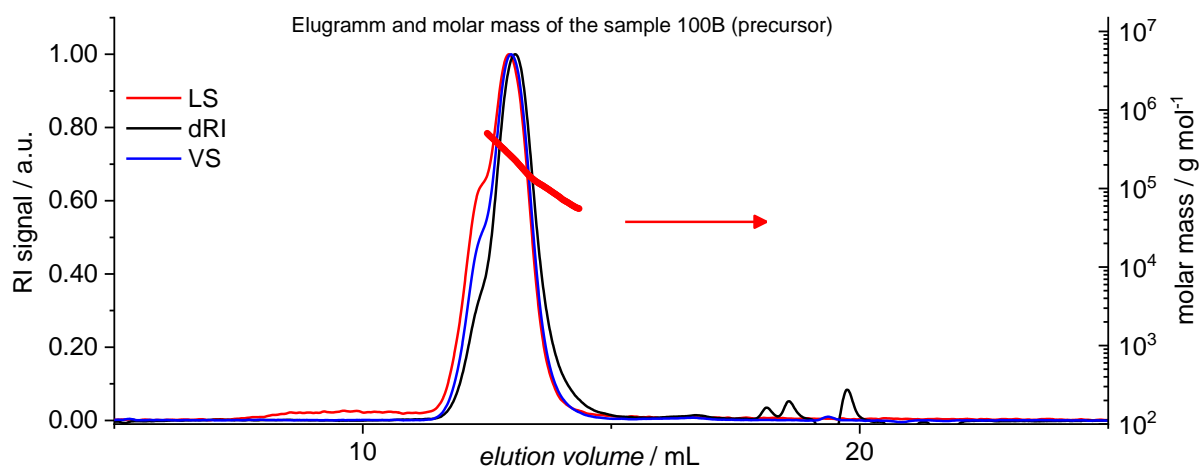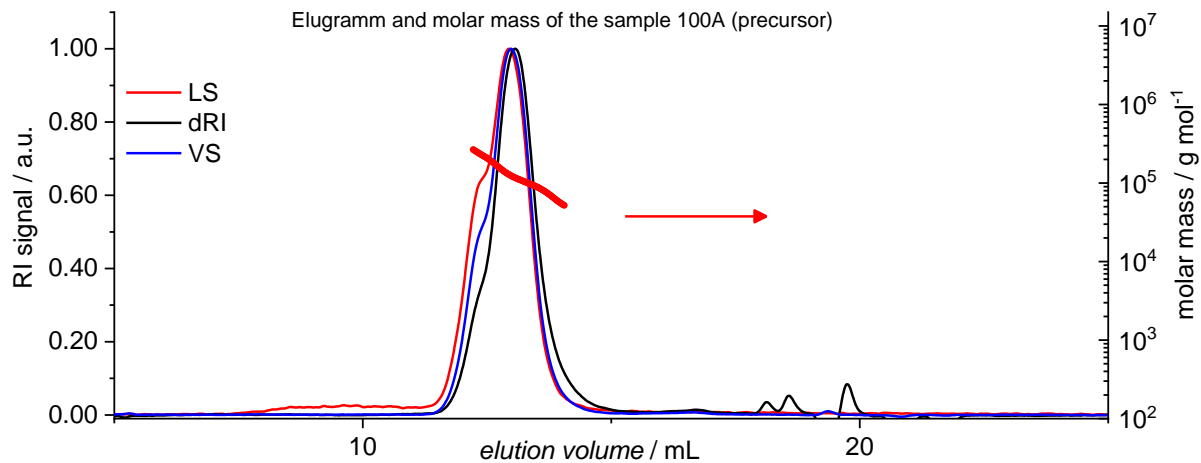
SI Figure 35. SEC-D4 chromatograms of precursor 100A, 100B and 100C in THF after RAFT synthesis.

4.2.2. SEC-D4 Chromatograms of the Single Chain Collapse

The following figures show all detector signals of the SEC-D4 traces of the complete library of molar masses 20kDa (SI Figure 46), 50kDa (SI Figure 37), and 100kDa (SI Figure 38).
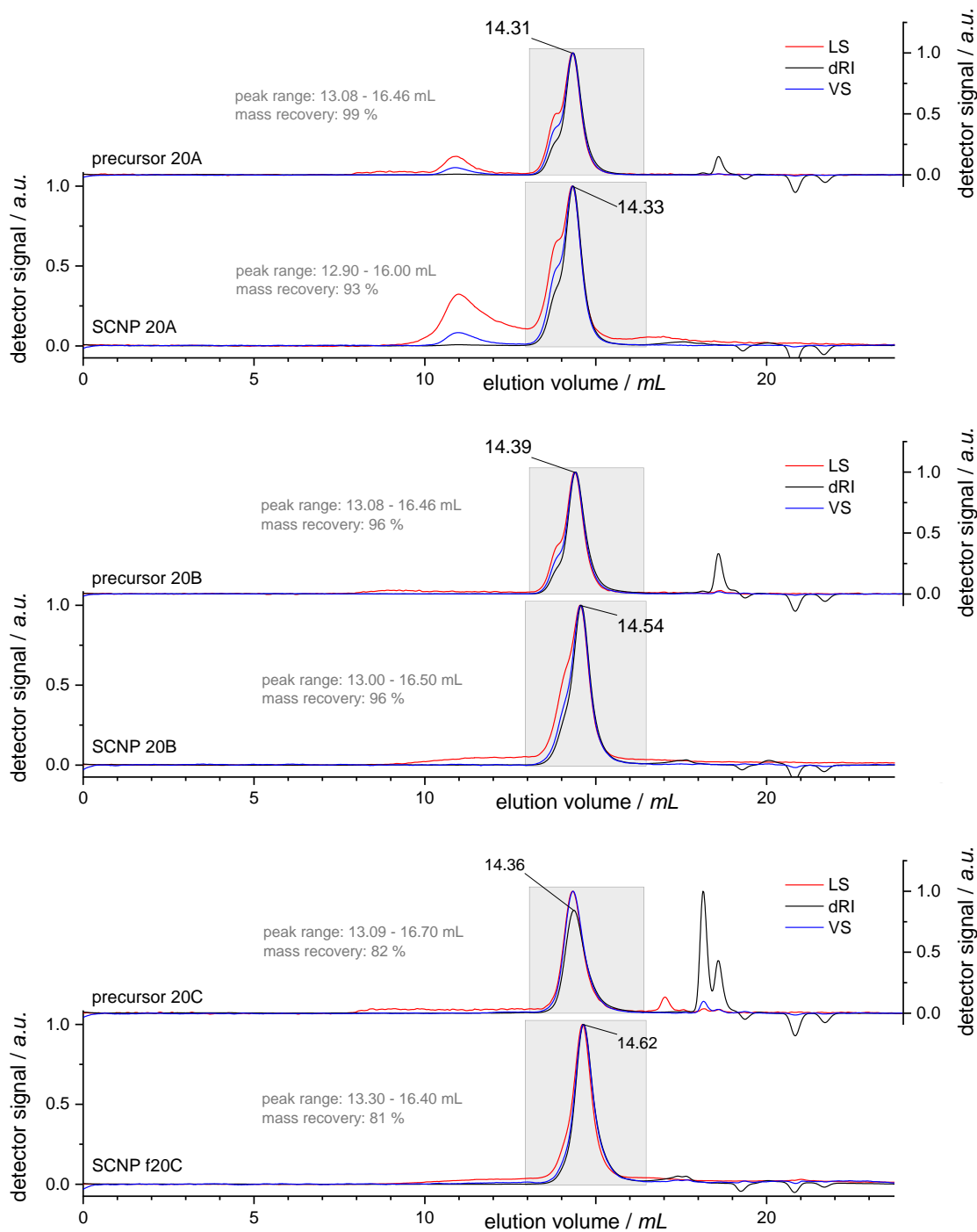
SI Figure 36. SEC-D4 traces of the 20kDa samples (20A, 20B, 20C) show the apparent hydrodynamic chain collapse due to the shift of the assigned apex of the dRI peaks for the SCNP (bottom) in comparison to the precursor (top).
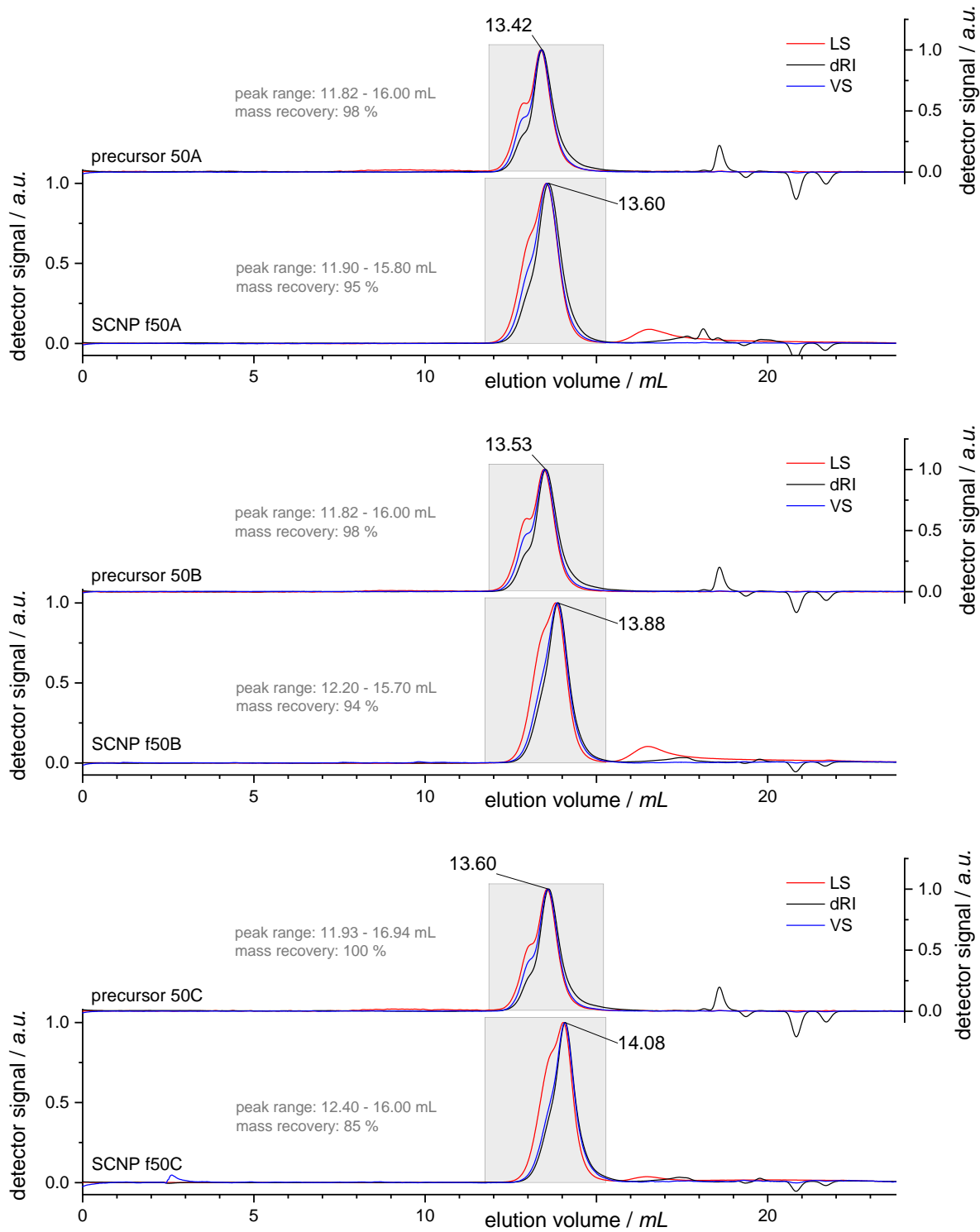
SI Figure 37. SEC-D4 traces of the 50kDa samples (50A, 50B, 50C) show the apparent hydrodynamic chain collapse due to the shift of the assigned apex of the dRI peaks for the SCNP (bottom) in comparison to the precursor (top).
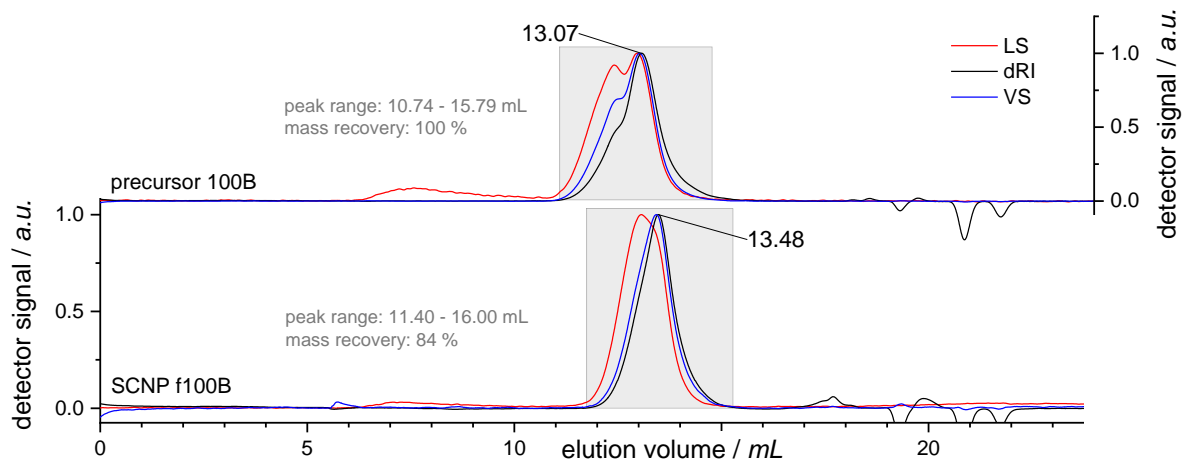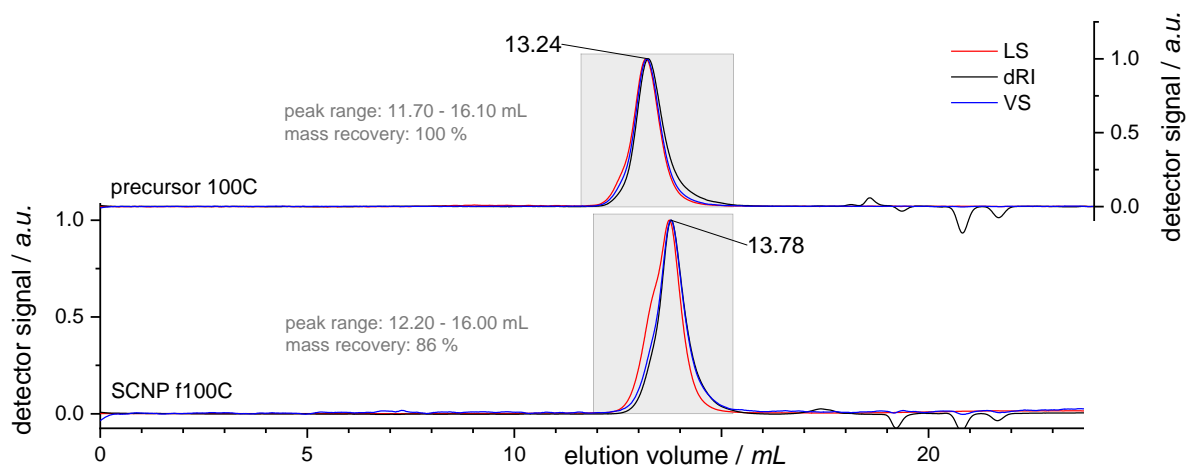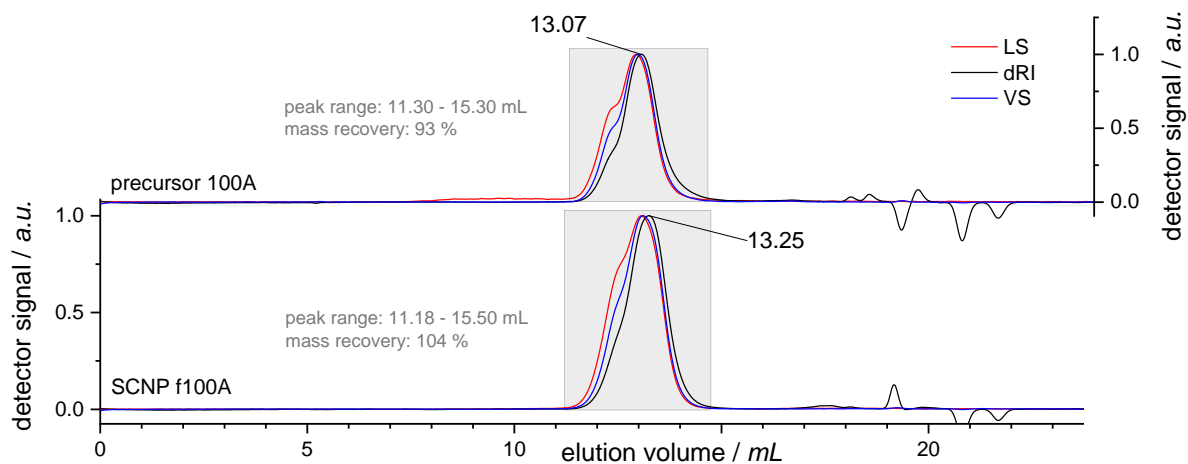
SI Figure 38. SEC-D4 traces of the 100kDa samples (100A, 100B, 100C) show the apparent hydrodynamic chain collapse due to the shift of the assigned apex of the dRI peaks for the SCNP (bottom) in comparison to the precursor (top).

4.3. Online SEC Results and further Graphs of the SEC-D4 Analysis

4.3.1. Online Molar Mass and Viscosity

The online data of the most meaningful SEC-D4 analysis (SI Figure 39 - SI Figure 40) allow to monitor the characteristic trends of the transformation from the precursor material (dotted dRI line or open dots of molar mass,- or viscosity data, respectively) to their folded analogues (full dRI line or full dots of molar mass,- or viscosity data, respectively) for all library copolymers. The dRI signals (lines corresponding to the left axis) are shown next to the results of online measures of absolute molar mass and intrinsic viscometry [η] (dots corresponding to the right axes). For sake of visual clarity, the data points are reduced to the half and the data is plotted at the same range of elution volume for all samples. The dRI-shift of the SCNPs towards higher elution volumes respective the starting material (see assigned apex of the dRI peaks) due to apparent hydrodynamic compaction, a decrease of intrinsic viscosity [η] due to compaction after folding and an increase of the molar mass due to crosslinker incorporation. These trends confirm the SCNP synthesis.
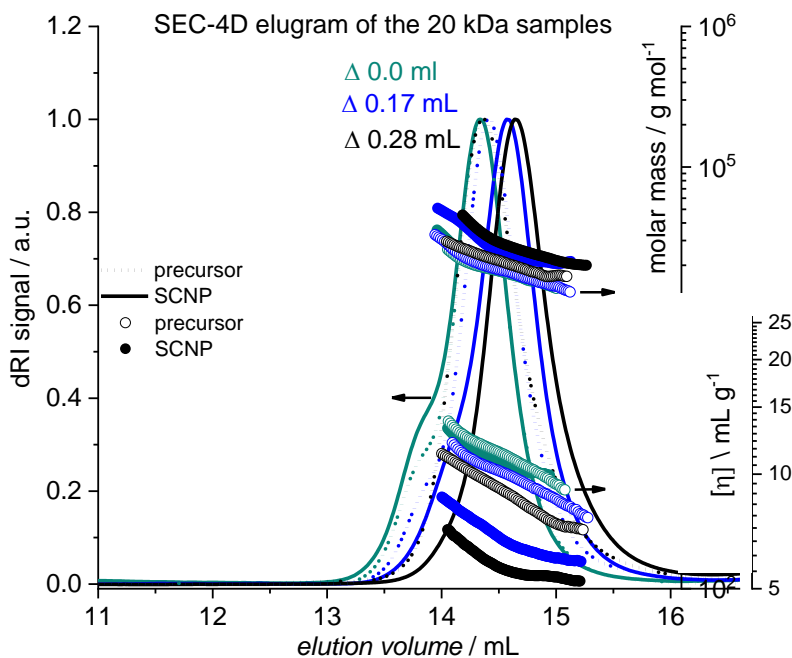
SI Figure 39. Results of SEC-D4 characterization, monitoring the most important detector traces, confirming the folding from linear precursor (open dots and dotted dRI line) to their pairing SCNPs (full dots and full dRI line) for the samples of approximately 20 kDa. The signals show the dRI-shift (left y-axis)of the towards higher elution volumes (Δ mL values), an increase of the molar mass due to crosslinker incorporation (top right y-axis) and a decrease of intrinsic viscosity [η] (bottom right y-axis).
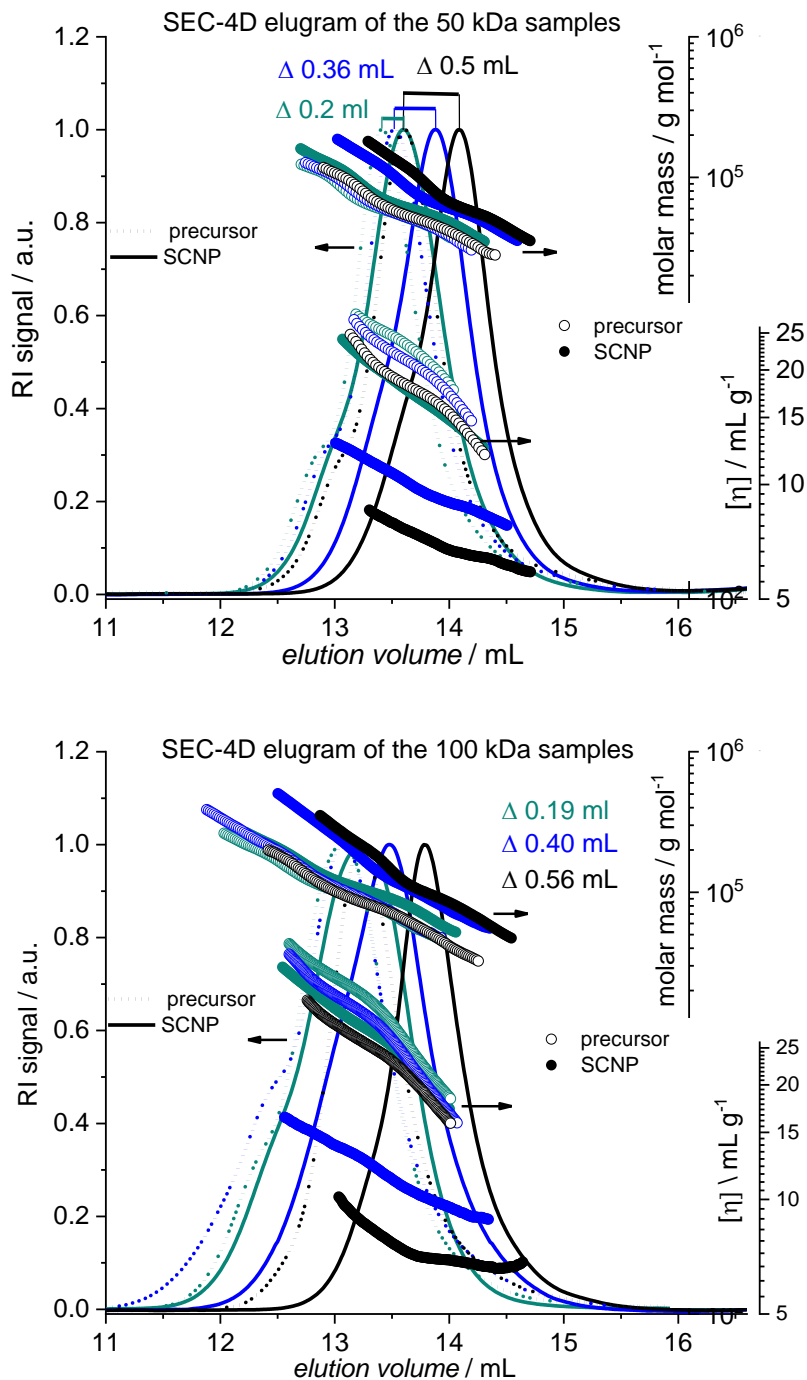
SI Figure 40. Results of SEC-D4 characterization, monitoring the most important detector traces, confirming the folding from linear precursor (open dots and dotted dRI line) to their pairing SCNPs (full dots and full dRI line) for the samples of approximately 50 kDa (top figure) and 100 kDa (figure below). The signals show the dRI-shift (left y-axis)of the towards higher elution volumes (Δ mL values), an increase of the molar mass due to crosslinker incorporation (top right y-axis) and a decrease of intrinsic viscosity [η] (bottom right y-axis).

4.3.1. The Online Contraction Factor

Online contraction factors g' (viscosity model, Astra® software) are given in SI Figure 41 in dependency of the molar mass for all SCNP samples.
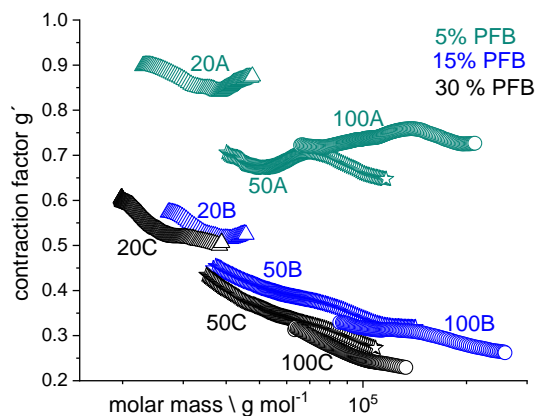
SI Figure 41. Online contraction factors of the SCNPs of low LD (green), middle LD (blue) and high LD (black) obtained from SEC-D4 characterization in molar mass dependency. The different molar mass groups are indicated by the shape of the dots (triangle: 20 kDa, star: 50 kDa, dots: 100 kDa).

4.3.2. The ρ- Parameter R_g (SANS) /R_h (online SEC)

The mass-centred compactness is discussed by the κ−parameter (R_g/R_η) in the main text. Accordingly, the complementary ρ-parameter is calculated by the ratio of the online R_h from SEC-D4 analysis and R_g from SANS technique. Even if the fit of the correlation function of the online QELS data from SEC-D4 analysis was not optimal or the R_h showed relatively high error (see SI Table 9), the reproducibility of the R_h of single measurement was high for the SCNP samples. The ρ-parameter shows the expected opposing trend to κ−parameter of the data obtained for the SCNP samples in SI Figure 42. The agreement of both parameters shows the similarity of the hydrodynamic measured of size R_η and R_h, and further confirms the topology of the polymers as discussed in the main text.
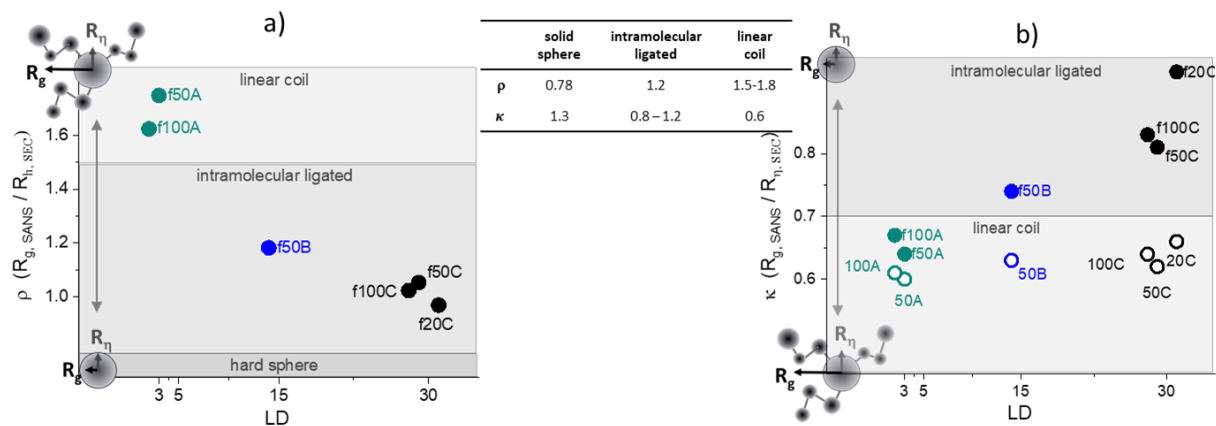
SI Figure 42. The ρ-parameter gives an insight into the topology of the polymer SCNPs (a). The ρ-parameter is calculated for the R_g (from SANS) and online R_h (from SEC-D4, QELS). As reliable online R_h were obtained for the SCNPs(full dots) only, we included the graph b for the direct comparison of the ρ-parameter to the complementary κ–parameter.

5. The Second Virial Coefficient A₂ under Folding Conditions

The solvent conditions during SANS and MALS characterization deviate from those during the folding reaction, as both have been performed in the good solvent THF only. The employed solvent mixture for folding is approximately ACN/THF = 4/1, depending in the polymer features as described in the main text. Additional determination of the second virial coefficient are performed to investigate the thermodynamic state during the folding reaction. Determination of A_2 in batch was performed by manual injection of precursor samples to a MALS detector, dissolved in a solvent composition as employed for SCNP synthesis. The A_2 determination was performed under dilute conditions (2 to 15 mg/mL), as only polymer solutions below the overlap concentration c^* (see SI Table 10), behave according the scaling behavior and power expansion of the osmotic compressibility. The results of exemplary experiments for the 50 kDa samples serve to review the solvent conditions of the precursor under the applied folding conditions (SI Table 4) indicating conformation close to the *theta*-state.

SI Table 4.Second virial coefficients of the precursor for solvent mixture employed for folding conditions, exemplarily determined for the of the middle molar mass (50 kDA samples).

sample	50A	50B	50C
A_2 [mol mL/g²]	$1.44E^{-05}$	$2.82E^{-05}$	$3.24E^{-05}$

6. SANS: Set-up and Characterization of the Polymer Library

6.1. SANS – Instrumentation and Data Processing

The set-up of the employed SANS-device D11 at the Institute Laue-Langevin (ILL, Grenoble) is shown in the SI figure 43. The employed sample-detector distance, the scattering intensity, and the scattering angle directly impacts the obtained scattering curves P(q).[16] The size-resolution of the analyte depends on the employed wavelength and the scattering angle or q-range, respectively. Detector distances of 1- 8-, and 20 m (right of figure SI figure 43, top) are employed for the polymer samples. Herein, a broad q-range is achieved, leading to broad range of resolved size scales for the investigated polymer samples, ranging from monomer to macromolecular dimension.
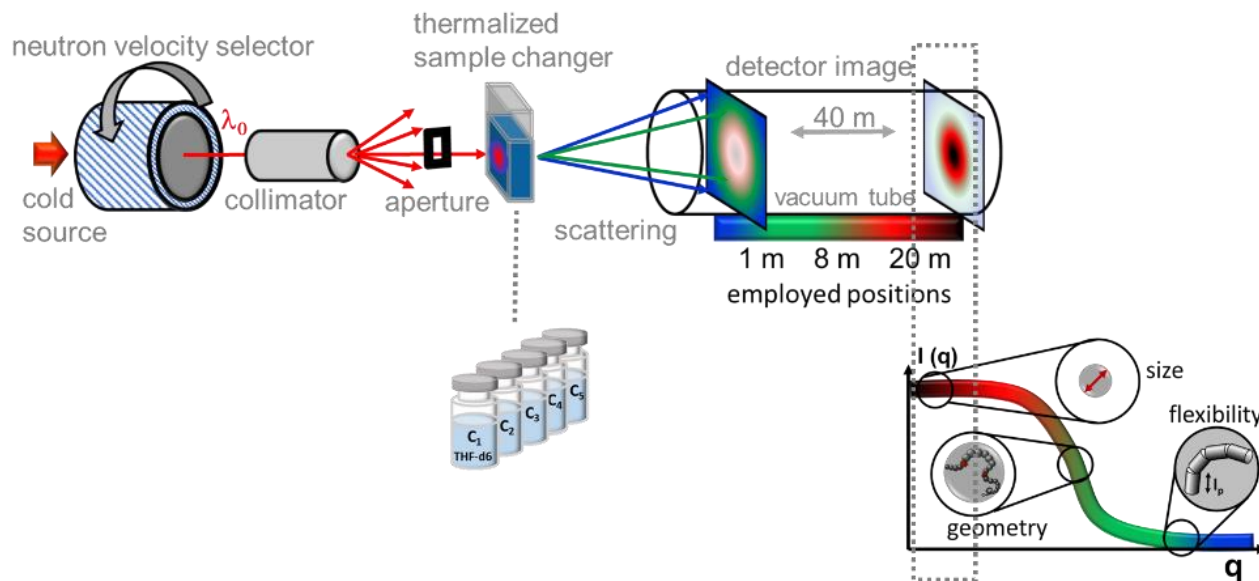
SI figure 43. Scheme of the SANS-instrument D11 of the Institute Laue-Langevin (ILL, Grenoble), which was employed for the characterization of six precursors and their corresponding SCNPs in solution (THF-d$_8$). Every sample was characterized for five different concentrations in the dilute solution regime, enabling a total Zimm data analysis.

The concentrations of the samples are held sufficiently below chain overlap concentration c*, no interparticle interaction is assumed. The absence of a structure factor peak in the scattering curve justifies this assumption of no interparticle interaction during SANS characterization. Herein, the form factor P(q) is equal to the scattering function of a single isolated polymer particle, revealing size and shape of the precursors and the corresponding SCNPs.[17]

6.1. Evaluation of P(q)

The evaluation of the form factor $P(q)$ gives information about size and the shape from the scattering behavior of a single isolated particle. In contrast to the simultaneously performed extrapolation to the scattering angle q = 0 and the concentration c = 0 in the so called Zimm diagram, we performed this extrapolation separately in two steps.[18,19] The key benefit of this procedure is facilitated by the dimensionless display of all parameters. This is achieved due to use of the ordinate values at c, q = 0 and their subsequent extrapolation to c = 0. Herein, the contrast factor is reduced, and the molecular weight is not required for the calculation.

The procedure is exemplarily shown for the precursor sample 50A in the SI Figure 44. SI Figure 44 shows the raw scattering curves after subtraction of the coherent underground (*I*). First, each scattering curve is corrected to the scattering intensity of the Guinier plateau ($I_{q=0}$ or for simplicity: I_0). I_0 is determined by extrapolation of a sigmoidal fit of each scattering curve. The normalization to the Guinier plateau allows to obtain I_{norm}, elsewhere known as apparent form factors $P_{app}(q, c)$, visualized in graph B of SI Figure 44. The apparent form factor $P_{app}(q, c)$ describes the angle dependency at finite concentration. As the intensity I_0 is a product of a constant K_{SANS} (including the

contrast $\Delta\rho^2$), the concentration (c) and the weight average molar mass (M_w), extrapolation to infinite dilution allows for a first estimation of the molar mass of the particles (equation SI-11).

$$I_0\,(q)\,\approx M_w * c * K_{SANS} \tag{SI-11}$$

Subsequently, the scattering behavior is corrected to the behavior at c = 0 by extrapolation of $P_{app}(q, c)$ to infinite dilution (graph C of SI Figure 44). This allows to obtain the corrected apparent $P_{c=0}(q)$. Finally, the average of all $P_{c=0}(q)$ curves is calculated (graph D of SI Figure 44) to obtain the true form factor $P_{c,\theta=0}(q)$, coined $P(q)$ for simplicity.
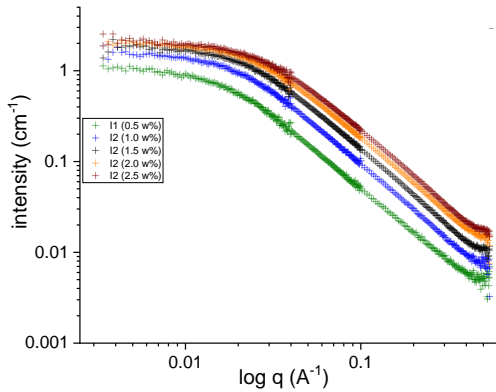
graph A   graph B
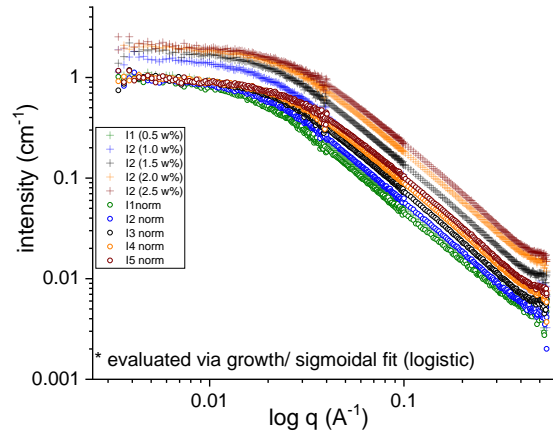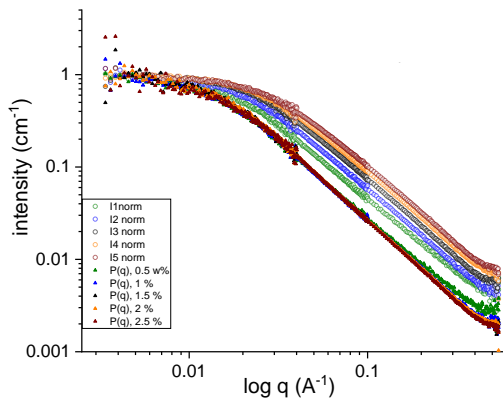
graph C   graph D
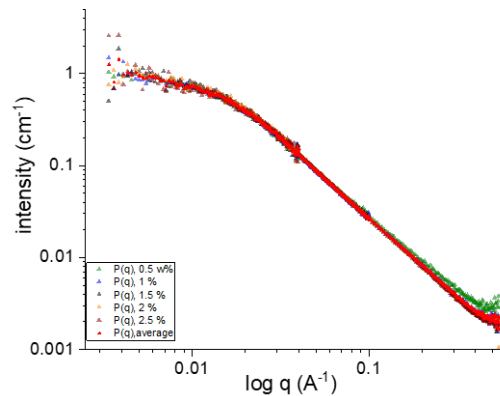
SI Figure 44. Procedure of the evaluation of P(q) for each sample, which facilitates to obtain a true form factor P(q) (red curve, graph D). Graph A: Raw scattering intensities after subtraction of the incoherent background scattering (I) of the precursor sample 50A (star symbols, five different concentrations, indicated by different colors). Graph B: Correction of the raw scattering curves (stars) to the I_0 corrected scattering curves (open dots) for each sample concentration. Graph C: Representation of the q,- and c-dependencies of the corrected apparent form factors $P_{c=0}(q)$ (full dots) derived from the apparent form factors P_{app} (q, c) (open dots). Graph D: The true form factor P (q) (red) is obtained as the average curve of the five P_{app} (q, c) curves.

The combined steps for processing the true P(q) as described in SI Figure 44 (according graph A (crosses), graph B (open dots), graph C (full dots) and graph D (red full dots of the finally obtained P(q))) are shown for the samples 50A and the corresponding sample f20C in the SI Figure 45. Each sample shows the concentration dependency by the height of the Guinier plateau I_0 of the raw scattering curves (I) after subtraction of the incoherent underground

(crosses) according equation SI-11. Slight increase at very low q values show the existence of large particles, presumably as a result of intermolecular crosslinking, resulting in multiple-chain nanoparticle (MCNP). The presence of MCNP was only slightly indicated by the intensity of the SEC-MALS detector signal at low elution volumes (see chapter 4.2). The change of the conformation from precursor (SI Figure 45, left) to SCNPs (SI Figure 45, right) can be clearly seen by the comparison of the slopes of the final P(q) scattering curves (red dots).
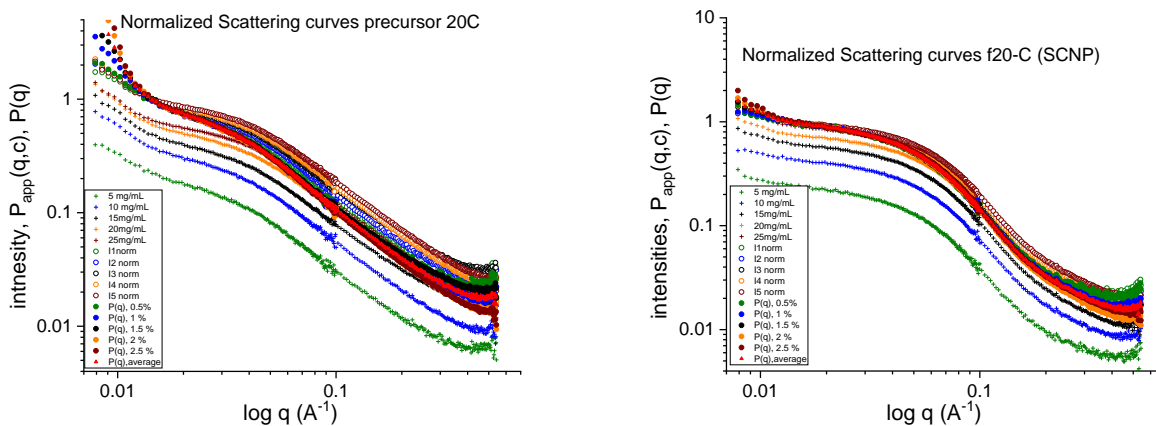
SI Figure 45. Merged curves obtained along the process of the calculation of true form factor (P(q), red full dots) from the raw scattering curves after subtraction of the incoherent underground (I, cross symbols), showing the effect of concentration (high of the raw curves), slight aggregation (increased in very low q-range for all concentrations) and change of conformation due to comparison P(q) of the precursor (left) and the SCNP (right).

All true *P*(q) scattering curves for the SANS-characterized samples, evaluated according the procedure as described in SI Figure 44, are given in SI Figure 46. The slope of the scattering curves (related to the scaling factor ν) drops clearly in correlation of the extend of intrachain collapse achieved by SCNP synthesis. The higher the LD of the SCNPs, the steeper is the negative slope of the obtained P(q) scattering curves (A-samples < B-samples < C-samples):
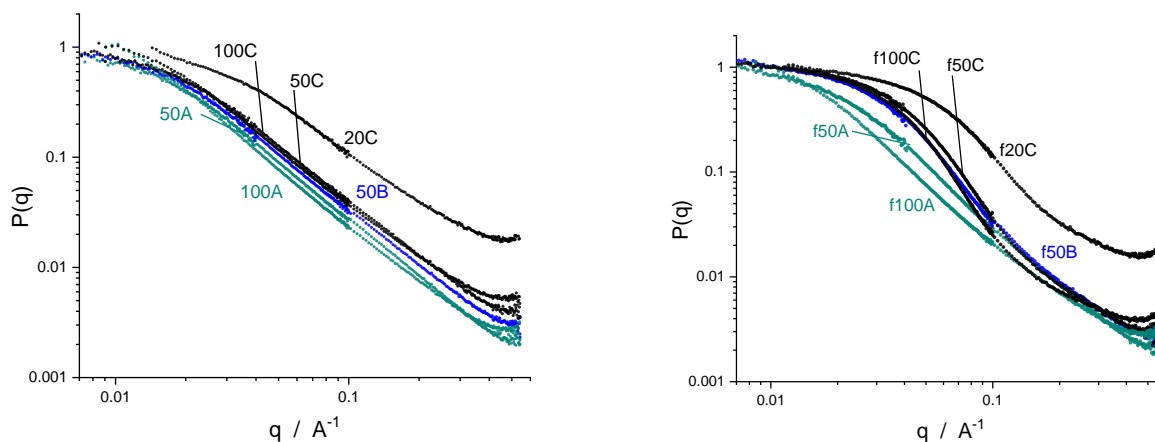
SI Figure 46. Obtained true P(q) scattering curves in the colors of the color code for all precursor (left) and all SCNPs (right) characterized via SANS technique.

6.1. Manual Plotting Form Factor P(q)

Conventional plots of the scattering intensity $P(q)$ are named after the pioneers of small-angle scattering like Zimm, Guinier, Kratky and Casassa suitable for describing a distinct q-range.[20–22] SI Figure 47 shows the certain ranges of a scattering curve, which allow to deduce characteristic information by conventional plotting. Zimm formalism assesses the critical parameters second virial coefficient A_2 and the absolute R_g and M_w, shown above. Guinier plots can be used for the evaluation of the R_g, Kratky plots can qualitatively assess the degree of folding, while Casassa plots are rather suitable for determination of the flexibility of linear chains.
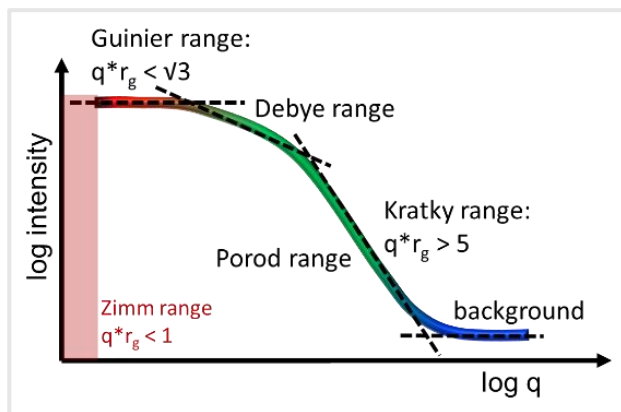
SI Figure 47. Scheme of a scattering curve obtained from SANS experiments. Certain ranges of a scattering curve allow to deduce characteristic information by conventional plotting within these ranges.
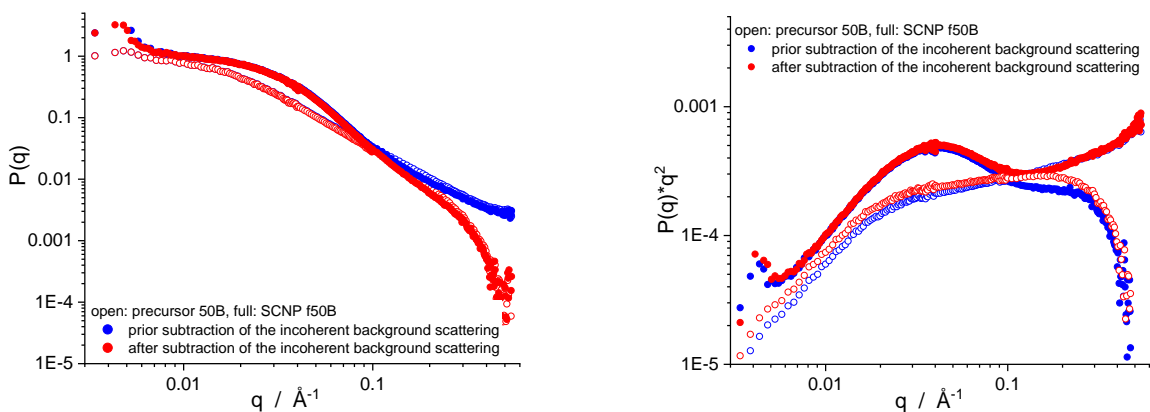
SI Figure 48. The impact of the subtraction of the incoherent background scattering in conventional dimension (left) or in the dimension used for Kratky plots (right), exemplary shown for the scattering curve of the precursor 50B (open dots) and its corresponding SCNP f50B (full dots). The curves prior the baseline subtraction (blue) differ from the curves after baseline subtraction (red) for high q-ranges.

For sake of accuracy any plotting was performed with the form factor P(q), corrected for angle and concentration dependencies, instead of the direct use of c-dependent scattering curves.

Plotting must be applied to the normalized neutron scattering curves after subtracting the incoherent background scattering. The subtraction of the incoherent background scattering has often been neglected in the past, which we aim to correct in this work. The subtraction of the incoherent background is applied to the final P(q) curve of each sample. More precise, the incoherent background is determined by the data points of very large q values (q > 0.47) of P(q), as it does not inhere phase-information of the analyte. The average value from the last 15 data points of high q-values is subtracted from the whole scattering curve. The subtraction of the incoherent background scattering

has an impact on the shape of the scattering curve for very high q-ranges only (SI Figure 48, left). Even if the shape of the scattering curve is changed for high q-values, main interpretation of conventional plots remains unchanged. Manual plots presented in this work focus generally on the scattering information of lower q-values, as exemplarily shown for the plot in the dimensions of Kratky plots (SI Figure 48, right).

6.1.1. Zimm Analysis

Zimm analysis is a mathematical series development of the scattering intensity as a function of the scattering vector q and concentration, as described in the equations above (SI-2 to SI-4). If the contrast factor is known, the weight average of the true molecular weight is obtained after extrapolation to the scattering angle q = 0 and concentration c = 0. Zimm proposed to carry out this extrapolation together in a special diagram, coined Zimm plot.

Assuming no particle interaction, Zimm analysis is conventionally performed to the second series only, and higher terms are neglected.[17] We show the classical Zimm analysis exemplary for the precursor 50C and its folded counterpart f50C in SI Figure 49. The determination of the absolute R_g is depicted in the inserted concentration dependent graph of the SI Figure 49 (small figure to the top). The determination of the second virial coefficient is shown in the framed zoom to the right of SI Figure 49.
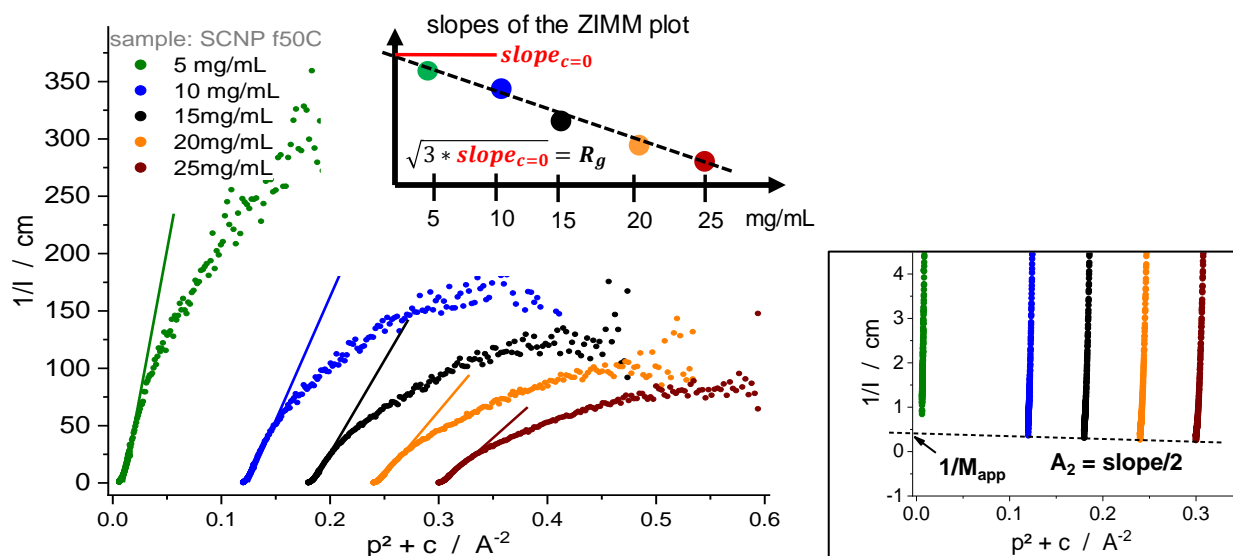
SI Figure 49 Determination of R_g (left) and the A_2 by the linear fit of the scattering curves at very low q-ranges. The slopes of the linear fits are plotted versus the concentration to derive the R_g (see inserted graph at the top). The framed zoom to the left shows how A_2 and the apparent molar mass M_{app} are deduced.

The choice of employed q-ranges for the linear fit of the scattering curve for R_g calculation is important for reliable data analysis. This importance becomes clearer for the logarithmic plot of the scattering curves (SI Figure 49, left), as this kind of plot enables the R_g calculation. To assure comparability of the Zimm analysis between the results of the precursor and the corresponding SCNP, exactly the same low q-ranges were employed for the evaluation of the characteristic slopes of the scattering curves (here: below q = 0.003). The Zimm-plots of the precursor 50C is shown together with the Zimm-plot of SCNP f50C in the figure below to show this consideration. The choice of the data points for the linear fit poses an optimization problem, because on one hand the precision of the linearization increased for infinite small p-ranges. On the other hand, enough data points must be employed for a reliable fit. The choice of the data point for the linearization was therefore optimized and applied for both the precursor and the corresponding SCNP.
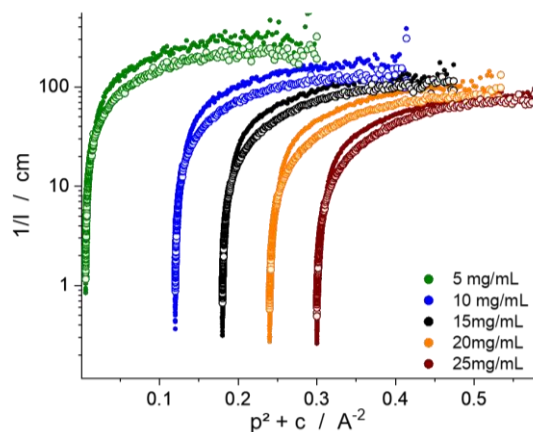
SI Figure 50. Zimm plot of the scattering data of the precursor 50C (open dots) and the corresponding SCNP f50 (full dots). The logarithmic plot facilitates for the precise linear fitting of the very low q-ranges. The selection of the data points of the very low q- range is important to achieve comparability of pairing samples.

SI Figure 51 shows the results for R_g(c) for all precursor samples (open dots) and all SCNPs (full dots), the colors of the data point indicate the %PFB of the samples. For sake of visual clarity, R_g(c) of the 50 kDa samples are given in the left graph of SI Figure 51, whereas the R_g(c) of the samples 100A-, 100C-, and 20C is given in the right graph of SI Figure 51. The data points obtained for the different concentration of one sample are connected *via* a dotted line as guide for the eye.
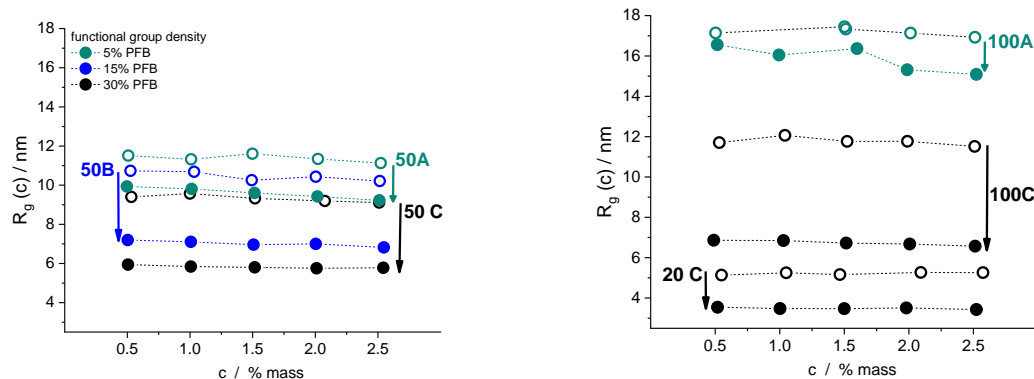
SI Figure 51. Concentration dependent plot of the radii of gyration obtained by Zimm analysis of the SANS data. The results of the samples of approximately 50 kDa are given in the left plot, whereas the data of the 20-, and 100 kDa samples are given in the right plot. Extrapolation to c=0 allows for calculation of the R_g as dicsussed in the main text.

All samples show the expected trend of increasing R_g(c) with decreasing concentration. This underlines the importance of extrapolation of the radii to infinite dilution to take in account concentration effects. The average R_g for each sample (see SI Table 10) is obtained by extrapolation of the R_g to infinite dilution for each sample.

6.1.2. Kratky Plots

Experimental Kratky plots of the dimension $q^2P(q)$ vs. q for all samples characterized *via* SANS are represented in SI Figure 52, spanning the complete measured q-range. The plateau height is (amongst other factors) caused by the different particle sizes or molar mass, respectively. A plateau in a Kratky plot is obtained for all precursor (SI Figure 52, left), resembling a Gaussian coil conformation (q^{-2} - slope). The Kratky plots of the SCNP (SI Figure 52, left) indicate increased segment density to the extent of functional group decoration (%LD, see color code). In contrast to the less crosslinked SCNPs (A-samples, green) the tightly crosslinked SCNPs (B samples [blue] and C samples [black]) show a bell-shaped peak, indicating increased segment density. The position of the apex of this peak (q-dimension, see colored labels q_A, q_B, q_C) is directly related to the size of the mass-fractals and fully resembles to the trends observed for R_g of the SCNPs (SI Table 9-10). Contrary to the expected Kratky plots of spheres, a high-

q plateau is still present for the compact B- and C-samples of the SCNPs. This observation indicates the coexistence composed of dense-fractions and linear chain conformation as discussed in the main text. Dimensionless Kratky plots ((qR_g)^{2}P(q) vs. qR_g), allow to elucidate the sphericity of the polymers without mass,- or size effects, as exemplarily shown for the 50 kDa samples in SI Figure 53, and the increasing degree of intramolecular ligation of the SCNP samples from f50A to f50B to f50C is clearly visible by the extend of the bell shaped peak.
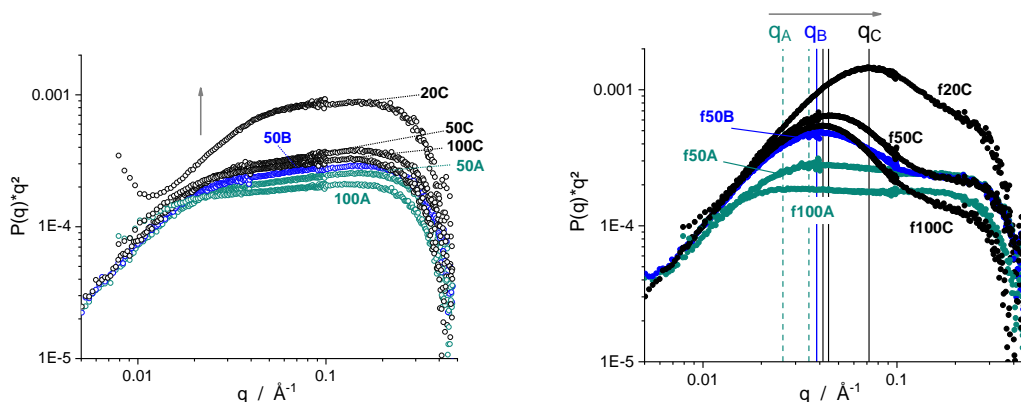
SI Figure 52. Overview of the Kratky plots of the precursor (left, open dots) and the SCNPs (right, full dots), spanning the whole measured q-range. The vertical arrow in the left graph indicates the increasing plateau hight due to mass-, or sizes effects. The horizontal arrow in the right figure highlights shift of the position of the apex of the bell-shaped peak (q-dimension, see colored labels q_A, q_B, q_C), which allows for an estimation of the size of the dense mass-fractals.
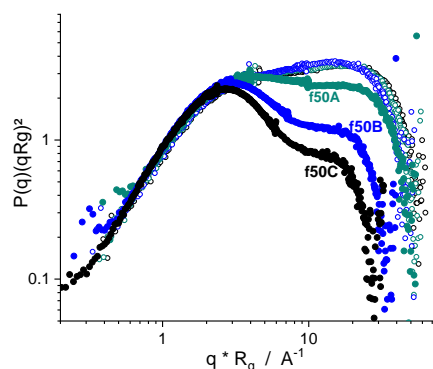
SI Figure 53. Dimensionless Kratky plots of the precursor (open dots) and the SCNPs (full dots), exemplary shown of the 50 kDa samples.

6.1.3. Casassa Plots

The transformation to Casassa plots can be used to estimate the transition from coil-like behavior (low q-range) to rod-like behavior (high q-range), if sufficient stiffness for such a transition is true for linear polymer chains. The intersection q^* (SI Figure 56) marks the transition from random coil to rigid rod behavior, therefore facilitating to derive the Kuhn length l_K of the rigid rods indirectly.[22] Attempts for determination of q* from Casassa plots were not successful for the precursor samples, presumably due to flexible chain properties or a lack of the coil to rod transition point, respectively. Herein, we assume high chain flexibility of the precursor chains under the good solvent conditions during SANS characterization, which coincides with the results of other thermodynamic measures like A_2.

The Casassa plots of the SCNPs show an asymptotic behavior for high q-ranges and the effect of the mass or size (SI Figure 54, left graphs) as discussed for the Kratky plots (chapter above). Similar to the observation from Kratky plots, a significant maximum at low q-ranges and an asymptotic behavior for high q-ranges, confirm the coexistence of dense-fractions and linear chain conformation as discussed for the Kratky plots (SI Figure 54, right graphs).
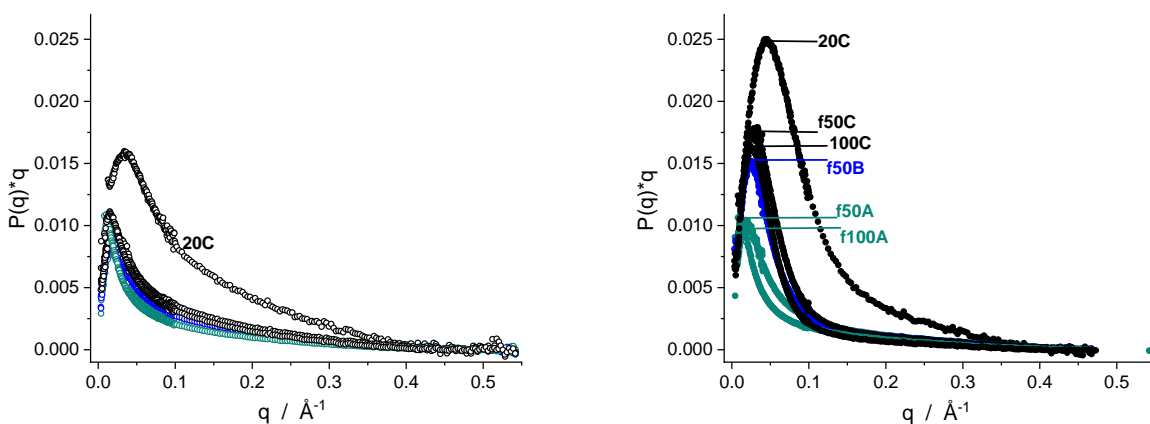
SI Figure 54. Overview of the Casassa plots of the precursor (left, open dots, labelling is resigned due to overlay) and the SCNPs (right, full dots), labeled with the sample names.

The Casassa plots assist to deduce information about dense fractions of the intramolecular ligated SCNPs, as the height of the maximum at low q-ranges increases with decreasing deformability of the SCNPs in the order A < B < C, as exemplarily shown for the 50 kDa samples in the SI Figure 55.
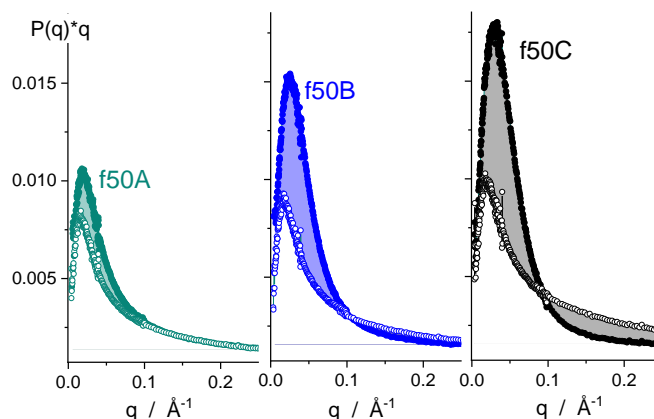
SI Figure 55. Casassa plots of the 50 kDa samples of the SCNPs (full dots) in contrast to the corresponding linear precursor (open dots).The colored area assist as guide for the eye for the increasing malleability with increasing LD (A < B < C).

The phenomena observed for the Kratky-, and Casassa plots are summarized in the illustration of SI Figure 56. The phenomena indicate the coexistence of both, dense-particle and gaussian chain behavior. We assume that not the entire SCNP molecule is compacted equally, as suggested in the cartoon to the right of SI Figure 56.[21]
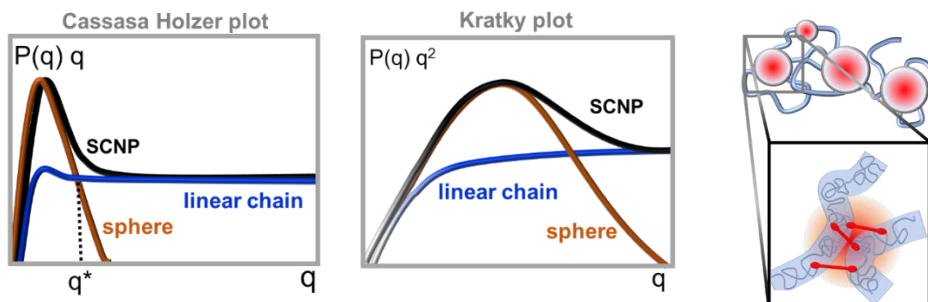
SI Figure 56. Schematic Kratky representation (left) and Casassa presentation (right) of tendencies found for linear chains or precursor (blue line) and SCNPs (black) and expected representation for hard spheres (brown). The dotted line in the Casassa plot marks the intersection point q*, which allows to estimate the stiffness if rigid chains are present.

6.2. Evaluation of the Scaling Factor from P(q)

SI Figure 57 and SI Figure 58 show the evaluation of the scaling factor ν from the double logarithmic plotted scattering curves P(q), derived of SANS experiments. The highest inverse slope equals the fractal dimension (d_{frac}), which is related to the scaling factor according equation SI-5. The linear fit was applied within the assigned range of the scattering curve P(q) in order to obtain high fit quality (at least $R^2 = 0.96$).
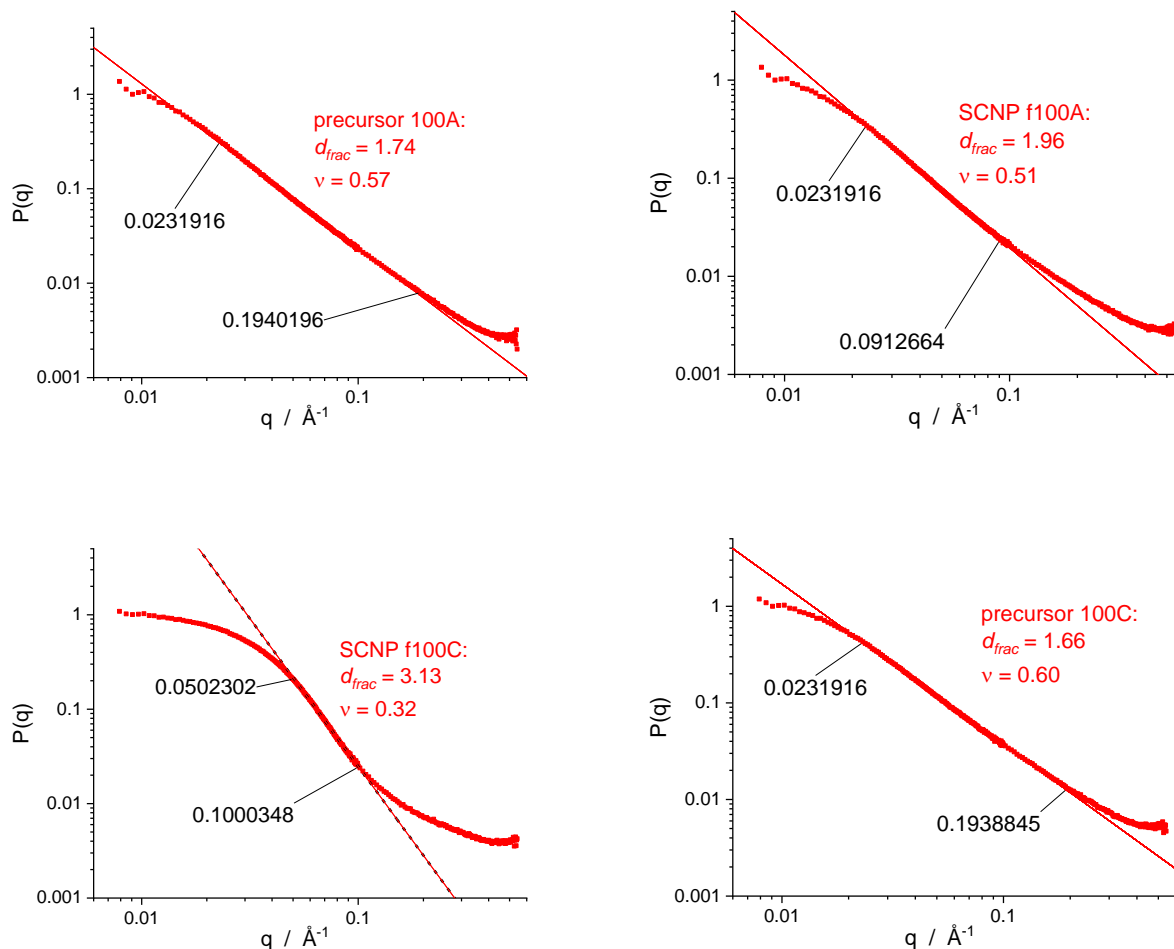
SI Figure 57. Evaluation of the scaling factor ν from the scattering curve (see equation SI-4 and 5). Scattering curves of the precursors (left) are given next to the corresponding SCNPs (right) of the longest chain range of the polymer library characterized via SANS technique 100A and 100C. The slope was derived by a linear fit within the assigned range of the scattering curve P(q).
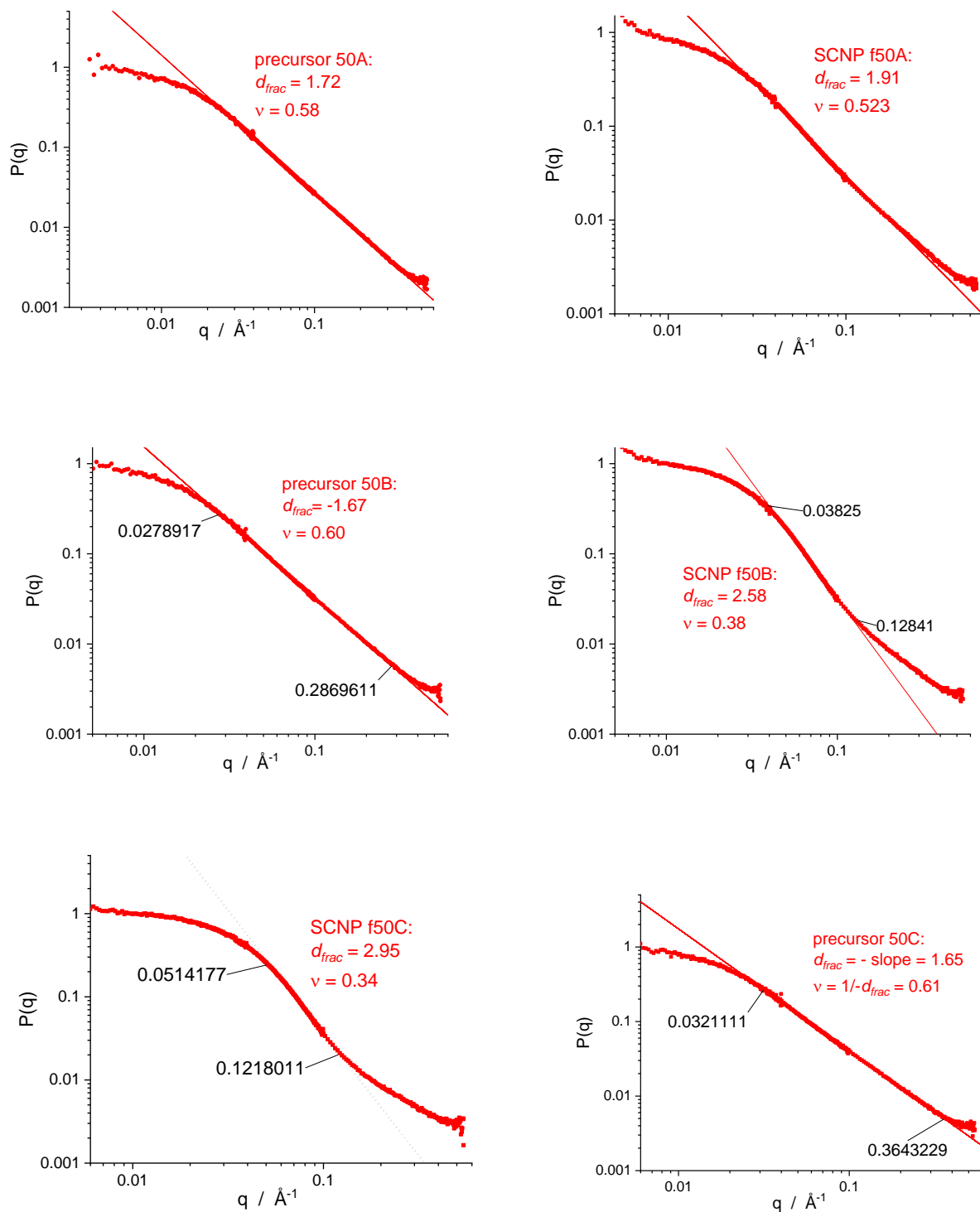
SI Figure 58. Evaluation of the scaling factor ν from the scattering curve (see equation SI-4 and 5). Scattering curves of the precursors (left) are given next to the corresponding SCNPs (right) of the middle chain range of the polymer library characterized via SANS technique (50A, 50B, and 50C). The slope was derived by a linear fit within the assigned range of the scattering curve P(q).
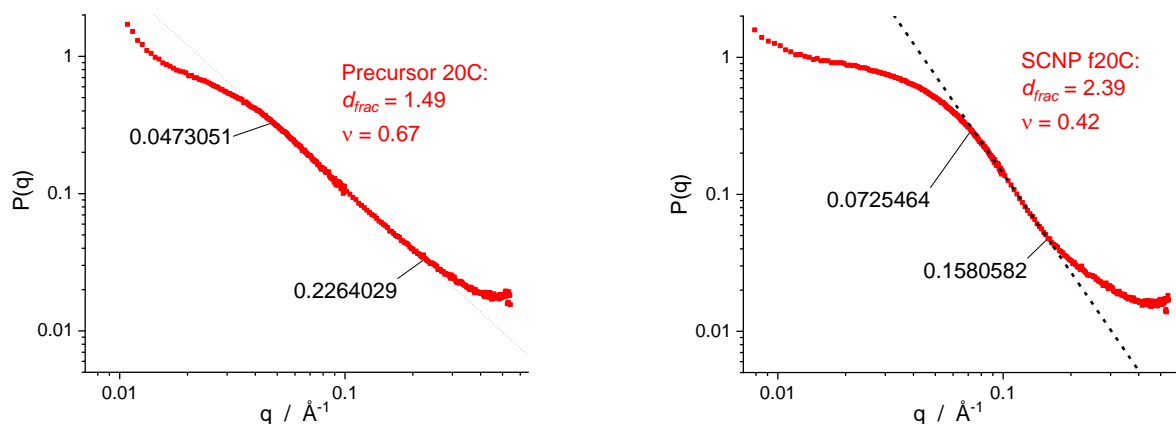
SI Figure 59. Evaluation of the scaling factor v from the scattering curve P(q) (see equation SI-4 and 5). Exemplary scattering curves of the precursors 20C (left) are given next to the corresponding SCNPs f20C (right).

6.3. Fitting SANS Data to Form Factor Models

6.3.1. *Flexible Cylinder* Model

The form factor *flexible cylinder* (SasView application) is fundamentally based on simulations of a discrete representation of a worm-like chain model of Kratky and Porod.[23] The employed version of the form factor implements corrected terms of Pedersen and Schurtenberger, which are based on different terms of Sharp, Bloomfield, Burchard and Kajiwara.[23–25] As depicted to the left in SI Figure 60, the polymer chain of the form factor model *flexible cylinder* is normalized by the volume of a flexible cylinder, defined by the contour length L (in means of the total chain length), the thickness $2R$ and locally stiff segments of the persistence length l_p. L, l_p and $2R$ are the output data, correlating to the required input data of the R_g and the DP (amongst other) of each sample as indicated in SI Figure 60. The plot corresponding to the default parameters of the model is shown to the right of SI Figure 60. For the required input-parameters of the fitting of the model form factor *flexible cylinder* to the experimental scattering curves, the scattering length density SLD of the solvent THF-d_8 (SLD = 0.183 10^{-6} Å^{-2}; calculated by the scattering calculator of the National Institute of Standards and Technology (NIST)[26]) is employed for all samples. The DP, obtained from DSEC-D4, and the R_g, obtained from manual ZIMM analysis of the SANS data, are used as input-data for the fitting of each sample.
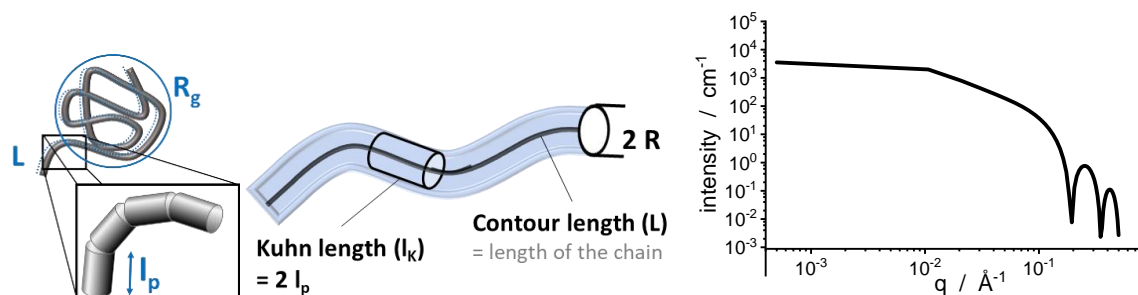
SI Figure 60. Scheme of the key output data of the form factor flexible cylinder, given by the radius of the normalized cylinder (2R), the contour length of the chain L, and the persistence length l_P (right). The output data is correlated to the input data of the R_g (amongst other) as indicated to the left. The plot corresponding to the default parameters of the model flexible cylinder is shown to the right.

For the form factor fitting we focus on the results correlated to the stiffness (Kuhn length l_K) of the polymer backbone, which can generally be described by the segment length of the polymer chain. The segment length is equal to the length of the freely-jointed part of a theoretical chain, which has the characteristic chain dimensions of the

particular real polymer.[27–29] The polymer can be described as a flexible rod below the scale of the persistence length l_p in turn, as applied in the form factor *flexible cylinder*. Following relation is true between the Kuhn length l_K the conventionally more frequently employed term of the persistence length l_p true (SI-12).

$$l_K = 2 \cdot l_P \tag{SI-12}$$

Therefore, the form factor *flexible cylinder* facilitates to estimate the stiffness of the linear backbone of the precursor chains by the indirect calculation of the Kuhn length l_K.

6.3.1.1. Choice of the Fit-Range (Model *Flexible Cylinder*)

Iterative improvement of the fit quality (reduction of residuals between the model form factor and the experimental scattering curves) was achieved due to the variation of both, the fit-parameters of the model and the considered q-range of the experimental data. Our team kept very similar parameters for all comparable samples to ascertain comparable results. Herein, the optimization of the parameters was performed in order to fit best all samples within the molar mass ranges (20 kDa, 50 kDa, and 100 kDa respectively). The iterative process is shown exemplarily for the scattering data of the 100 kDa precursor samples in the following SI figure 61.
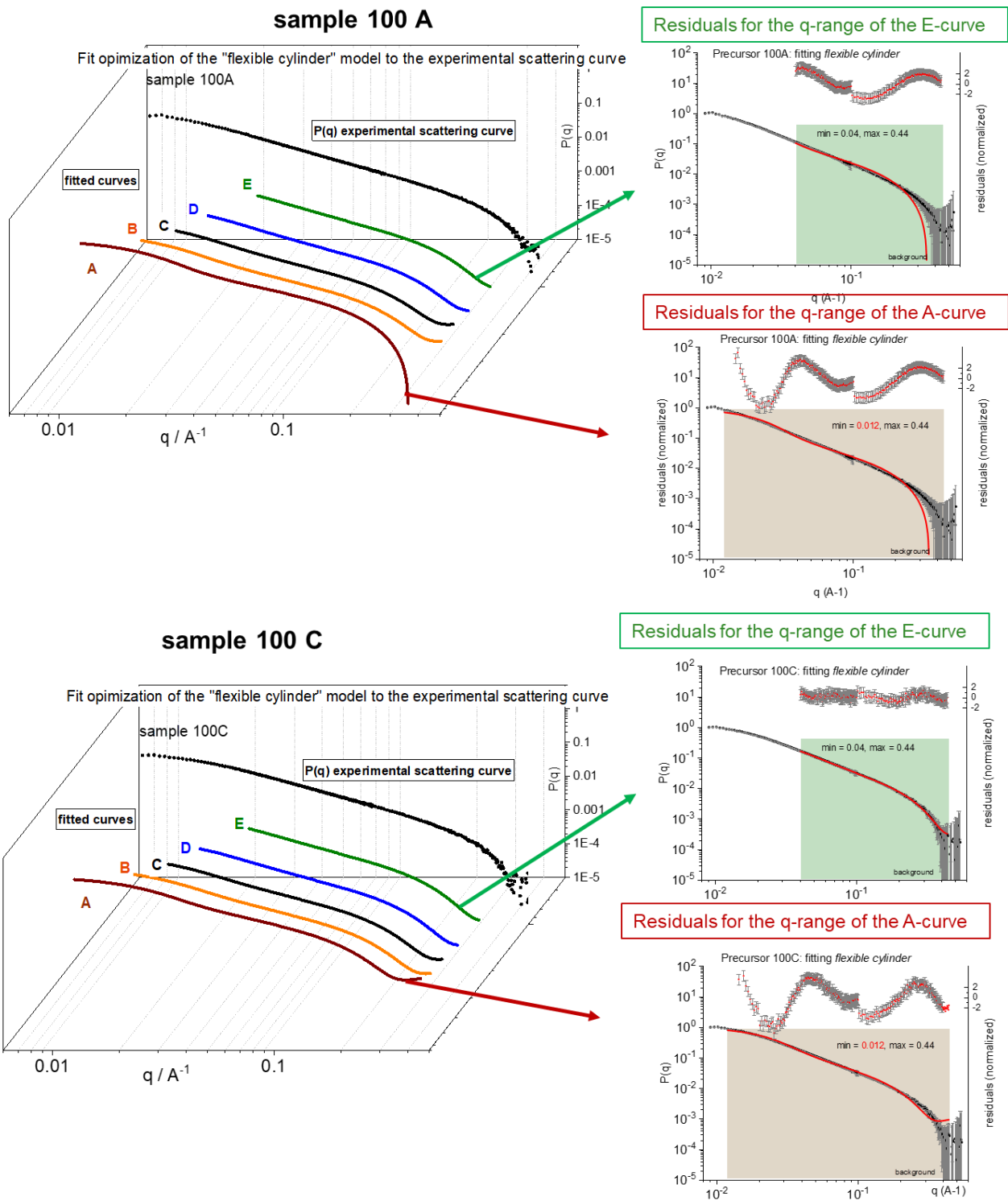
SI figure 61. Optimization of the fit by using flexible cylinder model to the experimental scattering curves (left graphs) of sample 100 A (top) and 100C (bottom). To ascertain comparability of the results, the residuals of the fit are minimized by variation the q-ranges of the experimental data for both samples (left graphs, z-axis). The best fit quality is obtained for the residuals of the E-curve (green) to the cost of a reduced set of data points employed for the fit. This example shows a clear deviation of the experimental scattering behaviour to the flexible cylinder model the low q-range. The decision of the choice of the q-range is justified in the next figure.

The following figure shows the results of the Kuhn length and the corresponding residual obtained for the form factor fitting flexible cylinder for sample 100C in dependency of the employed q-range (see the q-ranges A-E in SI

figure 61). Minimum residual, but reproducible Kuhn lengths are obtained for the q-range D. Herein, the fit for all 100 kDa samples is applied to the q-range D as shown in SI figure 61.
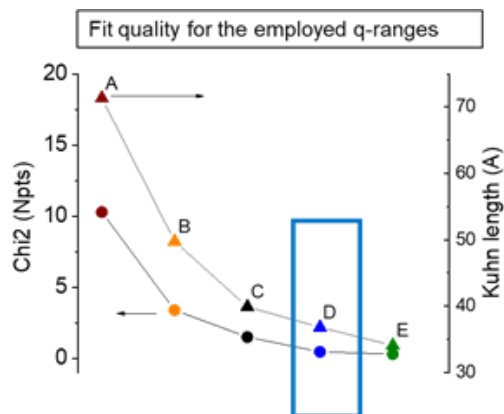
SI Figure 62. The justification of the suitable q-range in order to obtain an optimal fit (low residuals but at once including as much data points as possible) is enabled by the plot of the obtained Kuhn length next the residuals of the fit, in order to ascertain reproducibility

6.3.1.2. Fitting (Model *Flexible Cylinder*)

SI Figure 64 show the optimized fitting curves of the model form factor *flexible cylinder* (red curve) for all precursor samples characterized by SANS. The corresponding normalized residuals are given above, related to the left y-axis. The experimental scattering curves P(q) (black data points with uncertainties) are included and show high agreement to the fitted curve. The fit quality is high for a large q-range (minimum and maximum of the q-range is assigned for each fit) for the smaller polymers, whereas the fit for the samples 100A and 100C need to be applied to a limited q-range for reasons discussed above.
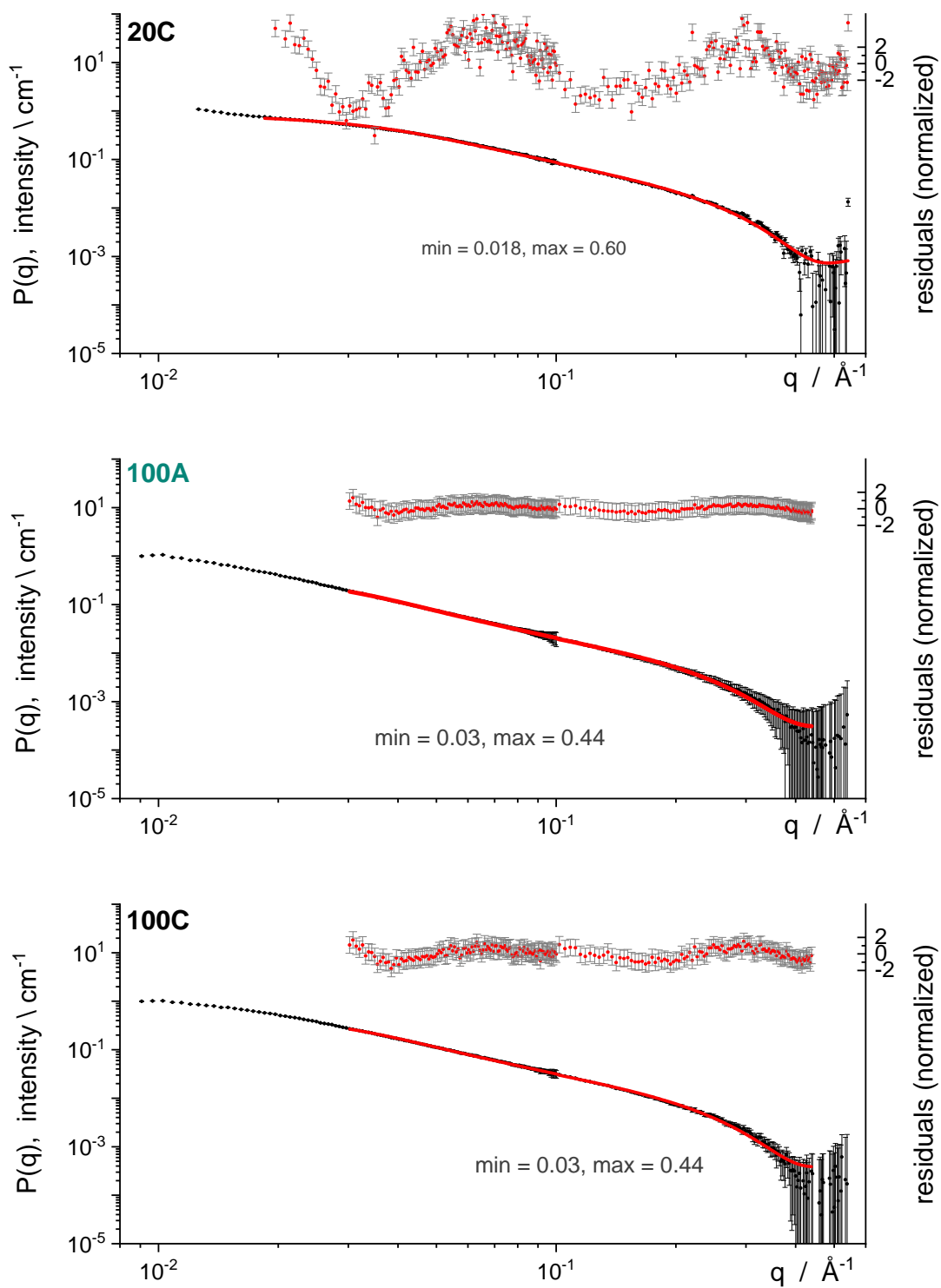
*SI Figure 63. The experimental scattering curves P(q) (black data point with uncertainties) and the fit of the model form factor flexible cylinder (red curve) for the precursor sample **20C** (top) and the precursor of approximately 100 kDa (**100A**, **100C**). Fitting was performed to the same q-range of experimental data for similar molar mass of the samples. The fit quality is given by the normalized residuals above the model curve, related to the left y-axis.*
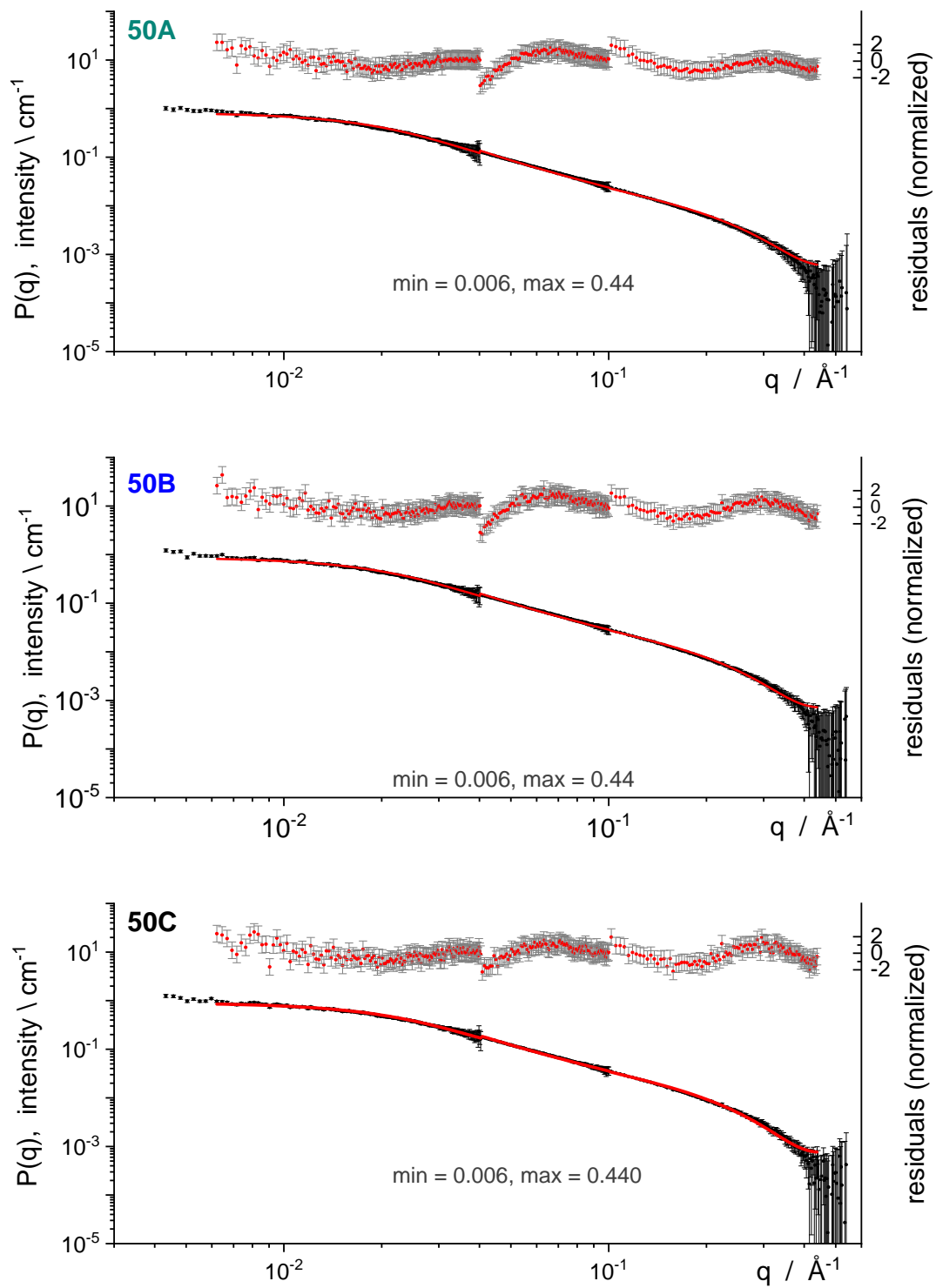
SI Figure 64. The experimental scattering curves P(q) (black data point with uncertainties) and the optimized fit of the model form factor flexible cylinder (red curve) for the precursor samples of approximately 50 kDa (50A, 50B, 50C). Fitting was performed to the same q-range of experimental data for similar molar mass of the samples. The fit quality is given by the normalized residuals above the model curve, related to the left y-axis.

The fit to the form factor model *flexible cylinder* is applied to the same q-ranges for the scattering curves of the precursor of approximately 100 kDa as follows.

6.3.1.1. Results (Model *Flexible Cylinder*)

The results of the model form factor fitting *flexible cylinder* for all SANS-characterized precursor are given in the following table. All obtained Kuhn lengths are discussed the main text. As explained in SI figure 61, the optimization of the fit to the model form factor flexible cylinder allows highest compatibility for the samples of the same mass range, as for such the same q-ranges are employed. Only the 50 kDa samples were characterized via SANS technique for all three functional group densities (50A, 50B and 50 C). The Kuhn lengths in dependency of the functional group decoration %PFB for the 50 kDa samples shows clear increase of l_K (chain stiffness) in the order A > B > C. This indicates maximal solubility for the polymer chain of sample 50A in THF or chemical integrity, respectively. As the bending stiffness of the linear precursor determines the probability of intramolecular interaction in space, but at once quantitative PFTR folding was observed for the C-samples, we conclude negligible influence of changing backbone composition or stiffness of the precursors on the SCNP morphology.

SI Table 5. Results of the model form factor fitting flexible cylinder for all SANS-characterized precursor samples. The quality of the fit (the residual Chi2), the contour length, the Kuhn length l_K and the radius of the hypothetic flexible cylinder allow for estimation of the stiffness of the precursor library.

	PFB (%)	Chi2 (Npts)	contour length (Å)	uncertainty	Kuhn length l_K (Å)	uncertainty	Radius R (Å)	uncertainty
20C	31	8.9	383	1.7	32	0.3	8	**0**
50A	5	0.7	1389	24	36	0.9	8.1	**0.1**
50B	14	0.8	1150	15	40	0.8	8.5	**0.1**
50C	29	0.7	922	10	42	0.8	8.5	**0.1**
100A	3	0.2	861	30	38	2.2	8.8	**0.2**
100C	28	0.5	731	13	37	1	8.6	**0.1**
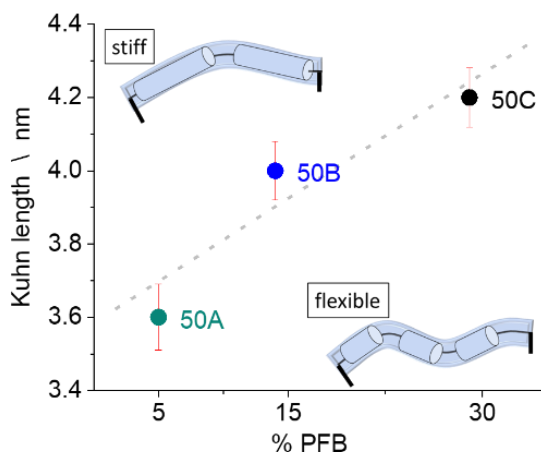
SI Figure 65. Plot of the Kuhn length l_K in dependency of the functional group decoration %PFB of the backbone for the precursor samples 50A (green), 50B (blue) and 50 C (black). Inserted cartoons of the meaning of the length of the Kuhn length are inserted for eased understanding. Relative uncertainties are given by the red bars. The plot indicates an increase of chain stiffness of the precursor in THF-d_8.

6.3.2. Polymer Excluded Volume Model

The model "*polymer excluded volume*" fits well to the experimental scattering curves $P_{c,\theta=0}(q)$ for all samples (precursor and SCNPs) and allows to confirm the manually evaluated parameters of the R_g (Zimm analysis) and ν (slope of scattering curves P(q)). To visualize the expected shape of the model applied to the parameters of the polymer library, we plotted in SI Figure 66 the form factor *polymer excluded volume* by use of the obtained average experimental values of R_g (derived by Zimm analysis of the SANS data) and ν for the precursor (black) and the SCNPs (blue).
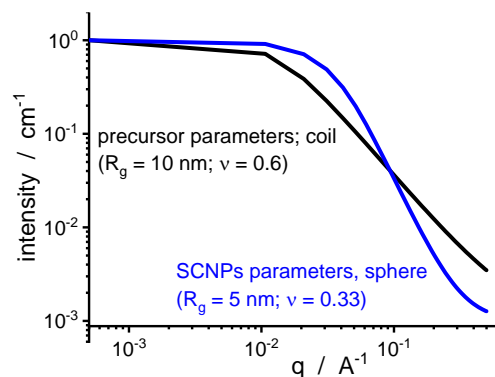
SI Figure 66. Model form factor polymer excluded volume by use of the obtained average experimental values of R_g and ν as input-parameters for the precursor (black) and the SCNPs (blue). The employed input-parameters are stated in the graph.

The applicability of the form factor *polymer excluded volume* (or, more precise: the implementation of its expression formulated in the year 1993) to the experimental data obtained for the polymer library is confirmed in by both the flexibility of the precursors (see chapter "*Flexible Cylinder* Model") and by the good solvent quality of the samples in THF-d_8, estimated by the second virial coefficient A_2 *via* Zimm characterization of the SANS data (see SI Table 10). We directly refer to the website of the application SasView.com for more detailed information about the features of the form factor *excluded volume*.[25]

6.3.2.1. Fitting (Polymer Excluded Volume Model)

SI Figure 67 to SI Figure 69 show the fitting of the model form factor *polymer excluded volume* (red curve) and the experimental P(q) data (dots with corresponding error bars). The precursor samples (black data points) are given next to the left to the corresponding SCNP (blue data points). The quality of the fit is given on the top of the fitted curve by the normalized residuals (linked to the right axis). We took caution to choose the same q-ranges for the fits for both samples of the corresponding pairs (precursor and SCNPs) in order to ascertain comparable and reliable results. Fitting the experimental data to the form factor for both samples in the same q-ranges was not trivial in all cases and turned to the drawback of the fit-quality (residuals) for some samples.
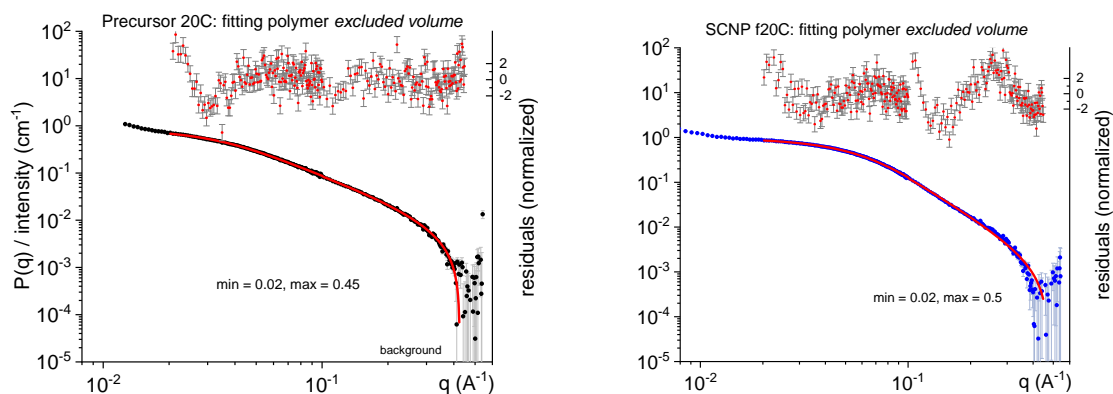
SI Figure 67. Plots of the optimized fitting of the model form factor polymer excluded volume (red curve) to the experimental scattering curves P(q) of the precursor samples (left graphs, black scattering data points with uncertainties) and to the corresponding SCNP (right graph, blue scattering data points with uncertainties). The fit is applied to the same q-range of the experimental data for both the precursor and the pairing SCNP, as the label of q-range shows in each graph. The corresponding normalized residuals of the fit are given above the red model curve, related to the left y-axis.
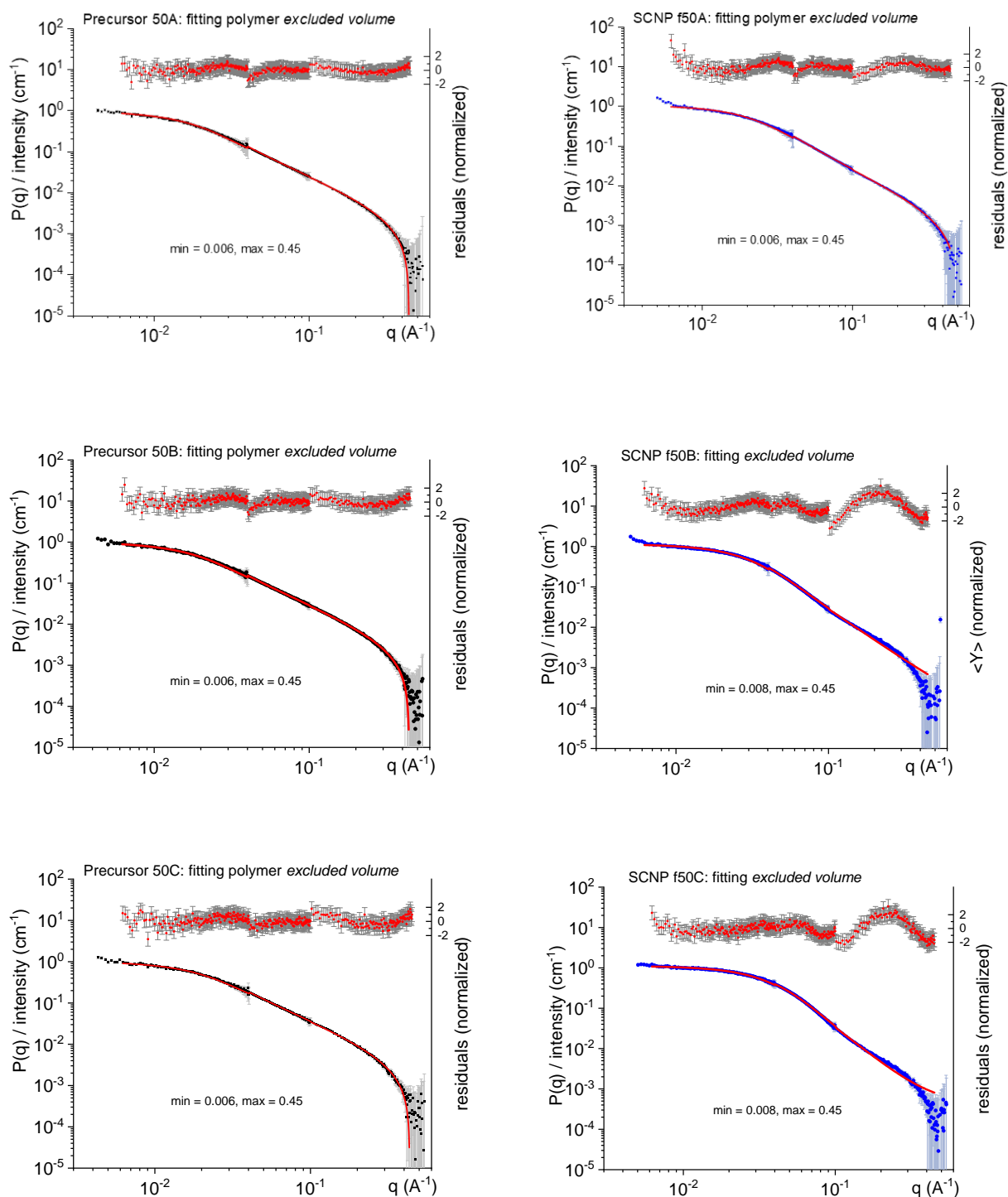
SI Figure 68. Plots of the optimized fitting of the model form factor polymer excluded volume (red curve) to the experimental scattering curves P(q) of the precursor samples (left graphs, black scattering data points with uncertainties) and to the corresponding SCNP (right graph, blue scattering data points with uncertainties) of the samples of approximately 50 kDa. The fit is applied to the same q-range of the experimental data for both the precursor and the pairing SCNP, as the label of q-range shows in each graph. The corresponding normalized residuals of the fit are given above the red model curve, related to the left y-axis.
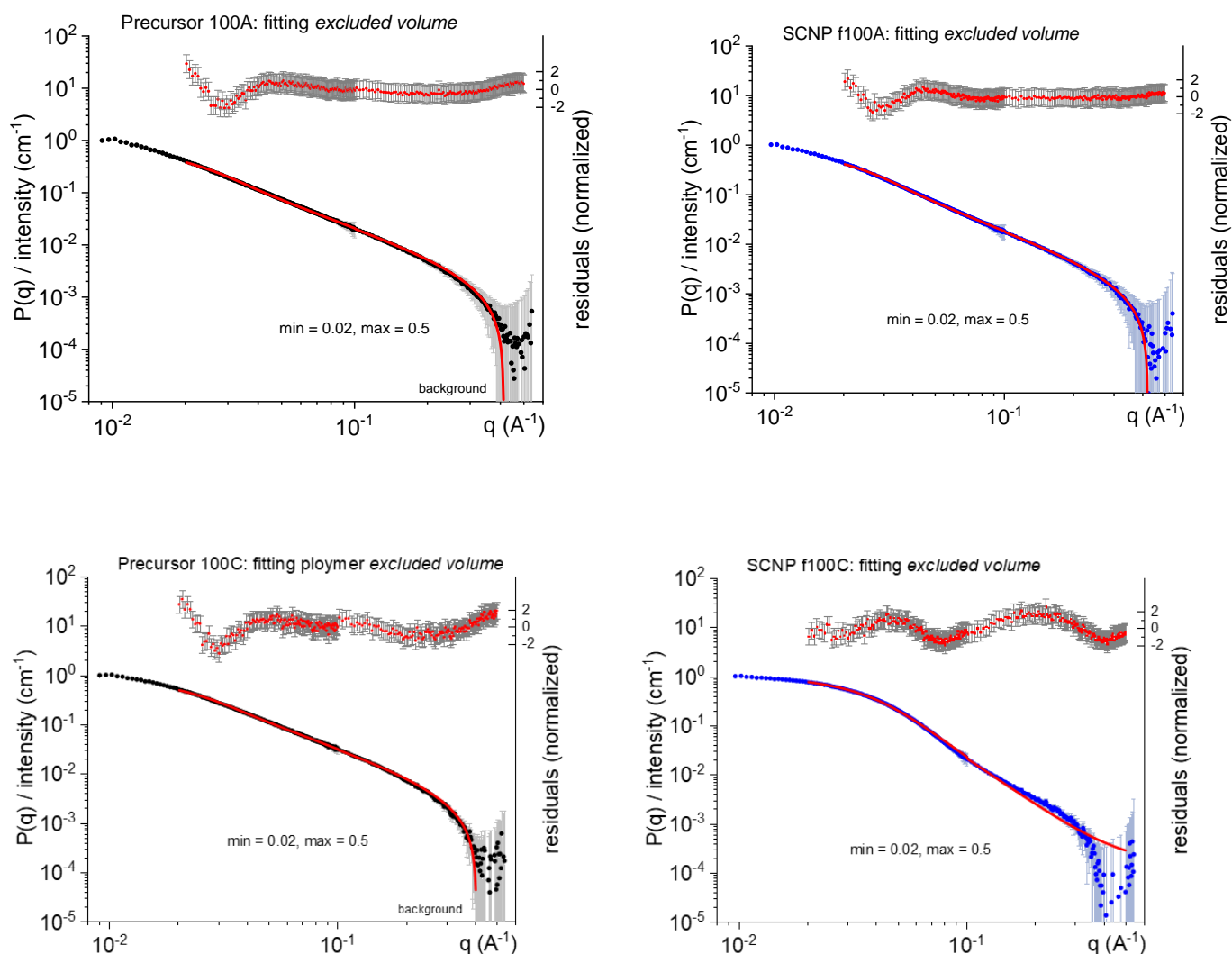
SI Figure 69. Plots of the optimized fitting of the model form factor polymer excluded volume (red curve) to the experimental scattering curves P(q) of the precursor samples (left graphs, black scattering data points with uncertainties) and to the corresponding SCNP (right graph, blue scattering data points with uncertainties) of the samples of approximately 100 kDa. The fit is applied to the same q-range of the experimental data for both the precursor and the pairing SCNP, as the label of q-range shows in each graph. The corresponding normalized residuals of the fit are given above the red model curve, related to the left y-axis.

6.3.2.1. Results (Polymer Excluded Volume Model)

The results of the fittings of the form factor model *polymer excluded volume* are shown in the SI Table 10. Both results of these fits the radius of gyration ($R_{g,model}$) and the scaling factor ν_{model} validate the data obtained from manual ZIMM analysis (R_g) and manual evaluation of the scaling factor (ν). The SI Figure 70 shows the agreement of the results obtained from the form factor fitting *polymer excluded volume* and the manually evaluated results of the SANS data. We note, that the obtained error bars for the $R_{g,model}$ (SI Figure 70, red bars) are generally higher for the precursor samples. We assume that the high sensitivity of SANS to impurities or a polydisperse sample lead to this phenomenon, which go beyond the sensitivity of MALS detection. In contrast, the measurements of the SCNPs benefit from multiple purifications along the SCNP synthesis route, leading to decreased Đ or higher purity, respectively.

SI Table 6. Results of the fitting of the model form factor excluded volume (Sasview application) to experiemtnal scattering data of the precursor (left) and the SCNPs (right), characterized via SANS technique.

	precursor						SCNPs				
sample	Chi2 [Npts]	R_g [nm]	+-	ν	+-	sample	Chi2 [Npts]	R_g [nm]	+-	ν	+-
20C	3.6	5.1	0.14	0.57	0	**f20C**	5.1	3.1	0.03	0.34	0.01
50A	0.2	13.9	1.97	0.62	0.01	**f50A**	0.3	10.3	0.94	0.52	0.01
50B	0.3	12.9	1.52	0.62	0.01	**f50B**	1.0	6.7	0.3	0.39	0.01
50C	0.4	11.2	1.24	0.63	0.01	**f50C**	1.1	5.3	0.19	0.33	0.01
100A	1.0	12.7	1.63	0.63	0.01	**f100A**	0.2	15.2	3.32	0.58	0.01
100C	0.4	15.8	3.87	0.63	0.01	**f100C**	1.1	5.9	0.23	0.32	0.02
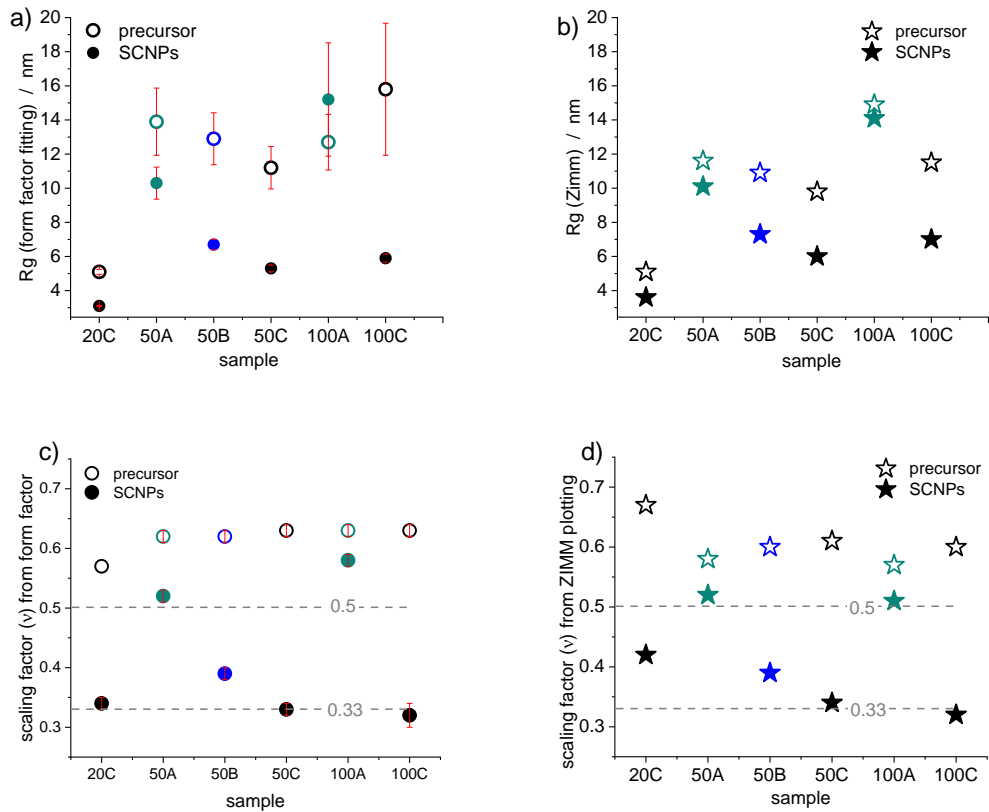
SI Figure 70. The results of the fit of the experimental SANS data to the form factor polymer excluded volume (SasView application) are shown in the (left graphs, dots) next to the results of the manual evaluation (right graphs, stars) of the R_g (top graphs; a and b) and the scaling factor ν (bottom graphs; c and d). The comparison of the results show good agreement of the data, confirming the reliability of absolute ZIMM calculation.

7. Additional interpretation of experimental data

7.1. Application of mathematical expressions for estimation of the SCNP compaction

The following figure shows the chain collapse (justified by the R_g) in dependency of the ligation density LD of the SCNPs. As direct reference of compaction (size, density etc.) is often useful not due to lack of comparability to other SCNP systems in literature we consider the only yet stated relation between folding-induced chain collapse and extend of intramolecular interaction by Colmenero et al..[30] Even if this relation for estimation of the size reduction upon folding applies for reversible folding scenarios, we apply it to our experimental data. For precursor chains of fraction of %PFB groups involved in intramolecular ligation (original literature: reversible bonds), the expected size of the SCNPs is estimated by $R_g = R_{g, precursor} (1 - \%PFB)^{0.6}$. The results from this calculation (SI Figure 71, crosses) show rather underestimation of the total chain collapse with respect to the experimental data (SI Figure 71, dots). We conclude, that contriving general trends for SCNP design is constantly improving towards applicable predictions of any SCNP system.
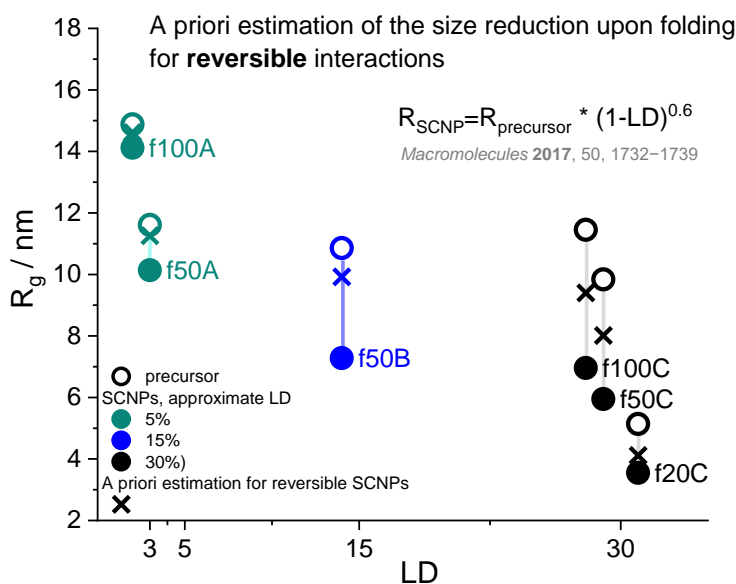
SI Figure 71. A comparison of the size reduction predicted by the expression of Colmeneo et al. for reversible bonds (crosses) and experimental data obtained by SANS data obtained from irreversible chain collapse from precursor (open dots) to the corresponding SCNP (full dots) in dependency of the functional group fraction involved in the intramolecular chain collapse (LD).

7.2. The Flory Fox parameter

The generalized ratio κ (R_η/R_g) sets the mass distribution of chain segments around the centre of gravity of the polymer in relation to the hydrodynamic distribution of the chain segments (see main text). Herein, κ is directly related to the Flory-Fox parameter Φ_F and can be used as a measure of to what extend the polymer is solvent-drained.[31] Flory-Fox equation describes the relation between the intrinsic viscosity $[\eta]$, the R_g and molar mass (equation SI-13), allowing to refer scattering data with results of viscometric characterization.

$$\text{Flory -Fox equation: } [\eta] = \Phi_F \left(\frac{R_g^3}{M} \right) \tag{SI-13}$$

The Flory Fox parameters of the SCNPs are given in the SI Figure 72. As expected, we obtain an increased Flory-Fox parameter with increasing intramolecular ligation LD due to linear chain folding (A > B > C). This observation

is reasonable due to the increase of the segment density for the SCNP samples, which correlates to smaller R_η or a higher value of κ, respectively (see SI Table 9 and10).[19]
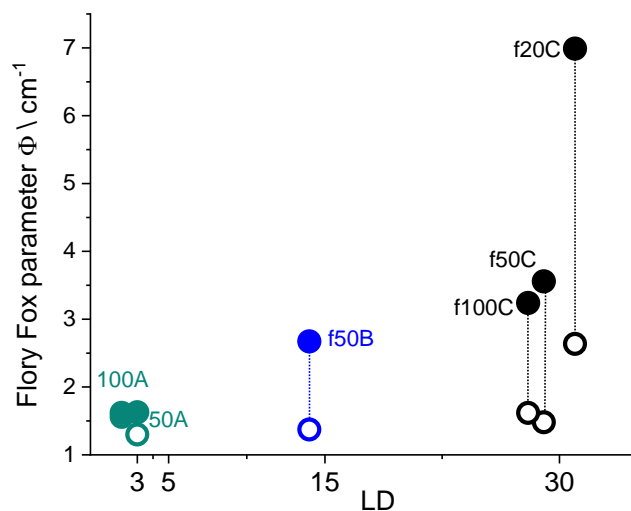
SI Figure 72. The Flory-Fox parameter Φ obtained for the SCNPs of the precursor library.

For the same molar mass and LD, one can expect a dependency of the rheological features from the solvent quality as good solvents will lead to chain expansion. A high extent of solvent-draining is in direct correlation to a relatively large viscosimetric radii and Flory-Fox parameters. These considerations show that valuable insights of chain conformation of SCNPs can be obtained by simple comparisons of the profound measures from scattering techniques and viscometry.

7.3. The drainage factor

The chain collapse of SCNPs can be directly estimated by the relative change of the R_g due to intramolecular interaction according the contraction factor g (a discussion of this is given in the main text). One can derive further topological descriptions of macromolecules if g is conjunct to the contraction factor of the viscosity g'.[19,32] Kurata assumed a corresponding power law and established the so-called drainage exponent ε (equation SI-14),[33] for which a range between 1.5 and 0.5 is usually observed in the discipline of branched polymers.[34]

$$g' = g^\varepsilon \tag{SI-14}$$

The study of the correlation between g' and g for branched polymers was once contemplated by Zimm and Kilb to describe the hydrodynamic properties.[35] The non-universality of ε is discussed by Lederer et al. in greater detail, showing that ε can correlates to the degree of branching independent of the molar mass under assumptions. Generally, the value for ε of 0.5 indicates polymer structure with low branching whereas 1.5 applies to molecules of high branching. Even if one cannot speak of branched polymers for SCNPs, they have a kind of intramolecular ligation. SI Figure 73 shows the drainage factors ε obtained for the sample set of SCNPs, which were characterized via SANS technique.
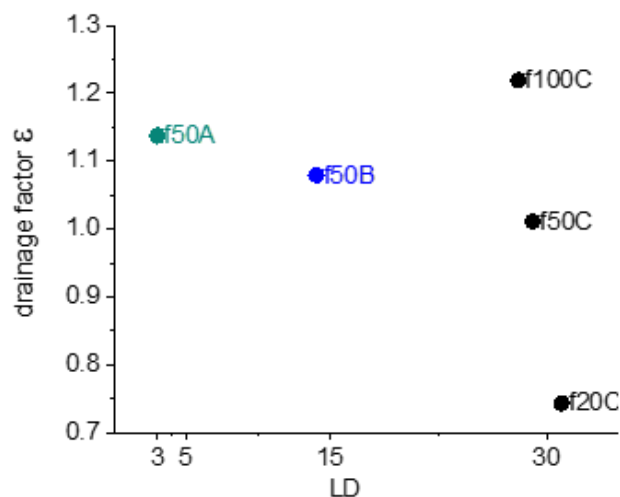
SI Figure 73. The drainage factor ε for the SCNPs characterized via SANS technique, allowing for an interesting contemplation of the the morphology of SCNPs. The obtained values of ε are between 0.7 > ε > 1.3). The drainage exponent decreases with increasing LD for comparable molar mass (f50A > f50B > f50C) and increases with increasing molar mass for comparable LD (f100C > f50C > f20C).

As similar considerations have not been applied to SCNPs to date, to the best of our knowledge, we present our results without further interpretation. We obtain values of the drainage exponent (0.7 > ε > 1.3) are within the limits popular in the discipline of branching polymer research. Furthermore, we see a linear decrease of ε with increasing LD (for comparable molar mass; f50A > f50B > f50C), and an increase of ε with increasing molar mass (for comparable LD; f100C > f50C > f20C).

7.4. The impact of mass increase upon folding on the apparent density

To visualize the limits the value of d_{app} for very small polymers, we plotted the theoretical R_g as a function of molar mass for the observed average experimental densities of both the SCNP (Figure below, black full dots, 0.2 g cm^{-3}) and the precursor (grey open dots, 0.02 g cm^{-3}). The theoretical R_g was calculated according the equation SI-15.

$$R_g = \sqrt[3]{3\,M_w/4\pi N_A d_{app}} \qquad\qquad \text{(SI-15)}$$

SI Figure 74 indicates that the mass change due to the incorporation of the external crosslinker has the most significant impact on the d_{app} of the smallest SCNPs with the highest LD, exemplarily shown for the SCNP sample f20C (the red arrow assists as guide for the eye).
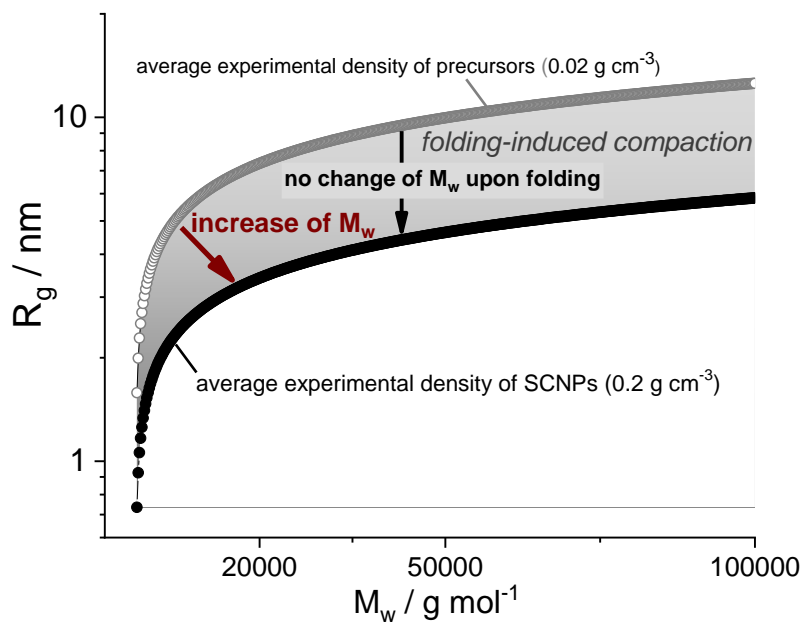
SI Figure 74. Theoretic R_g as a function of molar mass for the observed experimental average apparent densities d_{app} of both the SCNP (black full dots, 0.2 g cm^{-3}) and the precursor (grey open dots, 0.02 g cm^{-3}). The grey area indicates the folding-induced compaction. The red arrow shows the impact of the mass increase upon folding via incorporation of external crosslinker, whereas the folding-induced change of the d_{app} is more intuitive for folding events without mass change. These effects become meaningful for SCNP folding of very small precursors upon high mass change.

The graph shows that the applicability of the measure of the on the d_{app} is limited for SCNPs, synthesized under significant change of molar mass mass due to incorporation of external crosslinker.

8. Appendix

8.1. General procedure of thermally induced free radical polymerization (FRP)

The synthesis of linear FRP copolymers next to the defined precursor library synthesized *via* controlled polymerization is beneficial for several reasons. In contrast to the rather narrow distributed precursor library, their polydispersity $Đ$ spans the at least required two orders of magnitude of molar mass range, enhancing the performance of angle dependent scattering experiments for Zimm analysis, respectively. Furthermore, FRP synthesized polymers allow for more accurate batch dn/dc determination as described above. A FRP-test copolymer of comparable composition of B-samples of the precursor library (15% PFB) is synthesized according following procedure.
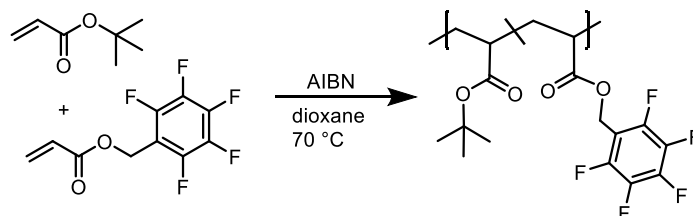
SI Figure 75. Reaction scheme of thermally induced free radical polymerization (FRP) of poly(PFB-stat-^{t}Bu) acrylates, employed for test copolymers. Feed ratios are given in the table below.

Molar amounts and identity of reactants employed for RAFT polymerization are given in SI Table 7. An evacuated Schlenk tube was charged with recrystallized radical initiator AIBN, uninhibited *tert*-butyl acrylate, uninhibited PFBA and dioxane. The solution was deoxygenated by four freeze pump-thaw cycles and heated to 70 °C to initiate polymerization. After 15 h the mixture was allowed to cool to ambient temperature and the reaction was quenched by exposing the solution to air. The viscous solution was diluted with dioxane and precipitated in cold n-hexane (500 mL) twice. The solvent was removed, and the poly(PFB-stat-^{t}Bu) acrylate polymer was dried in *vacuo*.

SI Table 7. Molar amounts of the monomer tert-butyl acrylate (^{t}BuA) and pentafluorobenzyl acrylate (PFBA), the initiator azobisisobutyronitril (AIBN) and the volume of the solvent dioxane for the thermally induced free radical polymerization (FRP) of poly(PFB-stat-^{t}Bu) acrylate copolymers, coined FRP copolymers.

	poly(PFB) acrylate homopolymer	poly(PFB-stat-^{t}Bu) acrylate
n_{tBuA} [mmol]	-	10.142
n_{PFBA} [mmol]	7.253	1.790
n_{AIBN} [mmol]	0.005	0.008
$V_{dioxane}$ [mL]	1.027	1.510

The ^{1}H NMR spectroscopy analysis showed 14% PFB (see structure at framed in SI Figure 76), which is comparable to the B-samples of the defined precursor library and therefore suitable for test reactions.

^{1}**H NMR** (500 MHz, CDCl$_3$) δ = 5.27 – 5.07 (br s, **9**), 2.49 – 2.03 (br, m, **2, 7**), 1.94 – 1.15 (**1, 5, 6**).

^{19}**F NMR** (470 MHz, CDCl$_3$) δ = -141.5 – -143.7 (br s, 2 F$_o$), -153.41 – -154.89 (br s, 1 F$_p$), -162.42 – -163.74 (br s, 2 F$_m$).

^{13}**C NMR** (125 MHz, CDCl$_3$) δ = 174.5 – 173.4 (**3, 8**), 145.7 (d, **12**), 141.7 (d, **13**), 137.4 (d, **11**), 109.5 (**10**), 80.4 (**4**), 53.3 (**9**), 42.9 – 40.5 (**2, 7**), 38.5 – 33.5 (**1, 6**), 28.5 – 26.5 (**5**).
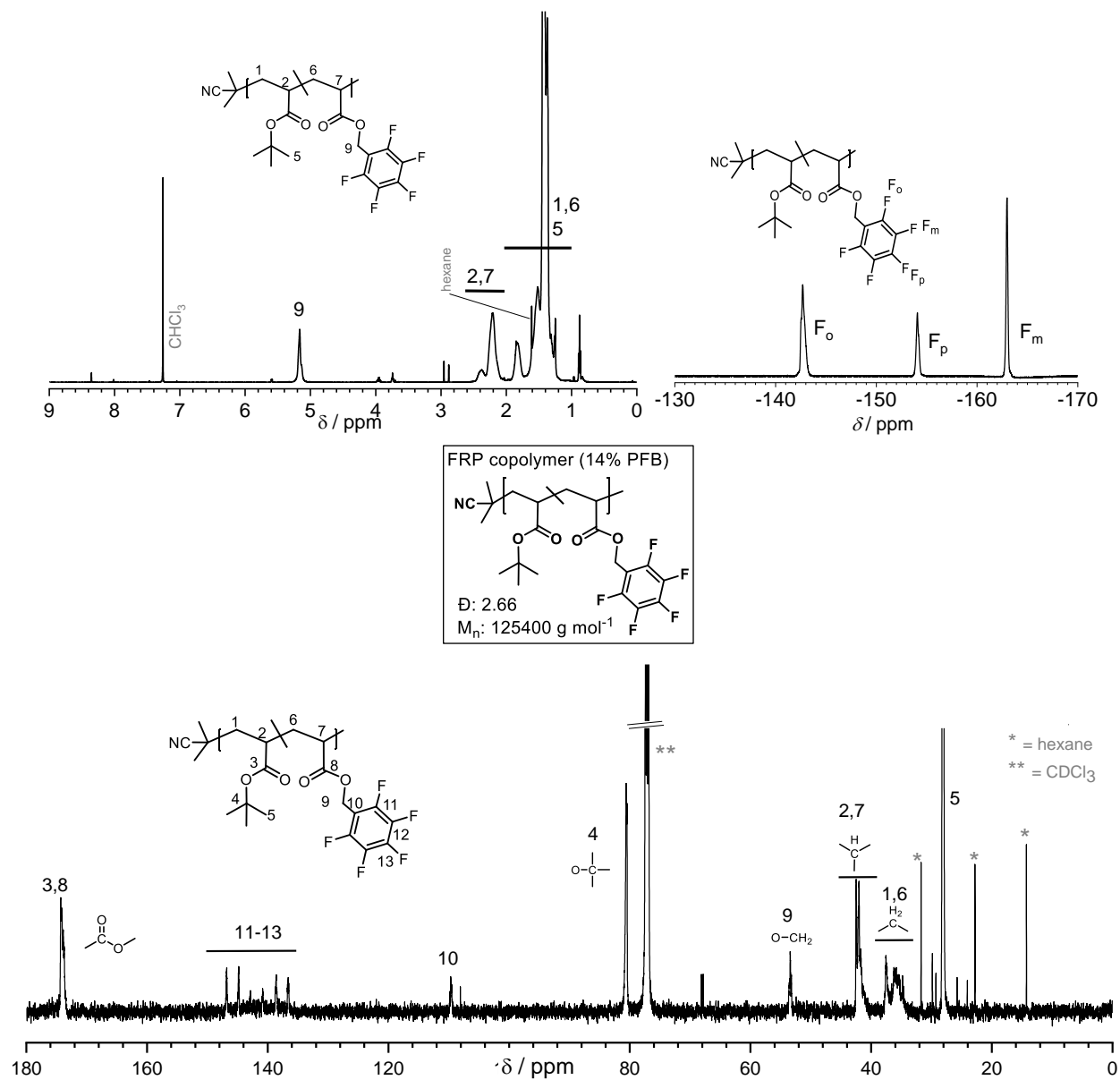
SI Figure 76. ^1H NMR spectrum (500 MHz, CDCl₃, top left), ^{19}F NMR spectrum (470 MHz , CDCl₃, top right),- and ^{13}C NMR spectrum (125 MHz, CDCl₃, bottom) of poly(^{t}Bu-stat- pentafluorobenzyl), obtained after thermally induced free radical polymerization (FRP). The results from SEC-D4 characterization are given next to the framed structure at the centre.

8.2. Characterization of the small RAFT test copolymer 10a

The small test copolymer **10a** was synthesized according the general RAFT polymerization procedure described below. The SI Figure 77 shows the most important detector signals of the SEC-D4 characterization of small test copolymer **10a**.
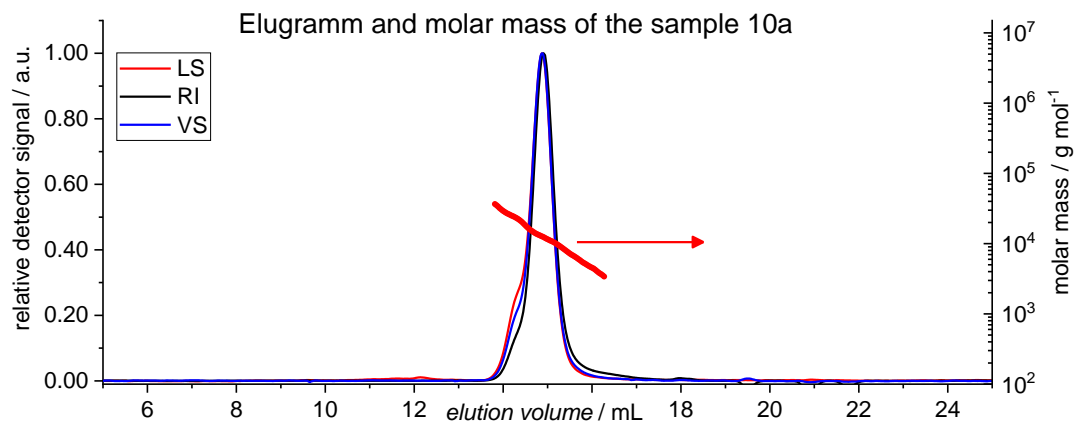
*SI Figure 77. SEC-D4 traces of the small test copolymer **10a** in THF after RAFT synthesis, showing the MALS detector signal (light scattering or LS, red), the dRI detector signal (black), and the viscosity detector signal (blue) of the SEC-D4 characterization of the RAFT precursor polymers. The molar mass is represented in red dots (referring to the right y-axis).*

The ^{1}H - ^{19}F -, and ^{13}C NMR spectra, the structure and the average characteristic values obtained from SEC characterization of **10a** is given in SI Figure 78.
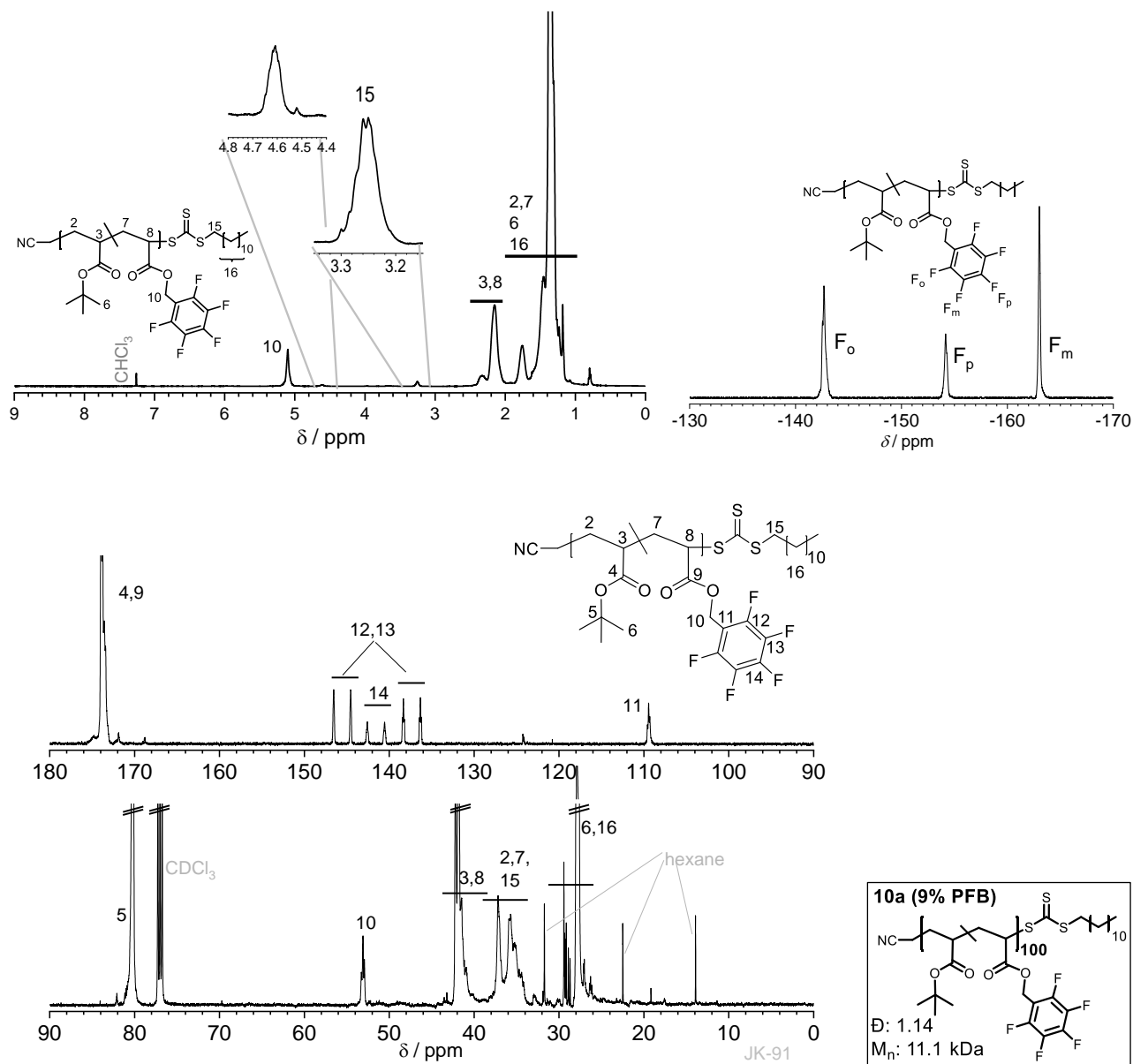
*SI Figure 78. ^{1}H NMR- (500 MHz, CDCl3, top left), ^{19}F NMR- (470 MHz , CDCl3, top right),- and ^{13}C NMR spectra (125 MHz, CDCl3, bottom) with the relevant labels of the test-copolymer **10a**, obtained after RAFT polymerization. The results from SEC-D4 characterization are given next to the framed structure at the right bottom. The characteristic RAFT end group signal **15** at 3.25 ppm (broad doublet) as well as the R-**CH**-(CO2)(ω) group (broad singlet) are zoomed in the ^{1}H NMR spectrum, which allows for quantification of RAFT end group removal representative for the whole precursor library.*

9. Structural and conformational parameters

SI Table 8. Main parameters of the polymer library determined via ^1H, and ^{19}F NMR spectroscopy and SEC-D4. The nine linear precursor samples and the amount of decoration with pentafluoro-benzyl groups (%PFB, top nine samples) are listed above the corresponding SCNPs (indicated by the letter "f" for folded), for which ligation density LD is shown. The results of the degree of polymerization (DP) and the refractive index increment (dn/dc) are given. Uncertainty weighted (±%) values of the absolute number average molar mass (M_n), the absolute weight average molar mass (M_w), the polydispersity ($Đ$) and the mass recovery, which applies for the given peak ranges. The right column gives the shift of elution volume of the obtained SEC elugrams, determined by the peak apex shift between the precursor and the corresponding SCNPs.

sample	PFB	DP	dn/dc	M_n	±%	M_w	±%	$Đ$	mass recovery	ΔV_e
precursor	%	absolute	mL g^{-1}	kDa		kDa			%	ml
20A	2	158	0.052	20.6	1.24%	22.5	1.23%	1.09	99.2	-
20B	14	133	0.051	19.4	1.50%	21.3	1.10%	1.10	95.6	-
20C	31	133	0.049	22.2	1.58%	23.8	1.73%	1.07	81.5	-
50A	5	414	0.052	55.4	1.36%	65.5	0.60%	1.18	98.0	-
50B	14	354	0.051	51.6	2.24%	63.8	0.43%	1.24	98.2	-
50C	29	302	0.049	49.4	2.36%	60.2	0.63%	1.22	100.5	-
100A	3	731	0.052	96.6	0.43%	116.6	0.30%	1.21	103.6	-
100B	14	745	0.051	108.0	0.89%	151.5	0.53%	1.40	100.4	-
100C	28	437	0.049	71.3	1.00%	83.4	0.40%	1.17	100.3	-
SCNP	%LD	CL per chain								
f20A	1	1	0.054	25.5	0.31%	29.3	0.43%	1.15	92.7	0.00
f20B	14	9	0.072	27.7	0.30%	32.4	0.43%	1.17	95.6	0.17
f20C	31	21	0.097	27.4	0.16%	30.4	0.20%	1.11	80.8	0.28
f50A	3	6	0.057	60.8	0.28%	72.0	0.17%	1.18	94.8	0.20
f50B	14	24	0.072	66.7	0.13%	79.9	0.10%	1.20	94.4	0.36
f50C	29	43	0.093	62.5	0.15%	77.1	0.10%	1.23	84.9	0.50
f100A	2	6	0.055	107.2	0.18%	127.3	0.10%	1.19	93.2	0.19
f100B	13	47	0.070	124.6	0.67%	176.1	0.30%	1.41	84.2	0.40
f100C	28	62	0.093	91.6	0.13%	111.2	0.10%	1.21	86.0	0.56

SI Table 9. Further parameters of the polymer library determined via SEC-D4. The nine linear precursor samples and amount of decoration with pentafluorobenzyl groups (%PFB, top nine samples) are listed above the corresponding SCNPs (indicated by the letter "f" for folded), for which the ligation density LD is given. The key parameters of SEC-D4 are given by the uncertainty weighted (±%) values of the absolute radius of gyration (R_g) and the scaling factor obtained from MALS, the hydrodynamic radius (R_h) obtained from QELS are given next to the viscometric radius (R_η), intrinsic viscosity ($[\eta]$), the viscosity based contraction factor (g´), the slope of the KMH-plot (α) and the scaling factor (ν).

sample	PFB	$R_{g,z}$ (MALS)	±%	$R_{h,z}$ (QELS)	±%	$R_{\eta,w}$ (VS)	±%	$[\eta]_w$	±%	g´	α	±%	ν (MALS)	±%
precursor	%	nm		nm		nm		ml g^{-1}						
20A	2	6.4	135.03%	n.a.	-	3.5	0.37%	12.7	0.26%	-	0.56	0.07%	1.36	131.38%
20B	14	8.4	68.90%	n.a.	-	3.3	0.37%	10.7	0.30%	-	0.55	0.09%	0.41	62.03%
20C	31	10.6	65.00%	n.a.	-	3.3	0.63%	9.4	0.89%	-	0.59	0.27%	0.24	19.69%
50A	5	10.0	23.67%	n.a.	-	6.3	0.23%	25.7	0.22%	-	0.60	0.04%	0.47	3.61%
50B	14	8.8	21.33%	n.a.	-	6.0	0.20%	22.8	0.16%	-	0.59	0.03%	0.56	2.87%
50C	29	10.0	25.17%	n.a.	-	5.5	0.27%	18.5	0.21%	-	0.57	0.03%	0.38	4.78%
100A	3	14.2	5.35%	9.1	90.10%	8.8	0.10%	38.3	0.21%	-	0.64	0.03%	0.43	0.88%
100B	14	19.0	5.87%	11.9	90.93%	9.2	0.20%	36.2	0.14%	-	0.54	0.02%	0.35	0.65%
100C	28	10.3	14.80%	7.3	89.73%	6.8	0.17%	24.4	0.20%	-	0.63	0.04%	0.50	2.51%
SCNP	%LD													
f20A	1	7.9	43.30%	n.a.	-	3.8	0.23%	12.4	0.44%	0.98	0.50	0.12%	0.29	5.66%
f20B	14	9.2	26.90%	n.a.	-	3.2	0.27%	6.9	0.36%	0.65	0.37	0.13%	0.20	3.92%
f20C	31	9.5	8.50%	3.2	60.73%	2.9	0.20%	5.6	0.46%	0.60	0.31	0.28%	0.24	1.63%
f50A	3	7.2	11.50%	5.9	78.83%	5.9	0.10%	18.8	0.15%	0.73	0.58	0.03%	0.40	2.83%
f50B	14	4.7	14.93%	5.7	34.40%	4.9	0.10%	9.6	0.22%	0.42	0.35	0.07%	0.39	4.64%
f50C	29	3.8	30.97%	5.0	29.37%	4.3	0.20%	6.9	0.56%	0.37	0.22	0.25%	0.35	9.40%
f100A	2	11.2	3.43%	9.4	56.37%	8.4	0.03%	30.6	0.09%	0.80	0.61	0.02%	0.55	0.55%
f100B	13	8.4	15.40%	9.0	48.37%	6.7	0.23%	12.0	0.50%	0.33	0.31	0.12%	0.42	2.30%
f100C	28	5.0	12.43%	5.8	28.20%	4.9	0.10%	7.3	0.38%	0.30	0.22	0.17%	0.36	2.27%

SI Table 10. *Main parameters of the selected sample set of the polymer library characterized via SANS. The selected six linear precursors and the amount of decoration with pentafluorobenzyl groups (%PFB, top nine samples) are listed above the corresponding SCNPs (indicated by the letter "f" for folded), for which the ligation density LD is given. The key parameters calculated from the SANS data are the scaling factor (ν), the absolute radius of gyration (R_g), the radius related contraction factor (g), and the second virial coefficient (A_2) as calculated using ZIMM analysis. Based on these primary data, the chain overlap concentration c* and the apparent density d_{app}, (both calculated by use of R_g from SANS and M_w from SEC-D4), the κ-parameter (κ, calculated by use of R_g from SANS and R_η from SEC-D4) are obtained. Model form factor fitting with the software SaSview.org was employed to calculate the Kuhn length (l_K) of the precursor by use of the model flexible cylinder, and the radius of gyration ($R_{g, model}$) and the scaling factor (ν_{model}) by the use of the model excluded volume.*

sample	PFB	R_g	c*	g	ν	κ	d_{app}	A_2	$R_{g, model}$	ν_{model}	l_K
precursor	%	nm					g cm^{-3}	mol mL g^{-2}	nm		nm
20A	2										
20B	14										
20C	31	5.1	71.2	-	0.67	0.66	0.072	2.11E-03	5.1	0.57	3.2
50A	5	11.6	16.6	-	0.58	0.6	0.018	2.04E-03	13.9	0.62	3.6
50B	14	10.9	19.5	-	0.6	0.63	0.021	1.35E-03	12.9	0.62	4
50C	29	9.8	25.4	-	0.61	0.62	0.026	8.65E-04	11.2	0.63	4.2
100A	3	14.9	14.0	-	0.57	0.61	0.013	-9.00E-04	12.7	0.63	3.8
100B	14										
100C	28	11.5	21.7	-	0.6	0.64	0.021	-1.48E-03	15.8	0.63	3.7
SCNP	%LD										
f20A	1										
f20B	14										
f20C	31	3.6	202.5	0.50	0.42	0.93	0.256	-1.42E-03	3.1	0.34	n.a
f50A	3	10.1	25.2	0.76	0.52	0.64	0.026	-7.06E-04	10.3	0.52	n.a
f50B	14	7.3	65.0	0.45	0.39	0.74	0.081	-6.17E-04	6.7	0.39	n.a
f50C	29	6.0	110.5	0.37	0.34	0.81	0.146	-1.22E-04	5.3	0.33	n.a
f100A	2	14.1	16.5	0.90	0.51	0.67	0.016	-1.19E-03	15.2	0.58	n.a
f100B	13										
f100C	28	7.0	96.39	0.37	0.32	0.83	0.134	1.05E-04	5.9	0.32	n.a

10. References

(1)   Huggins, M. L. The Viscosity of Dilute Solutions of Long-Chain Molecules. IV. Dependence on Concentration. *J. Am. Chem. Soc.* **1942**, *64* (11), 2716–2718.

(2)   Berek, D. Size Exclusion Chromatography - A Blessing and a Curse of Science and Technology of Synthetic Polymers. *J. Sep. Sci.* **2010**, *33* (3), 315–335.

(3)   Noy, J.; Friedrich, A.; Batten, K.; Bhebhe, M. N.; Busatto, N.; Batchelor, R. R.; Kristanti, A.; Pei, Y.; Roth, P. J. Para-Fluoro Postpolymerization Chemistry of Poly(Pentafluorobenzyl Methacrylate): Modification with Amines, Thiols, and Carbonylthiolates. *Macromolecules* **2017**, *50* (18), 7028–7040.

(4)   Dietrich, M.; Glassner, M.; Gruendling, T.; Schmid, C.; Falkenhagen, J.; Barner-Kowollik, C. Facile Conversion of RAFT Polymers into Hydroxyl Functional Polymers: A Detailed Investigation of Variable Monomer and RAFT Agent Combinations. *Polym. Chem.* **2010**, *1* (5), 634.

(5)   Delaittre, G.; Pauloehrl, T.; Bastmeyer, M.; Barner-Kowollik, C. Acrylamide-Based Copolymers Bearing Photoreleasable Thiols for Subsequent Thiol-Ene Functionalization. *Macromolecules* **2012**, *45* (4), 1792–1802.

(6)   Skrabania, K.; Miasnikova, A.; Bivigou-Koumba, A. M.; Zehm, D.; Laschewsky, A. Examining the UV-Vis Absorption of RAFT Chain Transfer Agents and Their Use for Polymer Analysis. *Polym. Chem.* **2011**, *2* (9), 2074–2083.

(7)   Delaittre, G.; Barner, L. The Para-Fluoro-Thiol Reaction as an Efficient Tool in Polymer Chemistry. *Polym. Chem.* **2018**, *9*, 2679–2684.

(8)   Turgut, H.; Delaittre, G. On the Orthogonality of Two Thiol-Based Modular Ligations. *Chem. - A Eur. J.* **2016**, *22* (4), 1511–1521.

(9)   Cavalli, F.; Mutlu, H.; Steinmueller, S. O.; Barner, L. The Para-Fluoro-Thiol Reaction as a Powerful Tool for Precision Network Synthesis. *Polym. Chem.* **2017**, *8* (25), 3778–3782.

(10)   Varadharajan, D.; Delaittre, G. Accessing Libraries of Bifunctional Block Copolymers Using Distinct Pentafluorophenyl Moieties. *Polym. Chem.* **2016**, *7*, 7488–7499.

(11)   Noy, J.-M.; Koldevitz, M.; Roth, P. J. Thiol-Reactive Functional Poly(Meth)Acrylates: Multicomponent Monomer Synthesis, RAFT (Co)Polymerization and Highly Efficient Thiol– Para-Fluoro Postpolymerization Modification. *Polym. Chem.* **2014**, *6*, 436–447.

(12)   Humphrey, R. E.; Potter, J. L. Reduction of Disulfides with Tributylphosphine. *Anal. Chem.* **1965**, *37* (1), 164–165.

(13)   Pauloehrl, T.; Delaittre, G.; Bastmeyer, M.; Barner-Kowollik, C. Ambient Temperature Polymer Modification by in Situ Phototriggered Deprotection and Thiol-Ene Chemistry. *Polym. Chem.* **2012**, *3* (7), 1740–1749.

(14)   Cavalli, F.; De Keer, L.; Huber, B.; Van Steenberge, P. H. M.; D'Hooge, D. R.; Barner, L. A Kinetic Study on the: Para -Fluoro-Thiol Reaction in View of Its Use in Materials Design. *Polym. Chem.* **2019**, *10* (22), 2781–2791.

(15)   Li, G. Z.; Randev, R. K.; Soeriyadi, A. H.; Rees, G.; Boyer, C.; Tong, Z.; Davis, T. P.; Becer, C. R.; Haddleton, D. M. Investigation into Thiol-(Meth)Acrylate Michael Addition Reactions Using Amine and Phosphine Catalysts. *Polym. Chem.* **2010**, *1* (8), 1196–1204.

(16)   Institut Laue-Langevin. D22 - Large dynamic range small-angle diffractometer https://www.ill.eu/users/instruments/instruments-list/d22/description/instrument-layout/ (accessed Mar 12, 2020).

(17)   Galinsky, G.; Burchard, W. Starch Fractions as Examples for Nonrandomly Branched Macromolecules. 2. Behavior in the Semidilute Region. *Macromolecules* **1996**, *29* (5), 1498–1506.

(18) Burchard, W. *Solution Properties of Branched Macromolecules*; Springer Berlin Heidelberg: Berlin, Heidelberg, 1999; Vol. 143.

(19) Lederer, A.; Burchard, W.; Hartmann, T.; Haataja, J. S.; Houbenov, N.; Janke, A.; Friedel, P.; Schweins, R.; Lindner, P. Dendronized Hyperbranched Macromolecules: Soft Matter with a Novel Type of Segmental Distribution. *Angew. Chemie - Int. Ed.* **2015**, *54* (43), 12578–12583.

(20) Zimm, B. H. The Scattering of Light and the Radial Distribution Function of High Polymer Solutions. *J. Chem. Phys.* **1948**, *16* (12), 1093–1099.

(21) Glatter, O.; Kratky, O. *Small Angle X-Ray Scattering*; Academic Press, 1982.

(22) Casassa, E. F. Light Scattering from Very Long Rod-Like Particles and an Application to Polymerized Fibrinogen. *J. Chem. Phys.* **1955**, *23* (3), 596–597.

(23) Pedersen, J. S.; Schurtenberger, P. Scattering Functions of Semiflexible Polymers with and without Excluded Volume Effects. *Macromolecules* **1996**, *29* (23), 7602–7612.

(24) Chen, W.-R.; Butler, P. D.; Magid, L. J. Incorporating Intermicellar Interactions in the Fitting of SANS Data from Cationic Wormlike Micelles. *Langmuir* **2006**, *22* (15), 6539–6548.

(25) SasView.org. SasView for Small Angle Scattering Analysis http://www.sasview.org/ (accessed Jan 19, 2020).

(26) U.S. Department of Commerce. National Institute of Standards and Technology (NIST) https://www.nist.gov/ (accessed Jan 23, 2020).

(27) Gerle, M.; Fischer, K.; Roos, S.; Müller, A. H. E.; Schmidt, M.; Sheiko, S. S.; Prokhorova, S.; Möller, M. Main Chain Conformation and Anomalous Elution Behavior of Cylindrical Brushes As Revealed by GPC/MALLS, Light Scattering, and SFM ‡. *Macromolecules* **1999**, *32* (8), 2629–2637.

(28) Rathgeber, S.; Pakula, T.; Wilk, A.; Matyjaszewski, K.; Beers, K. L. On the Shape of Bottle-Brush Macromolecules: Systematic Variation of Architectural Parameters. *J. Chem. Phys.* **2005**, *122* (12), 124904.

(29) Nagasawa, M.; Rice, S. A.; Dinner, A. R. *Physical Chemistry of Polyelectrolyte Solutions*; 2015.

(30) Pomposo, J. A.; Rubio-Cervilla, J.; Moreno, A. J.; Lo Verso, F.; Bacova, P.; Arbe, A.; Colmenero, J. Folding Single Chains to Single-Chain Nanoparticles via Reversible Interactions: What Size Reduction Can One Expect? *Macromolecules* **2017**, *50* (4), 1732–1739.

(31) Tande, B. M.; Wagner, N. J.; Mackay, M. E.; Hawker, C. J.; Jeong, M. Viscosimetric, Hydrodynamic, and Conformational Properties of Dendrimers and Dendrons. *Macromolecules* **2001**, *34* (24), 8580–8585.

(32) Lederer, A.; Burchard, W.; Khalyavina, A.; Lindner, P.; Schweins, R. Is the Universal Law Valid for Branched Polymers? *Angew. Chemie Int. Ed.* **2013**, *52* (17), 4659–4663.

(33) Kurata, M.; Fukatsu, M. Unperturbed Dimension and Translational Friction Constant of Branched Polymers. *J. Chem. Phys.* **1964**, *41* (9), 2934–2944.

(34) Grubisic, Z.; Rempp, P.; Benoit, H. A Universal Calibration for Gel Permeation Chromatography. *J. Polym. Sci. Part B Polym. Lett.* **1969**, *5* (9), 753–759.

(35) Zimm, B. H.; Kilb, R. W. Dynamics of Branched Polymer Molecules in Dilute Solution. *J. Polym. Sci.* **1959**, *37* (131), 19–42.